Charting the Galactic Acceleration Field. II. A Global Mass Model of the Milky Way from the STREAMFINDER Atlas of Stellar Streams Detected in Gaia DR3

Rodrigo Ibata, Khyati Malhan, Wassim Tenachi, Anke Ardern-Arentsen, Michele Bellazzini, Paolo Bianchini, Piercarlo Bonifacio, Elisabetta Caffau, Foivos Diakogiannis, Raphael Errani, et al.

The Astrophysical Journal, 967:89 (35pp), 2024 June 1 https://doi.org/10.3847/1538-4357/ad382d

Charting the Galactic Acceleration Field. II. A Global Mass Model of the Milky Way from the STREAMFINDER Atlas of Stellar Streams Detected in Gaia DR3

Rodrigo Ibata[1], Khyati Malhan[2,3], Wassim Tenachi[1], Anke Ardern-Arentsen[4], Michele Bellazzini[5], Paolo Bianchini[1], Piercarlo Bonifacio[6], Elisabetta Caffau[6], Foivos Diakogiannis[7], Raphael Errani[1], Benoit Famaey[1], Salvatore Ferrone[6], Nicolas F. Martin[1], Paola di Matteo[6], Giacomo Monari[1], Florent Renaud[1,8], Else Starkenburg[9], Guillaume Thomas[10,11], Akshara Viswanathan[9], and Zhen Yuan[1]

[1] Université de Strasbourg, CNRS, Observatoire astronomique de Strasbourg, UMR 7550, F-67000 Strasbourg, France; rodrigo.ibata@astro.unistra.fr
[2] Max-Planck-Institut für Astronomie, Königstuhl 17, D-69117, Heidelberg, Germany
[3] Myrspoven AB, Västgötagatan 1, 11827 Stockholm, Sweden
[4] Institute of Astronomy, University of Cambridge, Madingley Road, Cambridge CB3 0HA, UK
[5] INAF—Osservatorio di Astrofisica e Scienza dello Spazio, via Gobetti 93/3, I-40129 Bologna, Italy
[6] GEPI, Observatoire de Paris, Université PSL, CNRS, 5 Place Jules Janssen, 92190 Meudon, France
[7] Data61, CSIRO, Floreat WA, Australia
[8] University of Strasbourg Institute for Advanced Study, 5 allée du Général Rouvillois, F-67083 Strasbourg, France
[9] Kapteyn Astronomical Institute, University of Groningen, Landleven 12, 9747 AD Groningen, The Netherlands
[10] Instituto de Astrofísica de Canarias, E-38205 La Laguna, Tenerife, Spain
[11] Universidad de La Laguna, Dpto. Astrofísica, E-38206 La Laguna, Tenerife, Spain
Received 2023 November 28; revised 2024 March 21; accepted 2024 March 21; published 2024 May 21

Abstract

We present an atlas and follow-up spectroscopic observations of 87 thin stream-like structures detected with the STREAMFINDER algorithm in Gaia DR3, of which 28 are new discoveries. Here, we focus on using these streams to refine mass models of the Galaxy. Fits with a double-power-law halo with the outer power-law slope set to $-\beta_h = -3$ yield an inner power-law slope of $-\gamma_h = -(0.97^{+0.17}_{-0.21})$, a scale radius of $r_{0,h} = 14.7^{+4.7}_{-1.0}$ kpc, a halo density flattening $q_{m,h} = 0.75 \pm 0.03$, and a local dark matter density of $\rho_{h,\odot} = 0.0114 \pm 0.0007\, M_\odot\, \mathrm{pc}^{-3}$. Freeing β yields $\beta = 2.53^{+0.42}_{-0.16}$, but this value is heavily influenced by our chosen virial mass limit. The stellar disks are found to have a combined mass of $4.20^{+0.44}_{-0.53} \times 10^{10}\, M_\odot$, with the thick disk contributing $12.4\% \pm 0.7\%$ to the local stellar surface density. The scale lengths of the thin and thick disks are $2.17^{+0.18}_{-0.08}$ and $1.62^{+0.72}_{-0.13}$ kpc, respectively, while their scale heights are $0.347^{+0.007}_{-0.010}$ and $0.86^{+0.03}_{-0.02}$ kpc, respectively. The virial mass of the favored model is $M_{200} = 1.09^{+0.19}_{-0.14} \times 10^{12}\, M_\odot$, while the mass inside of 50 kpc is $M_{R<50} = 0.46 \pm 0.03 \times 10^{12}\, M_\odot$. We introduce the Large Magellanic Cloud (LMC) into the derived potential models, and fit the Orphan stream therein, finding a mass for the LMC that is consistent with recent estimates. Some salient highlights include the nearby trailing arm of ω Cen, and a nearby very metal-poor stream that was once a satellite of the Sagittarius dwarf galaxy. Finally, we unambiguously detect a hot component around the GD-1 stream, consistent with it having been tidally preprocessed within its own dark matter subhalo.

Unified Astronomy Thesaurus concepts: Stellar streams (2166); Galaxy structure (622); Dark matter (353)

Supporting material: machine-readable table

1. Introduction

The formation of galaxies involves a complex interplay between the accretion of gas and the merging of previously bound fragments. When these fragments are of low mass compared to their host or their dominant companion, tidal forces can have time to act progressively to slowly unbind material from the lower-mass object. If the disruption is gradual, so that the injected energy is only just enough to unbind the most loosely bound stars, the ejected objects will find themselves on similar orbits to their progenitor, and diffuse along a *tidal stream* pattern that approximates that orbit (Combes et al. 1999). The stars that by chance acquire higher kinetic energy leave approximately through the L1 Lagrange point and race ahead of their progenitor, forming the leading tidal arm. Conversely, those stars that are perturbed into lower-energy orbits emerge roughly through the L2 point and form the trailing arm (see, e.g., Fukushige & Heggie 2000).

Tidal disruption can take place over hundreds of millions to billions of years, with the dwindling progenitor slowly losing stars that drift away along their slightly different orbits. The requirement that the stream stars originated in their progenitor provides a physical constraint that allows us to attempt to turn back the clock and find the smooth potential and any perturbations that can permit this inversion. This is perhaps the most useful property of stellar streams, giving us a means to peer into the dynamical past of a galaxy without making assumptions about its equilibrium, and so uncover properties of the global and local dark matter distribution that are otherwise invisible. Nevertheless, it should be borne in mind that tidal disruption typically produces ejecta with a spectrum of energies, meaning that stars move along the tidal stream pattern at different speeds, so that position along the pattern is not perfectly correlated with ejection time. Furthermore, epicyclic patterns are also present in streams, which can complicate their analysis (Küpper et al. 2008).

This promise of being able to map out the acceleration field of our Galaxy motivated us to develop a dedicated stream-detection algorithm, STREAMFINDER, with the intention to deploy it on the Gaia mission catalogs (Gaia Collaboration et al. 2016). STREAMFINDER is effectively a friend-finding algorithm, with a *distance* in the parameter space of observables defined so as to make objects on similar orbits and with similar stellar populations appear close together. The procedure is presented in detail in Malhan & Ibata (2018), Malhan et al. (2018, hereafter Paper I), and Ibata et al. (2021b, hereafter Paper II). Paper I applied the algorithm to the Gaia DR2 catalog, based on 22 months of astrometric observations, while Paper II extended the search to the Gaia EDR3 catalog, with 33 months of observations. In Martin et al. (2022), the STREAMFINDER sources were crossmatched with the Pristine survey catalog (Starkenburg et al. 2017; Martin et al. 2023), providing metallicity estimates for the stars and hence better discrimination against contamination, which allowed us to lower the detection threshold and so find further stream candidates. A compendium of Galactic stellar streams was compiled by Mateu (2023), and a bibliography of previous searches is given therein.

Our aim in this contribution is to present the STREAMFINDER results for the full Gaia DR3 data set (Gaia Collaboration et al. 2023), which supersedes EDR3. The new analysis makes use of the radial velocity measurements for 33 million stars provided by Gaia DR3, which we complement with measurements from other large spectroscopic surveys. We will also present measurements from our own dedicated spectroscopic follow-up with the Very Large Telescope (VLT)/UVES and Isaac Newton Telescope/Intermediate Dispersion Spectrograph (INT/IDS) as well as our earlier CFHT/ESPaDOnS measurements, providing the community the full Gaia DR3 stream catalog as uncovered by our algorithm. The main scientific goal of the present contribution is to conduct a detailed analysis of the constraints that these observations impose on the large-scale mass distribution in the Milky Way.

The outline of this paper is as follows. In Section 2, we begin by explaining the small alterations we made to the algorithm for this new Gaia DR3 analysis, while Section 3 briefly reviews our follow-up spectroscopic observations, and Section 4 presents the new sky maps and detections. In Section 5, we begin the modeling of the streams, assuming that the Milky Way is axisymmetric and that its center defines the origin of an inertial frame around which the streams orbit. Section 6 generalizes the model to allow the Local Group galaxies to move under the influence of each other, and the streams will be modeled as dissolving systems. In Section 7, we explain how we use test-particle simulations to correct simple orbit integrations, and thus greatly speed up the exploration of the parameters of the model. The results of the stream-fitting analysis are presented in Section 8. In Section 9, we briefly summarize some salient streams, and finally draw our conclusions in Section 10.

2. STREAMFINDER Alterations

Here, we use a search algorithm version very similar to that presented in Paper II. As before, we aim to find a low-contrast stream superimposed on a *contaminating* population of normal Milky Way stars, and so we adopt a log-likelihood function of

$$\ln \mathcal{L} = \sum_{\text{data}} \ln \left[\eta \mathcal{P}_{\text{stream}}(\theta) + (1 - \eta)\, \mathcal{P}_{\text{cont}}\right], \tag{1}$$

where η is the fraction of stars in the stream, $\mathcal{P}_{\text{stream}}(\theta)$ is the probability distribution function (PDF) of the stream model with parameters θ, and $\mathcal{P}_{\text{cont}}$ is the PDF of the contaminants. The stream model is a model of a stellar population along a simple orbit that has been smeared out with a Gaussian

$$\begin{aligned}\mathcal{P}_{\text{stream}}(\theta) &= \mathcal{P}_{\text{length}} \times \mathcal{P}_{\text{width}} \times \mathcal{P}_{\text{LF}} \times \mathcal{P}_{\text{color}} \times \mathcal{P}_{\mu} \times \mathcal{P}_{\varpi} \\ &\quad \times \mathcal{P}_{v} \\ &= \mathcal{P}^{\text{Paper II}}_{\text{stream}}(\theta) \times \mathcal{P}_{v},\end{aligned} \tag{2}$$

where $\mathcal{P}_{\text{length}}$ is a uniform distribution along an $L = 20^{\circ}$ stream fragment, $\mathcal{P}_{\text{width}}$ is a Gaussian width of 50 pc dispersion, $\mathcal{P}_{\text{LF}}$ is the probability of being drawn from the luminosity function of the adopted simple stellar population (SSP) model (we adopt the PARSEC isochrone models, Bressan et al. 2012), $\mathcal{P}_{\text{color}}$ is a probability of the measured $G_{\text{Bp}} - G_{\text{Rp}}$ color of the star at the observed G magnitude, and $\mathcal{P}_{\mu}$ and $\mathcal{P}_{\varpi}$ are the Gaussian probabilities of the observed astrometry given an assumed 5 km s^{-1} intrinsic stream velocity dispersion, and a 50 pc line-of-sight dispersion. (The proper motion probability term $\mathcal{P}_{\mu}$ is a two-dimensional Gaussian PDF incorporating the proper motion uncertainties in R.A. and decl. and their correlation cross-terms.) Up to here, all is identical to the model described in Paper II. However, since the DR3 catalog provides many line-of-sight velocity measurements, we now also include a simple Gaussian probability $\mathcal{P}_{v}$ that the star has a line-of-sight velocity within 5 km s^{-1} of the orbit. Most stars in the DR3 catalog do not have measured velocities, and for those, we set $\mathcal{P}_{v} = 1$.

In an earlier contribution we used a much wider (500 pc) spatial template in order to detect the stream of the Sagittarius dwarf galaxy and any similar structures (Ibata et al. 2020a). In contrast, our decision in the present work to adopt a characteristic 50 pc width spread and 5 km s^{-1} velocity spread for the template was made to facilitate the detection of globular cluster streams. In the Harris (2010) catalog of Milky Way globular clusters, 79% have tidal radii <50 pc (their Gaussian width is, of course, much smaller), and 78% have a central velocity dispersion <5 km s^{-1}. Streams with much wider spatial or velocity dispersions will have their significance downweighted by our template choice; in future work, we intend to overcome this limitation by using a wider range of templates.

Including velocities in the likelihood function of the stream model means that we also have to include them in the contamination model $\mathcal{P}_{\text{cont}}$. We decided to retain the previously fitted, completely empirical, Gaussian mixture model (GMM) description $\mathcal{P}^{\text{Paper II}}_{\text{cont}}(\alpha, \delta, \mu_{\alpha}, \mu_{\delta}, G, G_{\text{BP}} - G_{\text{RP}}, \varpi)$ but include a new term $\mathcal{P}_{\text{GMM}}$ as follows:

$$\begin{aligned}&\mathcal{P}_{\text{cont}}(\alpha, \delta, \mu_{\alpha}, \mu_{\delta}, G, G_{\text{BP}} - G_{\text{RP}}, \varpi, v) \\ &= \mathcal{P}^{\text{Paper II}}_{\text{cont}}(\alpha, \delta, \mu_{\alpha}, \mu_{\delta}, G, G_{\text{BP}} - G_{\text{RP}}, \varpi) \\ &\quad \times \mathcal{P}_{\text{GMM}}(v|\alpha, \delta, G, G_{\text{BP}} - G_{\text{RP}}, \varpi).\end{aligned} \tag{3}$$

Note that the final term ignores the correlations of line-of-sight velocity with proper motion, which we felt was a necessary simplifying assumption given the relative scarcity of the velocity information compared to the astrometric information.

This $\mathcal{P}_{\rm GMM}$ term is calculated from the available velocities in large $5.^{\circ}6 \times 5.^{\circ}6$ tiles of a zenithal equal area projection of the sky.

The bulk of the radial velocity data that we provide to the algorithm are the 33 million stars with radial velocity measurements published as part of Gaia DR3. We complemented these measurements with other large public spectroscopic surveys, crossmatching the full Gaia DR3 survey with the APOGEE-2 survey (Majewski et al. 2017), the GALAH DR3 survey (Buder et al. 2018), the LAMOST DR7 survey (Cui et al. 2012), the Radial Velocity Experiment DR5 (Kunder et al. 2017), the Sloan Digital Sky Survey (SDSS)/Segue survey (Yanny et al. 2009), the Gaia-ESO survey (Randich et al. 2022), and the S5 survey (Li et al. 2019). We also included measurements of Palomar 5 stars by Odenkirchen et al. (2009) and Ibata et al. (2017a), as well as our previous velocity measurements of STREAMFINDER targets with CFHT/ESPaDOnS and the New Technology Telescope (NTT)/EFOSC2 and VLT/UVES presented in Paper II. For those sources where more than one measurement was available, we adopted the value with the lowest uncertainty.

A further difference with respect to Paper II is that we now include stars from the Gaia DR3 RR Lyrae variable catalog (Clementini et al. 2022). Although we used the VizieR database to recover any measured line-of-sight velocity of these stars (where available) we decided to ignore this information in the STREAMFINDER analysis, as RR Lyrae are very strong radial velocity variables, and we could not reliably phase-correct the heterogeneous archival velocity measurements, so for RR Lyrae we set $\mathcal{P}_v = 1$ in Equation (2). For these stars, we use the Muraveva et al. (2018) metallicity G-band absolute magnitude relation to predict a distance given the SSP trial metallicity, and set $\mathcal{P}_{\rm LF} = 1$ in Equation (2).

The algorithm proceeds star by star through the Gaia survey, using each star as a reference to launch trial orbits within the adopted fiducial potential (Dehnen & Binney 1998). The potential is actually going to be finely constrained with the detected streams in the following sections, but see Malhan & Ibata (2018) on the minor influence that a wrong potential in the first step has on the stream detection itself. The measured astrometry and photometry of the reference star are used to generate plausible trial orbits, and the assumed stellar population model provides the link between photometry and distance. When the line-of-sight velocity is available, it is used; otherwise, we scan through the missing information as explained in Papers I and II. For each trial orbit of the star, we find (and record) all the neighbors within the (10°) search radius that can be associated within a chosen threshold of the stream model. We define k to be the number of stars found in this way around a trial orbit centered on a particular star.

In many fields of astronomy, local measures of significance are used to define a detection, as the sources typically appear small (e.g., a star or distant galaxy) compared to the field of view of the instrument or survey, and there is a well-defined *background*. However, in the present situation, we are interested in detecting structures that subtend very long arcs on the sky with a wide range of (typically) foreground contamination. For streams we therefore seek a *global* statistic to quantify detection. The log-likelihood of Equation (1) can provide such a measure, but we would need to sum over the full Gaia survey (with more than 10^9 stars) in order to compare models of different structures. Note also that we would need to render the model more complex with each added stream; doing this in the Bayesian framework would require us to calculate the Bayesian evidence for each additional candidate structure to verify that it merits being added. This would be prohibitively computationally expensive. To simplify the calculation, we break up the log-likelihood into two terms $\ln \mathcal{L} = \ln \mathcal{L}_1 + \ln \mathcal{L}_2$, where $\ln \mathcal{L}_1$ corresponds to the parameter space region R_1 containing k stars (within, say 3σ of the model in the orbital and stellar populations parameters) and $\ln \mathcal{L}_2$ is for the complementary region R_2 with $n-k$ stars, where n is the number of stars in $R_1 + R_2$. Now for region R_1:

$$\ln \mathcal{L}_1 = \sum_{j=1}^{k} \ln\left(\eta \mathcal{P}_{j,\rm model} + (1-\eta)\mathcal{P}_{j,\rm cont}\right) - \ln \mathcal{P}_{j,\rm cont}, \quad (4)$$

where the final term provides a convenient zero-point so that $\ln \mathcal{L}_1 = 0$ if no stream is present. In region R_2 we make the simplification that the stream model probability is zero, so the corresponding log-likelihood is

$$\begin{aligned} \ln \mathcal{L}_2 &\approx \sum_{j=1}^{n-k} \ln((1-\eta)\mathcal{P}_{j,\rm cont}) - \ln \mathcal{P}_{j,\rm cont} \\ &= (n-k)\ln(1-\eta), \end{aligned} \quad (5)$$

where again we have included a zero-point choice so that $\ln \mathcal{L}_2 = 0$ when $\eta = 0$. Adding Equations (4) and (5) gives the total log-likelihood of

$$\ln \mathcal{L} = (n-k)\ln(1-\eta) + \sum_{j=1}^{k} \ln\left(1 - \eta + \eta \frac{\mathcal{P}_{j,\rm model}}{\mathcal{P}_{j,\rm cont}}\right), \quad (6)$$

which allows a straightforward statistical comparison of the detected features over the full sky, and has the convenient property of being zero when $\eta = 0$.

Previously, in Papers I and II, we selected the stream solution η with the highest likelihood according to Equation (6), which is a choice that works well at high Galactic latitude, but becomes problematic at low latitude where the number of possible associations becomes very large. We remind the reader that our algorithm is not finding the best single model fit to the global Gaia data, but rather our procedure checks whether a large-scale stream model centered at the phase-space position of each of the billions of stars in the survey is statistically significant or not. Hence, a given star may be considered a member of many different proposed groups. This is, of course, very different from the usual fitting problems in astronomy, where we fit the parameters of a model to a data set, or in detection problems, where we say fit galaxy models to a large number of spatially independent regions of a pixellated image. For the present work we therefore decided to use the logarithm of the likelihood per star of the group as our selection statistic

$$\ln \hat{\mathcal{L}} = \ln \mathcal{L} - k, \quad (7)$$

where k is again the number of stars associated with the trial orbit.[12] Optimizing this statistic forces the algorithm to find the

[12] In the present context, the statistic in Equation (7) is reminiscent of the Akaike information criterion, AIC $= 2m - 2\ln \mathcal{L}$, which is a statistical estimator designed to optimize the balance between goodness of fit and model complexity (m is the number of parameters of the model). Because of the fact that stars can be reused in different stream solutions, the higher k is on average, the more potential overlapping models there will be, and so the higher the complexity of the global model will be.

orbit and associated stream fraction η that maximizes the number of high-likelihood associations. By adjusting the acceptance threshold, stream maps built with this $\ln\hat{\mathcal{L}}$ statistic can be selected to be very similar at high Galactic latitude to those built previously using the $\ln\mathcal{L}$ statistic. However, close to the plane of the Galaxy, the new maps do not show spurious solutions that possess a large number of low probability members (i.e., that are composed mostly of stars at a high number of standard deviations from the orbit and stellar populations model).

3. Spectroscopic Observations

We used the VLT/UVES spectrograph (D'Odorico et al. 2000) to follow up on selected STREAMFINDER sources detected in the Gaia EDR3 and DR3 catalogs. These runs comprise runs 105.20AL.001 (2.5 nights in visitor mode), 110.246A.001 (40 hr service in service mode), and 111.2517.001 (3.6 nights in visitor mode). Our instrumental setup uses the DIC2 dichroic beamsplitter in the "437+760" setting, covering the wavelength ranges 3730–4990 and 5650–9460 Å. To reduce read noise, we binned the CCD in 2×2 pixel blocks, which in conjunction with a $1\farcs0$ wide slit, yields a spectral resolution of approximately 40,000. Exposure times were selected on a star-by-star basis to reach signal-to-noise ratio ∼3–5 for the fainter stars in the sample, so as to measure their radial velocities, but we set a minimum exposure time of 5 minutes. For the brighter stars, this minimum exposure time also allowed some elemental abundances to be measured. The spectra were reduced with the EsoReflex pipeline using daytime calibration arc lamps and flat-field images, resulting in extracted wavelength-calibrated one-dimensional spectra.

We also secured observations with the IDS long-slit spectrograph on the 2.5 m Isaac Newton Telescope in several runs over the course of 2022. Bright northern hemisphere stream stars were targeted with typically ∼1 hr exposures at $G = 16$ mag. The instrument was configured with the RED+2 detector, the R1200R grating with a central wavelength set to 8500 Å, a $1\farcs$ wide slit, and the GG495 order sorting filter.

The radial velocities of the target stars were measured with the IRAF fxcor algorithm, using the bright and relatively metal-poor star HD 182572 as a radial velocity standard. The UVES spectra were of sufficient quality and resolution to obtain excellent radial velocity measurements with <1 km s^{-1} uncertainty for stars to $G = 18$ mag, while the IDS spectra resulted in velocity uncertainties of ∼10 km s^{-1} at $G = 16$ mag.

4. Gaia DR3 STREAMFINDER Maps

We ran STREAMFINDER using seven different SSP templates with metallicity [Fe/H] = –2.2, −1.9, −1.7, −1.5, −1.3, −1.1, −0.7, and a common age 12.5 Gyr, as we are primarily aiming to discover halo structures. We allowed the solutions to explore the distance range of [1, 100] kpc. As in Paper II, the Gaia catalog was limited to sources with $G_0 < 20$ mag and V-band extinction $A_V < 2$ mag, so as to mitigate against variations in extinction and survey depth due to the satellite's scanning law.[13] The full sky was processed with the exception of circular regions around satellites; the radius of these masked regions was set to twice the tidal radius for globular clusters and seven times the half-light radius for satellite galaxies, as detailed in Paper II.

Figures 1 and 2 show the resulting sky maps of the detections of 24,540 (non-RR Lyrae) sources (listed in Table 1) with $\ln\hat{\mathcal{L}} > 19.8$ (note that with the standard log-likelihood, the value $\ln L = 19.8$ corresponds to a 6σ threshold) colored according to proper motion along the Galactic longitude and latitude directions, respectively. The corresponding distance solutions are shown in Figure 3, colored according to the distance modulus. Figure 4 displays the 2178 (non-RR Lyrae) sources with measured line-of-sight velocities, while Figure 5 shows the mean metallicity of the streams (listed in Table 3) as calculated from the mean of the spectroscopic metallicity measurements (or photometric metallicities, for those structures without spectroscopic measurements). These maps display a rich tapestry of crisscrossing streams that possess coherent behavior in proper motion, line-of-sight velocity, and distance. In Figure 6, we have selected a contrasting color scheme to allow easier visual disambiguation of the overlapping structures that can be discerned in Figures 1–5.

To facilitate subsequent analyses, we create a local coordinate system on a per stream basis by fitting a great circle to each structure using a least squares criterion (we consider that the uncertainties in sky position are negligible). For the streams with known globular cluster progenitors, we require the fit to intersect the center of the globular cluster, and we also use the R.A. of the cluster to define the zero-point of the great circle coordinates (ϕ_1, ϕ_2) along and perpendicular to the stream. The coordinate ϕ_1 is oriented so that the stream's velocity is approximately parallel to it,[14] while ϕ_2 is in the direction perpendicular to the great circle. For stream #48 (Orphan-Chenab) we chose the zero-point proposed by Koposov et al. (2019), while for stream #53 (GD-1) we fully adopted the (ϕ_1, ϕ_2) coordinate system of Koposov et al. (2010). The poles and zero-point of the (ϕ_1, ϕ_2) coordinates are provided in Table 3. We also estimate the stellar mass of each stream, using the metallicity listed in Table 3 together with the fitted stream distance models (calculated as explained in Section 5), to correct for the missing stars in the stellar population, assuming that the survey is complete to $G_0 = 20$ mag. These stellar masses are also listed in Table 3, but we stress that they are rough approximations and involve many assumptions, including that we have identified the full extent of each stream and that only a single stellar population is present.

Figures 7–9 display the individual stream structures in an array of three columns. The first column shows the line-of-sight velocity as a function of the angle ϕ_1 along each stream. The proper motion along the ϕ_1 direction is displayed in the middle column, while the last column displays the color–magnitude diagram of the population. The same color scheme as in Figure 6 is employed.

The nature of the detections can be appreciated better by first considering their dynamical properties. Next, we use the streams to understand the global properties of the Milky Way, which will then give us access to their orbits, and then we return to a discussion of individual objects in Section 9.

[13] To correct for interstellar extinction, we assume that all the dust is in the foreground and interpolate between the pixels of the Schlegel et al. (1998) maps, adopting the Schlafly & Finkbeiner (2011) recalibration with $R_V = 3.1$.

[14] The stream velocity vector need not be perfectly parallel to ϕ_1 due to projection and reflex motion.

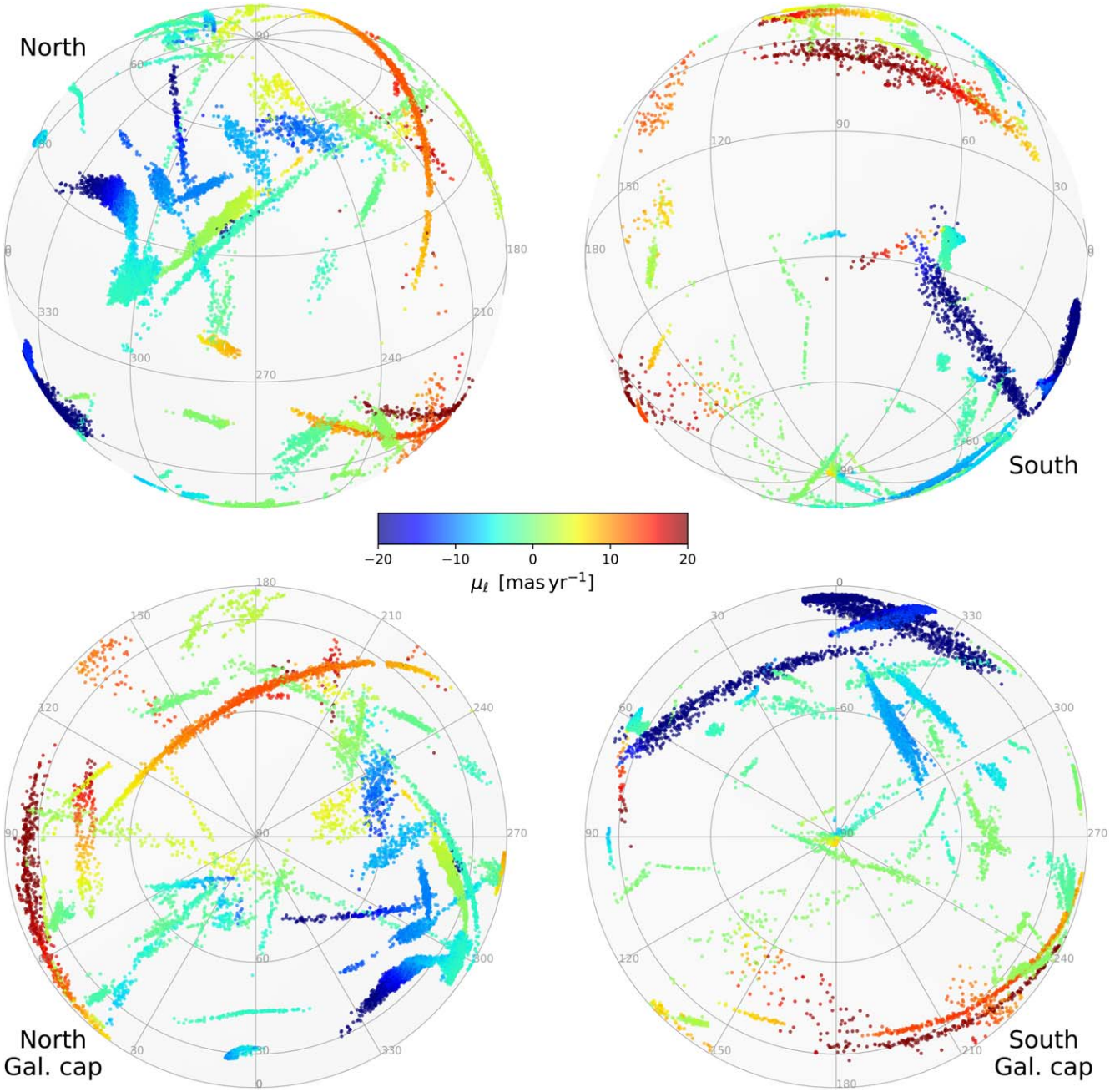

Figure 1. Four different projections in Galactic coordinates of the 24,540 STREAMFINDER sources listed in Table 1 with $\ln \hat{\mathcal{L}} > 19.8$ (more restrictive than a 6σ threshold). The color of the points encodes the proper motion μ_ℓ along the Galactic longitude direction, as measured by Gaia in the DR3 catalog.

5. Stream Fitting with Corrected Orbits in an Isolated Milky Way

We begin our modeling efforts by considering the Milky Way to be an isolated axisymmetric galaxy, whose center defines the origin of an inertial frame around which its satellites will orbit. In this context, we seek to find the most likely Galactic mass model that admits progenitor orbits that fit the stream data simultaneously. As we have mentioned before, stellar streams do not precisely delineate the orbital path of their progenitors. To overcome this complication, we will proceed in an iterative manner to find plausible functions $\Delta_\Theta(\phi_1)$ in the derived mass model that correct the offset between the stream and the progenitor orbit at ϕ_1 for each observable phase-space coordinate Θ.

While we could have tried to fit the whole data set of 87 streams and >24,500 stars, to find the best mass model, we restrict ourselves in the present contribution to a conservative sample containing velocity-confirmed members and RR Lyrae. We further impose that the individual streams should be long (>10° in length), containing at least five line-of-sight velocity measurements with a clear linear trend. Since we most probably only detect a small stream segment of the closest streams, we also select those structures at a heliocentric distance >2.5 kpc (this limit is somewhat arbitrary, and in future work, we will reexamine in detail the orbits of the closer streams). We set aside the Orphan stream for the initial analysis because although it has excellent data, it is probably affected by the Large Magellanic Cloud (LMC; Erkal et al. 2019). We have

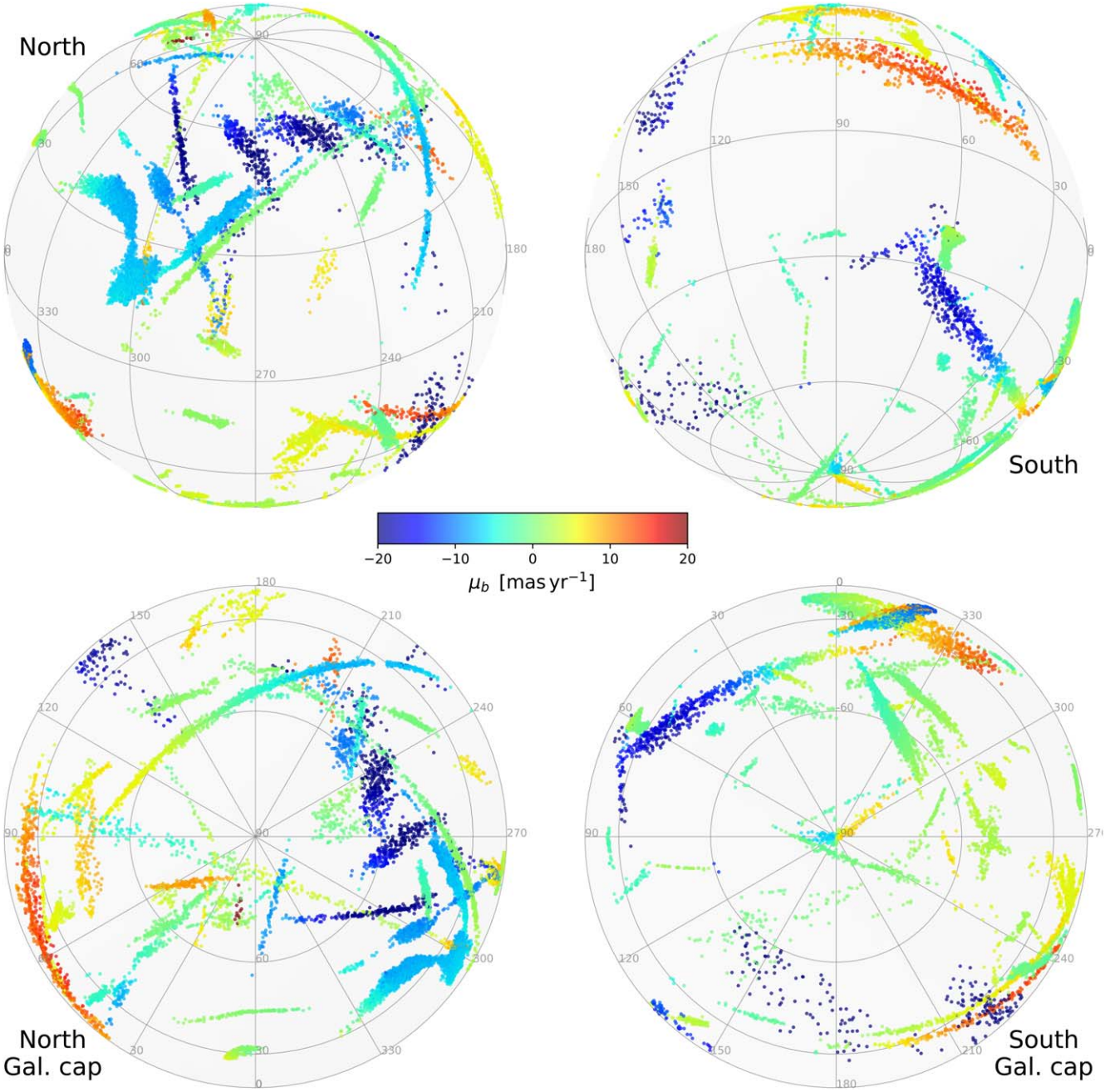

Figure 2. As in Figure 1, but showing the measured proper motion μ_b of the sources along the Galactic longitude direction.

previously shown (Ibata et al. 2019a) that the Fimbulthul stream possesses a complex structure due to the internal rotation of its progenitor, the massive cluster ω Cen, and so we decided not to model this structure either. The sample of 29 long and thin streams we fit here are flagged "1" in the column titled "sample" in Table 3. The data set comprises 1397 data points: 1098 stars with measured line-of-sight velocities, five globular clusters (with phase-space parameters derived from the compendia in Vasiliev 2019 and Baumgardt & Vasiliev 2021), and 294 Gaia RR Lyrae (for which we ignore any measured line-of-sight velocities due to concerns over their variability).

We constructed a similar Markov Chain Monte Carlo (MCMC) orbit-fitting algorithm to that presented in Ibata et al. (2018), but altered to allow for simultaneous adjustment to many streams. The MCMC driver algorithm we use was originally developed by Ibata et al. (2011), based on the *walkers* scheme proposed by Goodman & Weare (2010). The `walkers` algorithm (that simulates a population of agents sampling the likelihood at different parameter space locations) is very efficient as it is affine-invariant and adapts automatically to the multidimensional covariance of the problem.

The Milky Way potential is generated via multipole expansion from analytical double-exponential density models (to represent the disk components) or double-power-law density models (to represent the spheroidal components), following Dehnen & Binney (1998). We allow each disk component to have up to three parameters: central surface

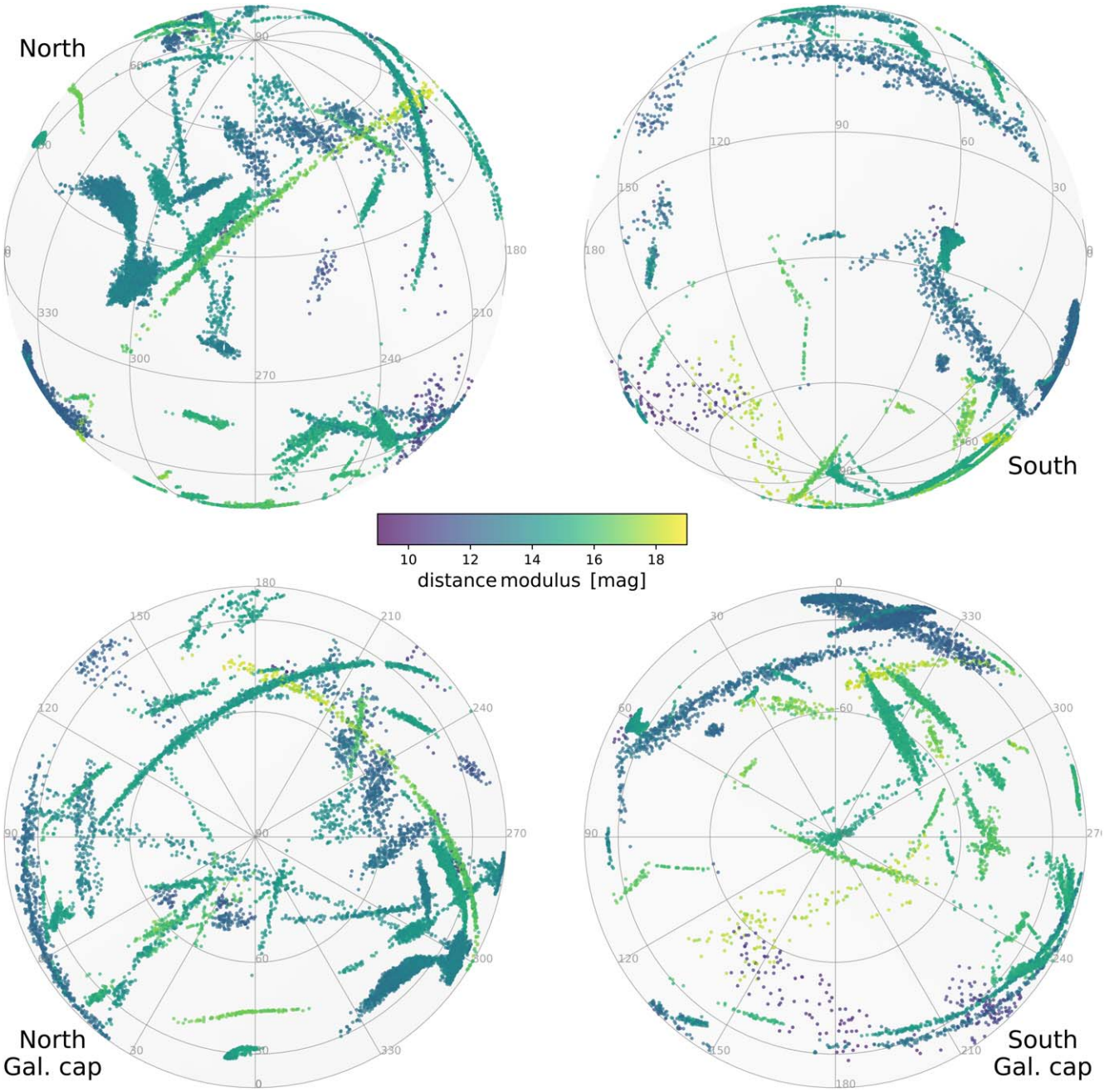

Figure 3. As in Figure 1, but showing the distance solutions, displayed as distance modulus.

density Σ_d, a scale length h_R and scale height h_z

$$\rho_d(R, z) = \frac{\Sigma_d}{2h_z} \exp\left(-\frac{R}{h_R} - \frac{|z|}{h_z}\right). \quad (8)$$

In contrast we allow the spheroidal components to have six parameters: central density ρ_0, density flattening q_m, inner power-law slope $-\beta$, outer power-law slope $-\gamma$, scale radius r_0, and truncation radius r_t

$$\rho_s(s) = \rho_0 \left(\frac{s}{r_0}\right)^{-\gamma} \left(1 + \frac{s}{r_0}\right)^{\gamma-\beta} e^{-s^2/r_t^2}, \quad (9)$$

where $s = \sqrt{R^2 + z^2/q_m^2}$ is an ellipsoidal coordinate. Each orbit obviously requires six parameters; however, for those streams with a known progenitor, we consider their center to be perfectly determined, leaving four free parameters, while for all others, we anchor the orbit at $\phi_1 = 0^\circ$ (except for GD-1, as discussed below), leaving five free parameters.

Hence, a full parameter exploration of the problem would have in excess of 150 parameters and would therefore be very challenging for an MCMC approach. However, the orbits can be fit independently of one another, which motivated our choice to implement a nested MCMC search. The outer MCMC loop simply proposes the Galaxy model parameters (and the components of the Solar peculiar motion vector, if so desired). The inner loop adopts those Galaxy model parameters and attempts to fit each stream independently. We implemented an option for two algorithm variants for the inner loop. The first option is another independent MCMC search with 500

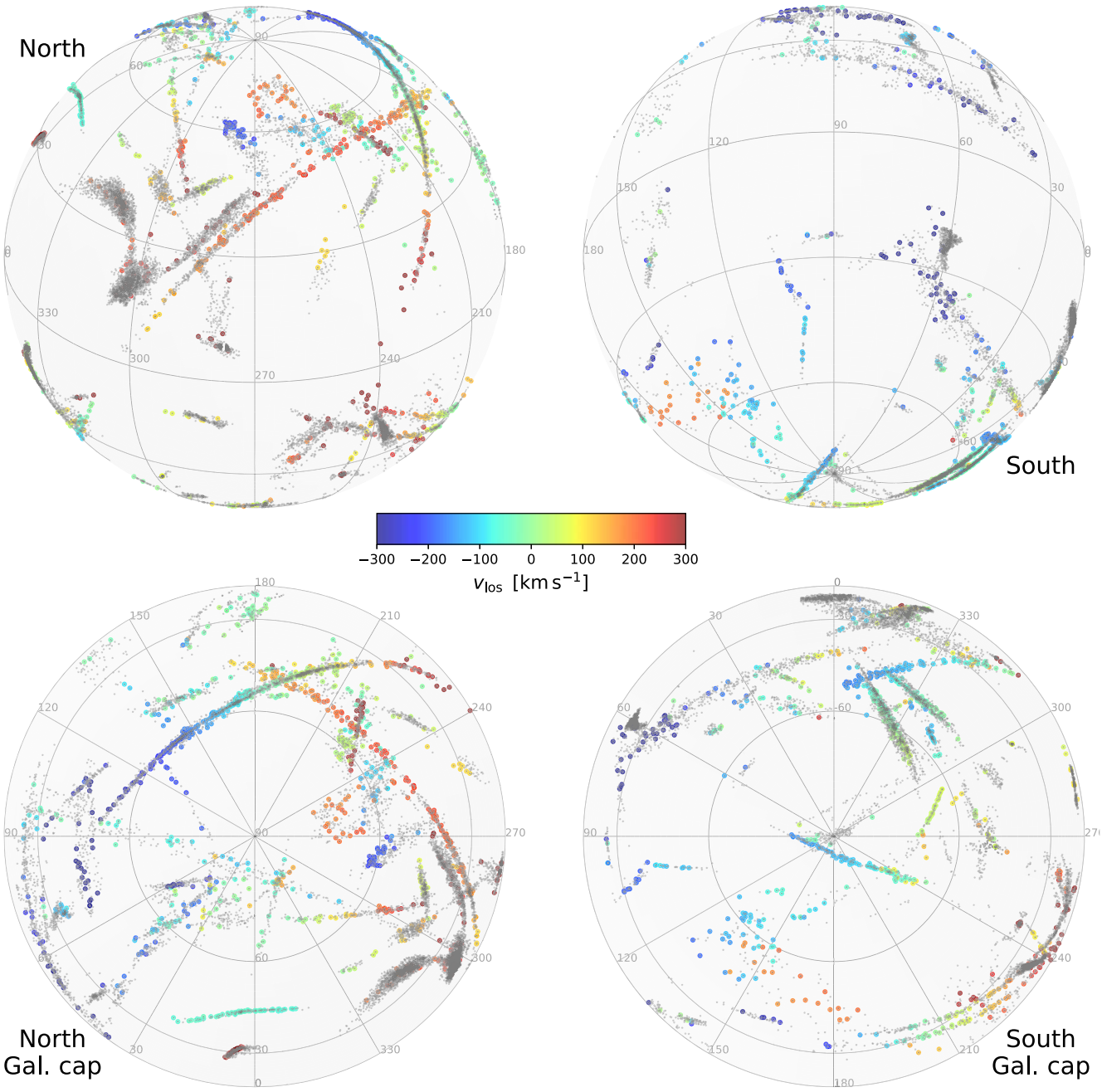

Figure 4. As in Figure 1, but showing the line-of-sight velocity measurements of the stars in the sample. Stars without such measurements are marked with small gray points.

iterations, where every 25 iterations of the inner loop, the step size is adjusted to try to maintain a 25% acceptance ratio (independently for each stream). The best solution and step size (for each stream) are recorded as if they were parameters of the outer loop and reused in the next run of the inner loop. The second option is to use a Nelder–Mead *downhill simplex* search (Press et al. 1992). We adopted a log-likelihood tolerance of 10^{-4}, which gave robust results in our tests (each such search requires ≈1000 likelihood evaluations). The Nelder–Mead method can be sensitive to the chosen starting point of the search, so we reran it with different randomly drawn positions until the best likelihood solution is found again to within the chosen tolerance. We found that both the MCMC and downhill simplex options for the inner loop give similar results, but the latter is computationally cheaper to reach a given accuracy, while the former allows one to estimate confidence intervals on the stream parameters. The results shown below were calculated using the downhill simplex as the optimization method of the inner loop.[15]

The outer loop uses 96 MCMC walkers, and we adjust the stretch factor of the proposed walker steps dynamically (see Goodman & Weare 2010) every 25 iterations, aiming to obtain a 25% acceptance ratio. We run the algorithm for at least 200,000 *burn-in* iterations, discard that data, and then continue

[15] Although we first employ the MCMC method in the inner loop to obtain an estimate of the uncertainties of the stream model parameters, which are then reused in the generation of the (Gaussian) random starting points for the downhill simplex method.

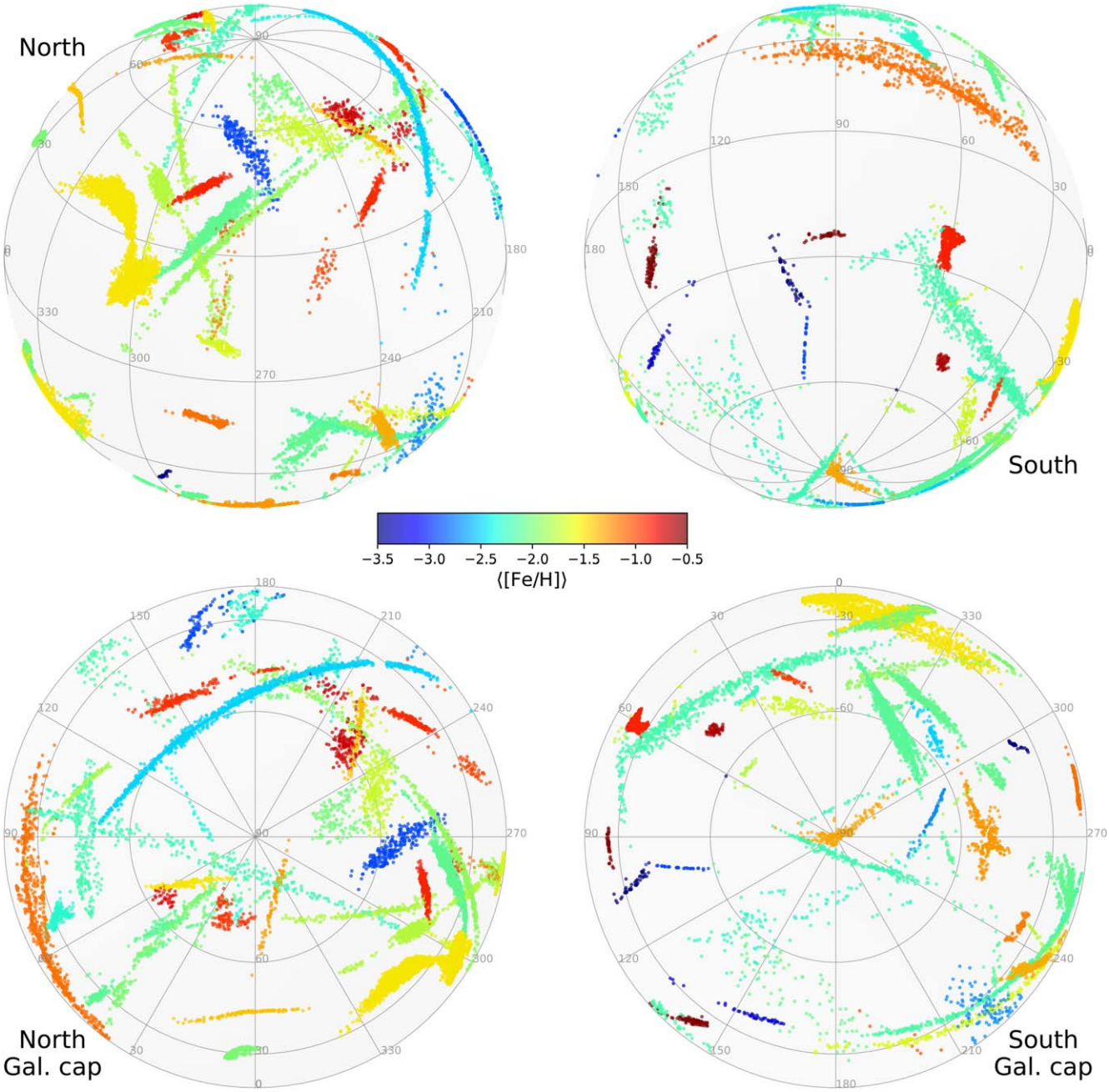

Figure 5. As in Figure 1, but showing the mean spectroscopic metallicity ⟨[Fe/H]⟩ (or photometric metallicity when spectroscopic values are not available) of the streams, as listed in Table 3.

for a further 500,000 iterations (i.e., for a total of $500{,}000 \times 1000$ evaluations of the combined likelihood of the 29 streams, with each orbit being sampled at a resolution of up to 10,000 points). For every step of the outer loop, the Galaxy parameters and the stream parameters of that step are recorded as the MCMC chain, which is the desired final output of the algorithm.[16] We consider that the MCMC exploration converged when the parameter statistics of the first and second half of the 500,000 iteration-long chains were statistically identical. One such optimization of the Galaxy and stream parameters typically takes ≈5000 CPU hr.

The log-likelihood objective function we choose to fit to the sample attempts to model the expected combination of thin streams, each enveloped by a wider *cocoon* population and a small amount of contamination. The adopted objective function is therefore

$$\ln \mathcal{L} = \sum_{\text{data}} \ln[\,(1-\zeta-\chi)\mathcal{P}^{\text{fit}}_{\text{stream}} + \zeta\mathcal{P}_{\text{cocoon}} + \chi\mathcal{P}_{\text{contam}}] + \ln \mathcal{L}_{\text{ancillary}}, \quad (10)$$

[16] Due to the low cost of the individual orbit integrations, which nevertheless require a non-negligible amount of memory to store their paths, this nested procedure proved to be very difficult to parallelize efficiently with standard parallelization libraries such as OPENMP/MPI. Consequently, we developed a custom parallelization scheme using persistent jobs (eliminating overheads due to memory allocation and data ingestion), one per machine core, that wait to be handed the different input parameters farmed out by the master process that handles the MCMC exploration.

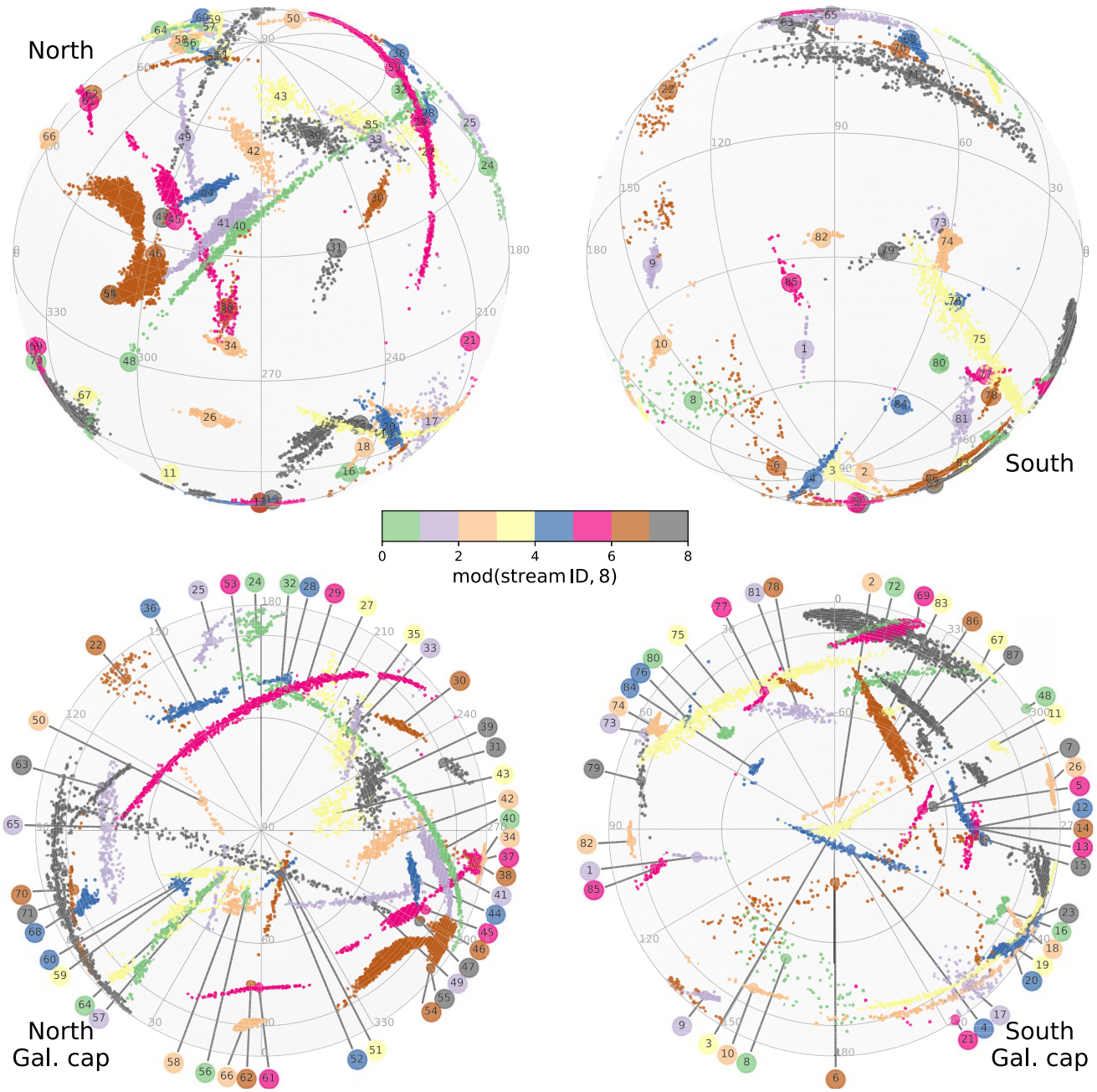

1 C-20 2 SGP-S 3 NGC288 4 ATLAS 5 Phoenix 6 Kwando 7 New-1 8 New-2 9 C-13 10 Gaia-12 11 Hydrus 12 NGC1261
13 NGC1261a 14 NGC1261b 15 Indus 16 NGC1851 17 New-3 18 New-4 19 Leiptr 20 C-12 21 New-5 22 New-6 23 NGC2298 24 C-25
25 C-11 26 NGC2808 27 New-7 28 New-8 29 New-9 30 C-10 31 New-10 32 New-11 33 Gaia-10 34 GjoII 35 C-9 36 C-24
37 New-12 38 New-13 39 Slidr 40 New-14 41 Ylgr 42 Sylgr 43 New-15 44 Gaia-7 45 Gaia-8 46 New-16 47 Fjorm 48 Orphan
49 Gaia-1 50 C-23 51 LMS-1 52 C-22 53 GD1 54 Fimbulthul 55 Fimbulthul-S 56 New-17 57 NGC5466 58 New-18 59 Gaia-6 60 New-19
61 Pal-5 62 M5 63 Kshir 64 Svol 65 Gaia-9 66 Ophiuchus 67 NGC6101 68 M92 69 NGC6397 70 Gaia-11 71 Hrid 72 C-7
73 New-20 74 New-21 75 Phlegethon 76 NGC7089 77 NGC7099 78 New-22 79 New-23 80 New-24 81 New-25 82 New-26 83 New-27 84 NGC7492
85 C-19 86 Jhelum 87 Tuc-3

Figure 6. Gallery of the stellar streams in the same projections as in Figures 1–5. The color of the points shows our chosen stream identification number in a modulo 8 representation.

where ζ and χ are the fraction of stars in the cocoon and contamination, respectively. We conservatively set $\chi = 0.01$. In our examination of the GD-1 stream in Section 9.4 below, we deduce $\zeta = 0.27$ for that system; however, to be conservative, we set $\zeta = 0.1$ for all streams in our MCMC analysis. The stream model

$$\mathcal{P}^{\rm fit}_{\rm stream} = \mathcal{P}_{\rm width} \times \mathcal{P}_{\rm color} \times \mathcal{P}_{\mu} \times \mathcal{P}_{\varpi} \times \mathcal{P}_{v} \qquad (11)$$

is exactly the same stream probability criterion as used in STREAMFINDER (Equation (2)) but ignores the luminosity

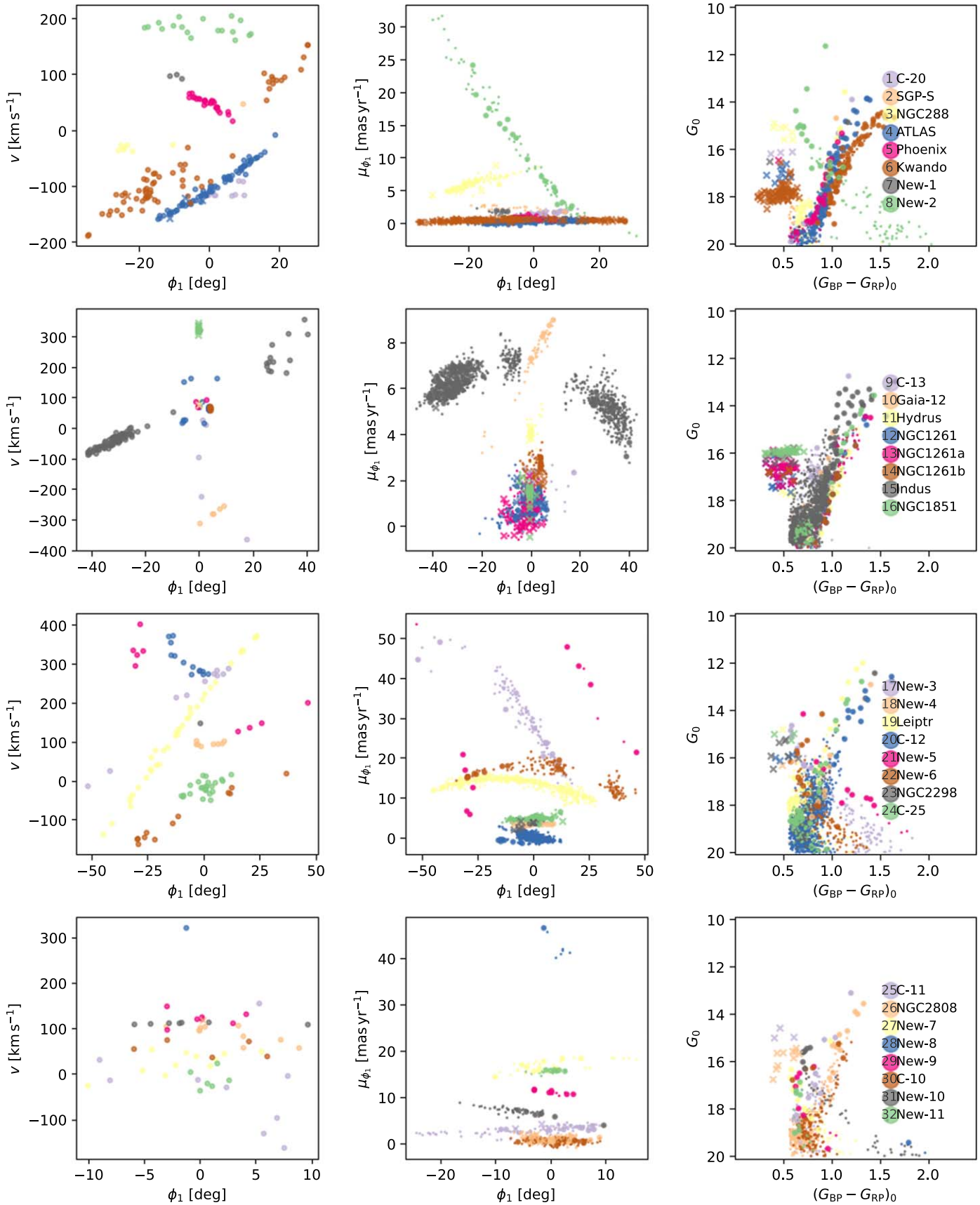

Figure 7. Kinematic profiles and color–magnitude relations of stellar streams. The left column of panels shows the heliocentric line-of-sight velocity as a function of angle ϕ_1 along the streams, while the middle column displays proper motion μ_{ϕ_1} along the ϕ_1 direction. The color–magnitude properties of the stellar populations can be seen in the right column of panels.

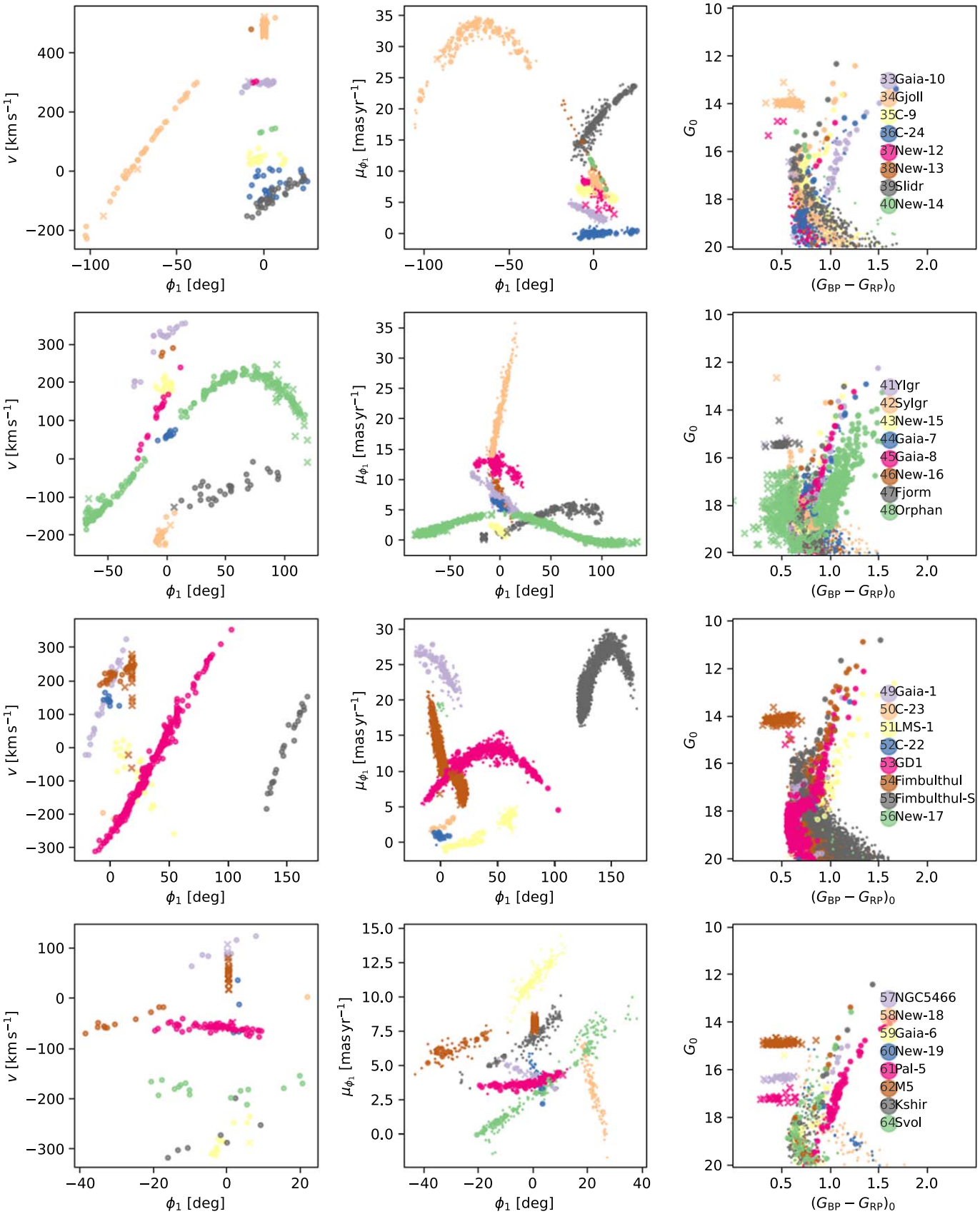

Figure 8. Continuation of Figure 7.

function information (as we are assuming at this point that the stars have been appropriately selected). Also, in contrast to STREAMFINDER, the orbital track is corrected by the function $\Delta_\Theta(\phi_1)$ introduced above, so as to better approximate the corresponding stream (these functions will be discussed in more detail in Section 7 below). The cocoon model is assumed

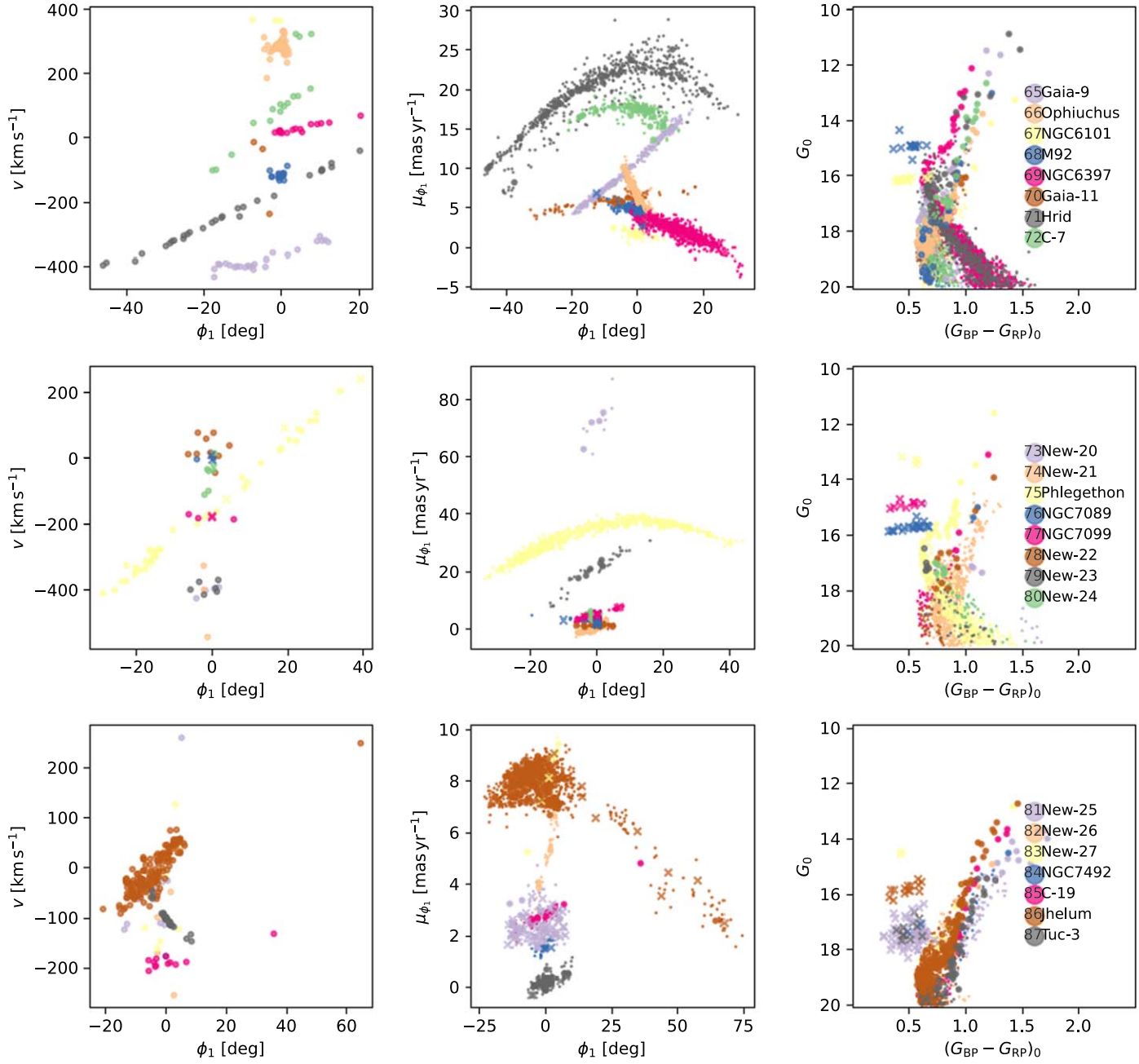

Figure 9. Continuation of Figure 7.

to be identical to the stream model, except that we widen the model dispersions by a factor of 5 in line-of-sight velocity (approximately the ratio inferred in Section 9.4 for GD-1), proper motion, distance, and width on the sky (i.e., equivalent to an intrinsic 25 km s^{-1} velocity dispersion and an intrinsic 250 pc stream width). In the present context, the contamination is clearly a very complex multidimensional function and further compounding the complexity of our model does not seem like a good idea. So instead, we adopted a pragmatic contamination model, inspired by the *good-and-bad data model* of Sivia & Skilling (2006; see their Section 8.3.2). According to their model, the *good* fraction has Gaussian residuals $R \equiv (F - D)/\sigma$ between the data D and the model prediction F given the expected dispersion σ (due to the model spread and the measurement uncertainties), while for the *bad* fraction, these residuals are simply scaled down by some factor τ (Sivia & Skilling 2006 use the symbol γ). In this way, we choose the contamination model to be exactly the same as the stream model (not the cocoon), but with $\tau = 10$, effectively inflating the σ of the stream model by that factor (for bright stars with small measurement uncertainties this corresponds to a velocity dispersion of 50 km s^{-1} and a spatial dispersion of 0.5 kpc). This renders the objective function (Equation (10)) much less sensitive to the presence of outliers, even though the assumed contamination fraction (1%) is quite small.

The $\ln \mathcal{L}_{\rm ancillary}$ term in Equation (10) is used to include constraints from ancillary data sets, all in the form of simple χ^2-like terms. So, for instance, when we force the rotation

curve of the proposed potential models $v_c^{\rm model}$ to be consistent with Galactic rotation curve measurements $v_c^{\rm Eilers}$ and associated uncertainties $\delta v_c^{\rm Eilers}$ (Eilers et al. 2019), we include

$$-\sum_{\rm data}\frac{1}{2}\left(\frac{v_c^{\rm Eilers}-v_c^{\rm model}}{\delta v_c^{\rm Eilers}}\right)^2 \quad (12)$$

in $\ln\mathcal{L}_{\rm ancillary}$. We limit the Eilers et al. (2019) rotation curve data to $R<15$ kpc, as the outer stellar disk is both substantially warped and flared beyond that radius (see, e.g., Momany et al. 2006).

Further constraints on the radial mass distribution are available thanks to studies of the terminal velocity of H I in the inner Galaxy. The high-resolution profiles of McClure-Griffiths & Dickey (2007, 2016) are conveniently measured with respect to the local standard of rest, so we can directly compare them to the predictions of the mass models

$$v_{\rm term}^{\rm model}(\ell)=\mathrm{sgn}(\sin(\ell))\,v_c(R|\sin(\ell)|)-v_c(R_\odot)\sin(\ell). \quad (13)$$

The H I terminal velocity curves as a function of angle show substantially localized bumps on scales of a few degrees (see, e.g., Figure 1 of McClure-Griffiths & Dickey 2016), implying correlated motion that our large-scale mass model cannot possibly reproduce. To mitigate against this, we decided to average the profiles over 2° intervals. Also, following McMillan (2017), we retain only those measurements with $|\sin(\ell)|>0.5$ to avoid regions that are heavily affected by the presence of the Galactic bar. We assume an uncertainty of $6.2\,\mathrm{km\,s^{-1}}$ of the terminal velocity measurements, as derived from the scatter between the measurements and the linear model fit by McClure-Griffiths & Dickey (2016).

We similarly add the datum of $71\pm6\,M_\odot\,\mathrm{pc}^{-2}$ for the vertical force at $z=1.1$ kpc above the Galactic midplane measured by Kuijken & Gilmore (1991). We also include the stellar density measurements toward the north Galactic cap of Ibata et al. (2017b) decomposed into thin and thick disk components according to photometric metallicity; the sample at Galactic latitude $b>70°$ is used (shown in their Figure 12(f)) truncated to $z<5$ kpc as their thin disk profile is noisy at larger z. As indicated in Ibata et al. (2017b), the stellar number density profiles are transformed into *relative* mass density profiles with simulations that use PARSEC isochrone models and take into account the selection function of their survey. They adopt an average age of 5 and 10 Gyr for the thin and thick disks, respectively, and note that the difference in the computed density corrections between these two ages is only 20%, implying that their measured relative vertical density profiles are not very sensitive to those reasonable assumptions on population age. The Ibata et al. (2017b) study chose not to constrain the normalization of the density profiles, so in the present work the thin and thick disk components are fit to those vertical profiles data while allowing for a free multiplicative constant.

Neither the Eilers et al. (2019) rotation curve measurements nor the long streams we have selected probe the inner regions of the Milky Way. We, therefore, chose for the present work to simply adopt the Galactic bulge component of the model previously fit by McMillan (2017). The truncation radius of the halo component is fixed at $r_t=1000$ kpc, far beyond the expected virial radius of the Milky Way.

In our explorations we realized that the data set provides constraints on the peculiar velocity of the Sun that seem plausible given published studies, but that these constraints are somewhat degenerate with the freedom we allow to models of the potential. We defer an investigation into this issue to a future contribution, and therefore, fix the peculiar velocity of the Sun to the values found by Schönrich et al. (2010). Likewise, we also fix the distance to the Galactic Center to $R_\odot=8.178$ kpc (GRAVITY Collaboration et al. 2019), and ignore the small uncertainties on this value.

We calculate the M_{200} mass of the models, defined as the mass out to a radius of r_{200} where the average interior density of the model is 200 times the critical density $\rho_c=3H^2/8\pi G$ of the universe, and we assume a Hubble parameter of $H=70\,\mathrm{km\,s^{-1}\,Mpc^{-1}}$. Clearly, the calculated M_{200} value involves a long extrapolation from the region constrained by the chosen sample of 29 streams. Nevertheless, we consider M_{200} to be a useful constraint on the models, and require the solutions to be in the range of $[0,\,2]\times10^{12}\,M_\odot$. The upper bound on M_{200} of $2\times10^{12}\,M_\odot$ corresponds to half of the Local Group mass of $4\times10^{12}\,M_\odot$ (95% upper limit) estimated by Peñarrubia et al. (2014). The other bounds are that the masses of all components, as well as the halo density flattening parameter $q_{m,h}$, should be positive.[17] The thin and thick disk scale lengths are required to be in the range of [1, 10] kpc, so we impose that the thin disk scale height should be in the range of [0.05, 0.5] kpc and the thick disk scale height should be in the range of [0.05, 5] kpc. Finally, we require that the thick disk scale height should be larger than that of the thin disk.

In our first modeling efforts we considered what we thought was the simplest useful Galaxy model, containing only a fixed bulge, a halo, and a single disk component. However, we noticed that if we left out the Ibata et al. (2017b) vertical density constraint, the resulting best solutions required a disk component with an unrealistically large scale height (∼1 kpc). This result is perhaps not surprising in retrospect since the selected streams mostly reside in halo regions at high extraplanar distance, where the effect of the thin disk is less pronounced. So, evidently, a minimal Galaxy model for our purposes also entails including a thick disk component. Because our data provide poor constraints on the potential at low Galactic latitude, we also adopt the two gas disk models proposed by McMillan (2017), which include an atomic gas disk of scale height of 85 pc and mass of $1.1\times10^{10}\,M_\odot$, as well as a molecular gas disk of scale height 45 pc and mass of $1.1\times10^{9}\,M_\odot$.

Before showing our results with this model, we next present a refined—but computationally much more costly—method that uses test particles to follow tidal dissolution in a moving Local Group potential. This model is also used to calculate the correction functions Δ_Θ employed in the orbit fitting described above.

6. Stream Fitting with Test Particles in the Local Group

Contrary to the assumptions underlying the models presented in the previous section, the Milky Way is, of course, not an isolated galaxy, but a member of the Local Group, the other major components of this grouping being the Andromeda and

[17] These bounds are implemented in the MCMC procedure simply by subtracting a very large number from $\ln\mathcal{L}$ if the limits are crossed.

Triangulum galaxies, approximately 800 kpc away, as well as the LMC, the Small Magellanic Cloud, and the Sagittarius dwarf galaxy that reside within the halo of our Galaxy. Predicting the paths of stellar streams in the Local Group requires some consideration of the combined gravitational effect of these six bodies, and perhaps additional mass concentrations depending on the particular path of the stream progenitor.

Yet, running full N-body simulations of the Local Group with a resolution sufficient to fit the observed stellar streams is far beyond current computational abilities, so we need to make some simplifying steps to tackle the problem. Here, we will assume that the major galaxies can each be modeled as moving potentials with a mass distribution that does not vary in time when viewed from their center of mass. Since this assumption becomes worse further back in time, we will only consider integrating backward for at most 5 Gyr.

We integrate the path of the Local Group members using a symplectic leapfrog scheme with direct summation of the forces from all other bodies. The major galaxies (the Milky Way, Andromeda, and the LMC) are assumed to be truncated at their (static) virial radius. This allows us to treat the bodies as point masses when considering their effect on the other Local Group galaxies that are beyond the virial radius. When including M31 or M33 (whose influence we neglect in the present work), we also take into account a dark energy term, using an additional acceleration term $\ddot{\boldsymbol{x}} = H_0^2 \Omega_\Lambda \boldsymbol{x}$, where $\boldsymbol{x}$ in this case is the radial vector from the center of mass of the Local Group.

The dynamics of the LMC and Sagittarius galaxies are particularly difficult because we expect their orbits to have been substantially affected by dynamical friction. Here, we use the Chandrasekhar dynamical friction model to integrate the massive bodies backward in time, and adopt the formula of Correa Magnus & Vasiliev (2022) to approximate the Coulomb logarithm. We have confirmed with several spot-tests that the Correa Magnus & Vasiliev (2022) method predicts well the behavior in N-body simulations of the spiraling-in path of the LMC when the Milky Way is represented by a live Navarro–Frenk–White (NFW) halo.

The orbits of the stream progenitors are integrated backward in time for a time T in this dynamic Local Group potential, starting from a trial present-day phase-space coordinate. At the initial time $-T$, we instantiate a set of $N = 10{,}000$ massless test particles that follow a spherical Plummer model (parameters: mass, scale radius).[18] We then integrate this system forward in time until the present day. However, instead of following the full N-body evolution of the progenitor, we approximate tidal dissolution as follows. We use the analytic potential of the progenitor to approximate the evolving system, so that the forces on the test particles are the sum of the forces from the Local Group galaxies, plus the force due to the progenitor. If a particle moves beyond 10 scale radii from the progenitor, it is considered to be lost, and we decrease the mass of the progenitor by $1/N$. In contrast, we assume that the Plummer scale radius a does not change during the tidal disruption. The advantage of this scheme is that it has saved us from having to follow the internal N-body dynamics of the progenitor, and it can also be parallelized trivially since the test particles are independent of each other ($\mathcal{O}(N)$ computational complexity). Our method is inspired by those of Mastrobuono-Battisti et al. (2012) and Ferrone et al. (2023), but we implement mass loss in the progenitor, as well as massive perturbers. Mastrobuono-Battisti et al. (2012) demonstrated that test-particle integration in nonvarying host globular clusters can reproduce very similar stream extent and morphology as full N-body simulations, but for the majority of the STREAMFINDER streams, we need to be able to account for the full dissolution of the progenitor.

The validity of our simplifying approximation of fixing the Plummer scale radius can be judged from Figure 10, where we show a separate N-body experiment of the evolution of a plausible GD-1 stream progenitor. For this test, we use the Galactic potential model #1 of Dehnen & Binney (1998) and integrate therein a Plummer model for 2 Gyr. Over this period of time, where the system loses almost all its mass (red profile), the half-mass–radius $r_h = (2^{2/3} - 1)^{-1/2} a$ (blue profile) remains close to constant. An equivalent result is discussed in Errani et al. (2024) for collision-less systems that follow an exponential density profile, suggesting that our simplifying assumption of $a = \text{const}$ is not unique to our choice of progenitor density profile. Note, however, that our idealized setup does not capture the effects of potential internal collisional dynamics on the progenitor structure.

We use exactly the same optimization machinery and the same objective function for the stream fits as for the orbit fits in Section 5 (except, of course, that the correction functions $\Delta\Theta$ are ignored). Unfortunately, this procedure of integrating test particles is substantially more computationally expensive to optimize: most importantly, we have to follow N times more orbits, and there are two more parameters per stream (the progenitor mass and scale radius of the Plummer model), and the global potential requires seven additional parameters (mass and initial phase-space position) for each Local Group galaxy that we aim to include the potential of. While it would be possible to reduce N, there needs to be a sufficient number of tidally disrupted particles to model a stream, and our experiments showed that below $N \approx 10^4$, the stream model could become too noisy to allow a reliable comparison to data.

In the present contribution, we will only attempt a limited exploration of the parameter space of this complex model, and defer a full stream-fitting analysis with this machinery to a future contribution.

7. Orbit–Stream Correction Functions

The test-particle model introduced in the previous section is immediately useful to us as a means to calculate the $\Delta_\Theta(\phi_1)$ correction functions needed for the corrected orbit fitting described in Section 5. We started by running the test-particle model optimization procedure with the Milky Way mass parameters fixed at the values found by McMillan (2017), and with all other Local Group galaxies set to zero mass. For the five systems with known globular cluster progenitors (Gjöll/NGC 3201, Fjörm/M68, NGC 5466, Palomar 5, and M5, i.e., streams #34, #47, #57, #61, and #62) in our sample of 29 streams, we fixed the mass and half-mass parameters at the values measured by Baumgardt & Hilker (2018), and also fixed the line-of-sight velocities at the values given by Vasiliev (2019); the distances and proper motions were allowed to vary within the uncertainties set by the measurements of Baumgardt & Vasiliev (2021) and Vasiliev (2019), respectively. For GD-1,

[18] For streams that have dwarf galaxy progenitors an exponentially truncated NFW model would be more appropriate (Errani & Navarro 2021), and would be very simple to implement into this machinery.

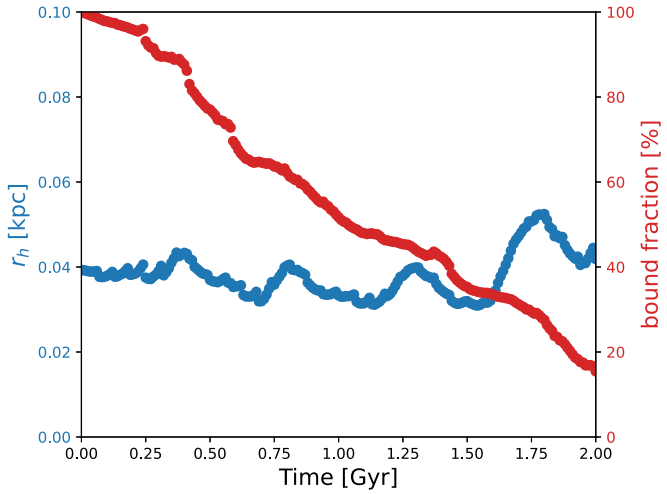

Figure 10. Tidal dissolution of an N-body GD-1 progenitor model, showing the approximate constancy of the half-mass–radius as the system loses almost all its mass. For this experiment, a Plummer sphere of 10^5 particles with a scale radius $a = 50$ pc and a mass of $3 \times 10^4\,M_\odot$ was evolved using the `falcON` (Dehnen 2002) N-body integrator. A softening length of 1 pc was adopted.

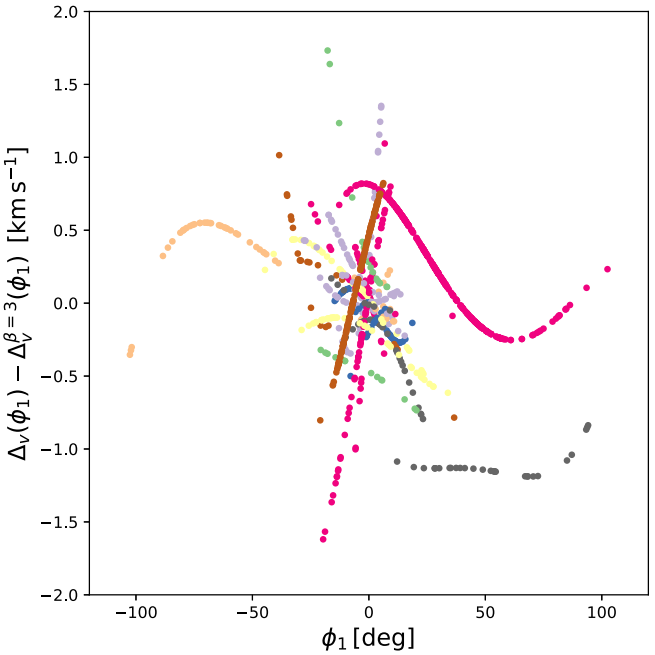

Figure 11. Difference between the line-of-sight velocity correction functions $\Delta_v(\phi_1) = v_{\rm stream} - v_{\rm orbit}$ corresponding to the most likely Milky Way model and that resulting from imposing $\beta_h = 3$. It can be seen that the correction functions differ by only $\approx$1 km s^{-1}. The points are plotted at the ϕ_1 locations of the stars in the 29 selected streams, and we again use the color map of Figure 6.

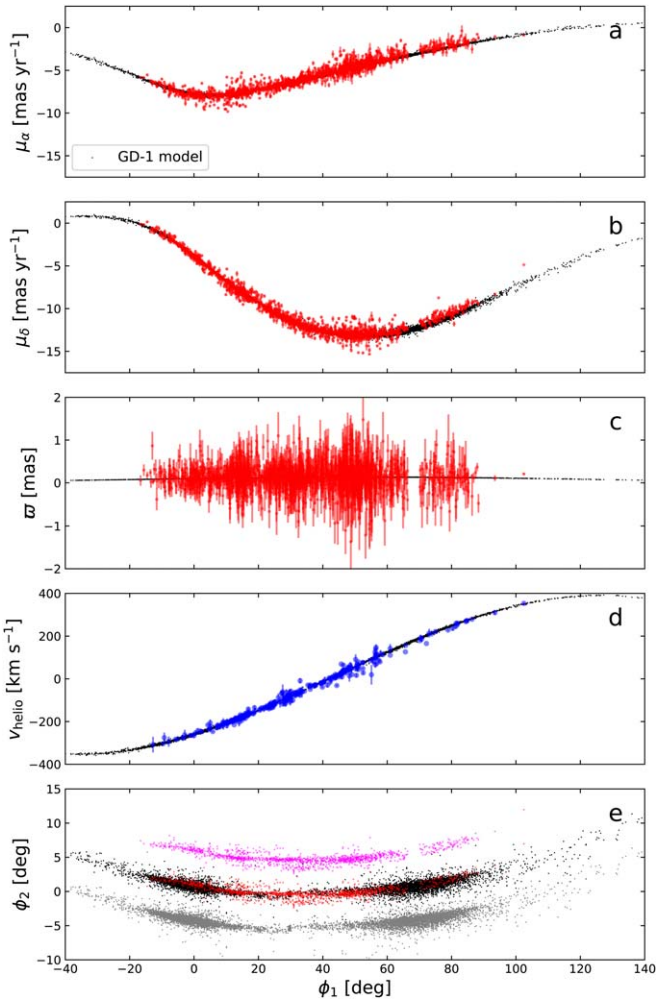

Figure 12. Comparison of the GD-1 data (stream #53, red points) with a best-fit model (black points) in a potential model that is constrained to have fixed halo power-law parameters of $\gamma_h = 1$ and $\beta_h = 3$, fixed scale heights of 0.3 and 0.9 kpc, respectively, for the thin and thick disk components, together with a fixed thick disk scale length of 3.6 kpc (all these parameters are also fixed in the McMillan 2017 model). The model fits the halo central density, halo scale parameter, the disk scale length, and the masses and relative fractions of the thin and thick disks. Although all GD-1 data are displayed, only those stars with measured radial velocity (blue points) were used in the fit. The GD-1 model has an initial mass of $3 \times 10^4\,M_\odot$, a Plummer scale length of 50 pc, and is integrated over 2.5 Gyr. To aid visual comparison, the sky positions (e) include a version of the model shifted by $-5°$ (gray) as well as the data shifted by $+5°$ (magenta) in ϕ_2. The gap in the data visible in all panels at $\phi_1 \approx 68°$ is a consequence of our choice in running `STREAMFINDER` to excise Gaia data around dense sources (in this case, M67).

we set the progenitor position to $\alpha = 157\overset{\circ}{.}74$, as will be justified below in Section 8. For the remaining 23 streams, we unfortunately have no constraint on the position of the progenitor, so it is set at the estimated midpoint of the stream ($\phi_1 = 0°$). The masses of the structures are set to the stellar mass estimates listed in Table 3, but we conservatively set a floor of $2 \times 10^4\,M_\odot$ to these values (approximately the mass of our estimate of the Palomar 5 progenitor). For these streams, we also assume a progenitor Plummer scale length of 30 pc. The correction function $\Delta_\Theta(\phi_1)$ is then calculated independently for each observable Θ (i.e., sky position, distance modulus, line-of-sight velocity, and proper motions) as a fourth-order polynomial fit to the best-fit stream minus the corresponding progenitor orbit. This $\Delta_\Theta(\phi_1)$ is subsequently used in the corrected orbit-fitting algorithm to find an improved Milky Way mass model. We repeated this procedure a further two times, rederiving $\Delta_\Theta(\phi_1)$ for the best mass model, and rerunning the MCMC search of Section 5. We stopped at the third iteration as the derived Milky Way parameters were statistically identical to those in the second iteration.

The procedure we have devised makes several simplifications to speed up the calculations, including the use of a single correction function $\Delta_\Theta(\phi_1)$ for each stream during an MCMC run. Ideally, a new correction function should be calculated for each stream for every set of Milky Way and stream parameters

Table 1
The First 10 Rows of the STREAMFINDER Catalog of 24,540 Stars Detected in Gaia DR3

DR3 ID	α (deg)	δ (deg)	ϖ (mas)	μ_α (mas yr^{-1})	μ_δ (mas yr^{-1})	G_0 (mag)	$(G_{BP}-G_{RP})_0$ (mag)	v_h (km s^{-1})	δv_h (km s^{-1})	s	s_{ID}
(1)	(2)	(3)	(4)	(5)	(6)	(7)	(8)	(9)	(10)	(11)	(12)
2746748683780680704	0.131771	8.022269	−0.523	−0.338	1.390	19.35	0.74	⋯	⋯	⋯	1
2746696319539384320	0.328548	7.886247	0.045	−0.683	1.425	19.48	0.59	⋯	⋯	⋯	1
2745893989584959488	0.714213	7.207192	0.090	−0.553	1.405	15.83	1.04	−115.03	0.35	13	1
2745895810651091456	0.714858	7.301568	−0.001	−0.439	1.322	18.75	0.83	⋯	⋯	⋯	1
2745605054248759296	0.992495	6.646490	−0.413	−0.760	1.801	19.04	0.68	⋯	⋯	⋯	1
2745591005412035584	1.135276	6.569216	−0.055	−0.251	1.656	18.00	0.89	⋯	⋯	⋯	1
2742045419713596416	1.655054	5.419648	0.186	−0.531	1.219	19.22	0.75	⋯	⋯	⋯	1
2742028759537330176	1.740425	5.219596	0.047	−0.572	1.522	19.59	0.71	⋯	⋯	⋯	1
2740941544398892032	2.436206	4.142149	0.545	−0.651	1.321	18.60	0.79	⋯	⋯	⋯	1
2740973155358226432	2.751825	4.308954	−0.239	−0.391	1.247	19.20	0.68	⋯	⋯	⋯	1

Note. Column (1) provides the Gaia DR3 identification of the star, columns (2)–(6) list the EDR3 equatorial coordinates α and δ, parallax ϖ and proper motions μ_α(*cos(δ)), μ_δ. The extinction-corrected magnitude G_0, and color $(G_{BP}-G_{RP})_0$ used in STREAMFINDER are listed in columns (7) and (8). Columns (9) and (10) list the best-measured heliocentric line-of-sight velocity, as derived from the corresponding source "s" in column (11). In column (11), the source identifications "s" are: 1 = APOGEE, 2 = GALAH, 3 = Gaia RVS, 4 = LAMOST, 5 = S5, 6 = SDSS, 7 = BOSS, 8 = ESPaDOnS (this work), 9 = AAOmega (from Ibata et al. 2017a), 10 = FLAMES (from Ibata et al. 2017a), 11 = UVES (from Odenkirchen et al. 2009), 12 = EFOSC (this work), 13 = UVES (this work), 14 = INT (this work), 15 = Yuan et al. (2022b), 16 = Li et al. (2021), 17 = Caldwell et al. (2020), 18 = T. S. Li et al. (2018), 19 = Koposov et al. (2018), 20 = G.-W. Li et al. (2018), 21 = Simon et al. (2020), 22 = Walker et al. (2015), 23 = VizieR, 24 = GES, 25 = DESI. Finally, column (12) provides a unique stream identification label.

(This table is available in its entirety in machine-readable form.)

examined in the MCMC search.[19] In Figure 11, we show the difference between the correction functions in the best-fit model, and in the best model when imposing a halo outer power-law parameter of $\beta_h = 3$ (so as to be consistent with an NFW profile). In these two quite different Milky Way models, the correction functions are very similar, within $\approx$1 km s^{-1} in line-of-sight velocity (which is the easiest observable to interpret when comparing streams, as there is no distance dependence).

8. Stream-fitting Results

We begin by attempting to fit a static axisymmetric model to the Galaxy, ignoring any stellar stream data; to this end, we use the objective function in Equation (10), with the first term on the right-hand side set to zero (i.e., we only fit to the ancillary data). For this first experiment, we fix the halo power-law parameters to $\gamma_h = 1$ and $\beta_h = 3$ so as to reproduce the expected behavior of dark matter halos (Navarro et al. 1997), set the halo matter flattening to $q_{m,h} = 1$, set the thin and thick disk scale heights to 0.3 and 0.9 kpc respectively, and set the thick disk scale length to 3.6 kpc; these are all choices that were adopted by McMillan (2017). The main difference with respect to that study is that we are using the Eilers et al. (2019) rotation curve measurements. We find a thin disk scale length of $h_{R,d} = 2.22 \pm 0.07 (2.53 \pm 0.14)$ kpc, a halo scale radius of $r_{0,h} = 12.4 \pm 2.0 (19.0 \pm 4.9)$ kpc, a total stellar mass of $M_\star = 4.63 \pm 0.33 (5.43 \pm 0.57) \times 10^{10}\, M_\odot$, $M_{200} = 0.86 \pm 0.09 (1.3 \pm 0.3) \times 10^{12}\, M_\odot$, and a mass interior to 50 kpc of $M_{R<50} = 0.41 \pm 0.02 \times 10^{12}\, M_\odot$, where the values in brackets are those reported by McMillan (2017), when available. Figure 6 of McMillan (2017) shows their posterior PDF of $M_{R<50}$ peaking at a considerably higher mass of $M_{R<50} \approx 0.51 \times 10^{12}\, M_\odot$. Our aim with this test was to obtain a baseline for the following stream analysis, and to explore how the improved data changes these inferences.

We now repeat this experiment, but add in the GD-1 stream, which is the structure for which we have the most numerous data (323 stars with line-of-sight velocity measurements and three RR Lyrae). This time we allow the halo mass flattening parameter $q_{m,h}$ to also be free. With this data set, we find $h_{R,d} = 2.16 \pm 0.08$ kpc, $q_{m,h} = 0.86 \pm 0.05$, $r_{0,h} = 10.7 \pm 1.6$ kpc, $M_\star = 4.24 \pm 0.35 \times 10^{10}\, M_\odot$, $M_{200} = 0.77 \pm 0.07 \times 10^{12}\, M_\odot$ and $M_{R<50} = 0.39 \pm 0.01 \times 10^{12}\, M_\odot$, and the corresponding stream fit is shown in Figure 12. While the stream model captures the large-scale behavior of the kinematics of GD-1, it possesses some small, yet systematic, deviations from the proper motion trend in the data, especially in the range of $60° < \phi_1 < 90°$. The density distribution of the model particles (panel (e)) is also not a good match to the data, given that the model produces two high-density peaks at $\phi_1 \approx 0°$ and $\phi_1 \approx 70°$, and a small remnant (at $\phi_1 = 29.^\circ7$) still remains, but is not present in reality. However, the large peaks in the data at $\phi_1 \approx 10°$ and $\approx 50°$, which we ascribed in an earlier contribution (Ibata et al. 2020b) to epicyclic motion, can be seen to have counterparts in the model. Given this match, and also given that $\phi_1 = 32.^\circ4$ corresponds to the stellar mass-weighted midpoint of the stream,[20] we consider $\alpha = 157.^\circ74$ to be currently the best estimate for the position of the center of the GD-1 progenitor. Henceforth, we fix the present-day position of GD-1's progenitor to that location.

We continue the procedure of rendering the model more realistic, adding in the five streams in our sample that have known globular cluster progenitors (Gjöll/NGC 3201, Fjörm/M68, NGC 5466, Palomar 5, and M5). The phase-space parameters of these objects, and in particular their distances, are very well constrained, which makes them especially powerful probes of the Galactic potential compared to a similarly sized sample of streams. In addition to the previously

[19] Of course, this would be pointless in practice, as it would be more accurate and more computationally efficient to simply use the test-particle machinery developed in Section 6 and forgo the corrected orbit-fitting approach altogether.

[20] We calculate this midpoint by assuming that the survey is complete to $G_0 = 20$ mag, and correct for missing stars given the distance model and the metallicity listed in Table 3. However, we did not correct for the masked region around M67.

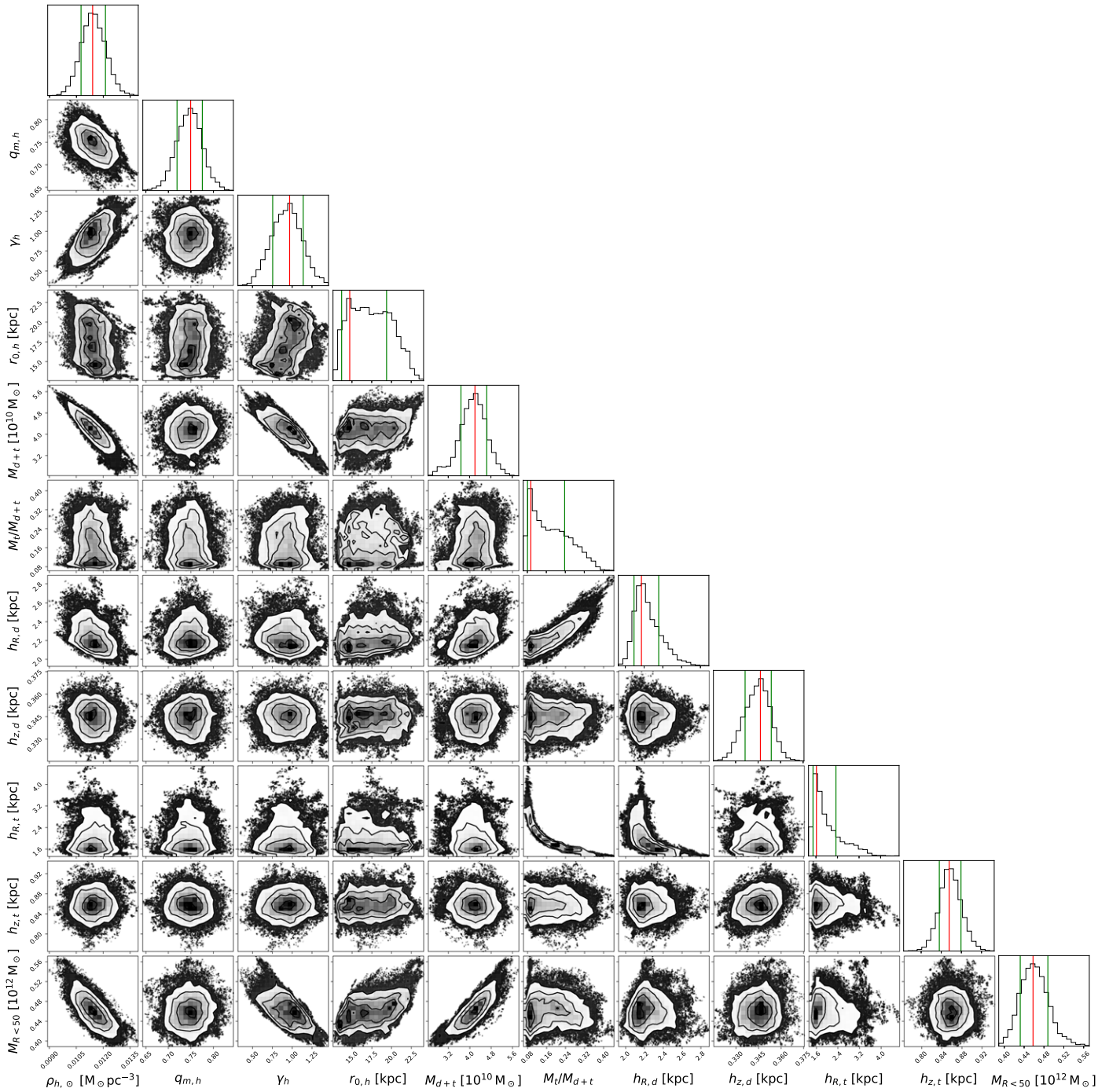

Figure 13. Correlations between Milky Way parameters in a six-component Galaxy model with fixed bulge and gaseous disks, but free halo (four parameters, with fixed $\beta_h = 3$), thin disk (three parameters), and thick disk (three parameters). The useful quantity $M_{R<50}$ is not a fitting parameter, but is derived from the mass model determined by the other parameters. This mass model determines the potential in which 29 stream structures are fit. The red vertical line in each histogram marks the mode of the distribution. Using this mode, each distribution is cut into two subamples, and the green lines show the 68th percentile lowest (left of the peak) and 68th percentile highest point (right of the peak) of the two subsamples. The contour lines in the correlation panels encompass 0.5σ, 1σ, 1.5σ and 2σ confidence regions.

fitted Galactic parameters, the scale heights of the thin and thick disk components, the scale length of the thick disk, and the halo inner power exponent are also allowed to vary. Compared to the least constrained model we present below, only the halo outer power-law parameter remains fixed at $\beta_h = 3$. The resulting fit has $h_{R,d} = 2.31 \pm 0.14$ kpc, $h_{z,d} = 345 \pm 9$ pc, $h_{R,t} = 2.02 \pm 0.42$ kpc, $h_{z,t} = 859 \pm 25$ pc, $\gamma_h = 0.89 \pm 0.19$, $q_{m,h} = 0.75 \pm 0.03$, $r_{0,h} = 22.1 \pm 2.8$ kpc, $M_\star = 5.60 \pm 0.51 \times 10^{10}\,M_\odot$, $M_{200} = 1.42 \pm 0.25 \times 10^{12}\,M_\odot$, and $M_{R<50} = 0.50 \pm 0.03 \times 10^{12}\,M_\odot$. The most striking difference

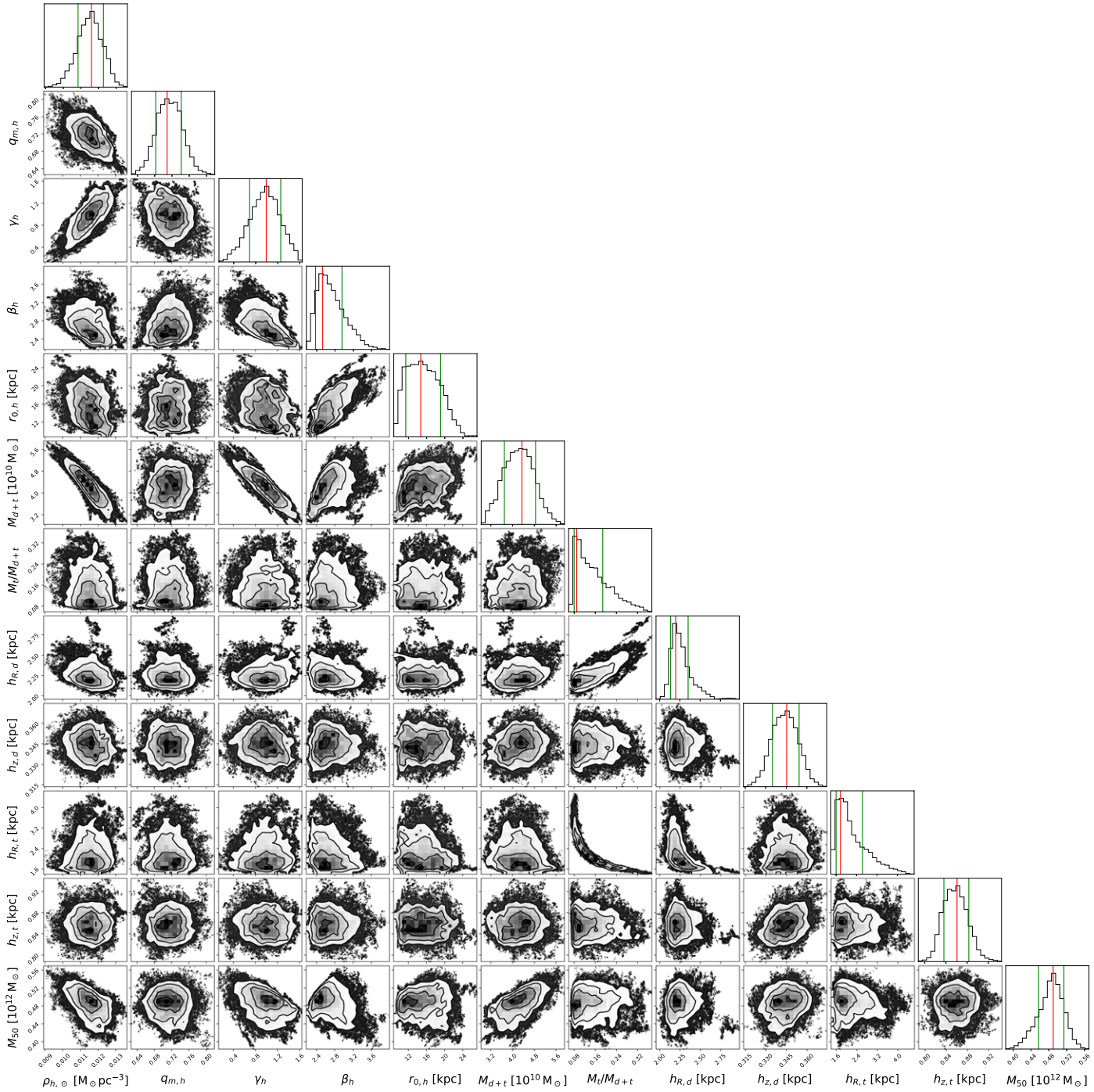

Figure 14. As in Figure 13, but here the halo outer power-law parameter β_h is also allowed to vary, for a total of 11 free parameters of the Galactic mass model.

to the previous fit is that the stream kinematics require the thick disk scale length to be much shorter than the 3.6 kpc measured by Jurić et al. (2008) and assumed by McMillan (2017); with a shorter thick disk scale length the halo scale radius $r_{0,h}$ becomes longer.

Exactly the same procedure is repeated, but this time using the full sample of 29 streams. As before, the Galactic potential model has a fixed bulge and gaseous disks, but a free halo, thin disk, and thick disk. The results of the MCMC exploration with the halo outer power-law parameter set to $\beta_h = 3$ are shown in Figure 13, while in Figure 14, β_h is also allowed to vary. Table 2 provides the summary statistics of the two experiments. We note that some of the marginalized distributions are clearly highly skewed, so the mean and rms values can be misleading. So instead, we report the distribution mode, which we find as follows: using the binning scheme shown in Figures 13 and 14 (30 bins between the minimum and maximum values), we identify the peak bin, and refine the position of the mode assuming that the distribution is locally quadratic over the region of the peak and the two adjacent bins. The marginalized distributions are then divided into two subsets, containing the data with lower and higher values than the mode, and in each

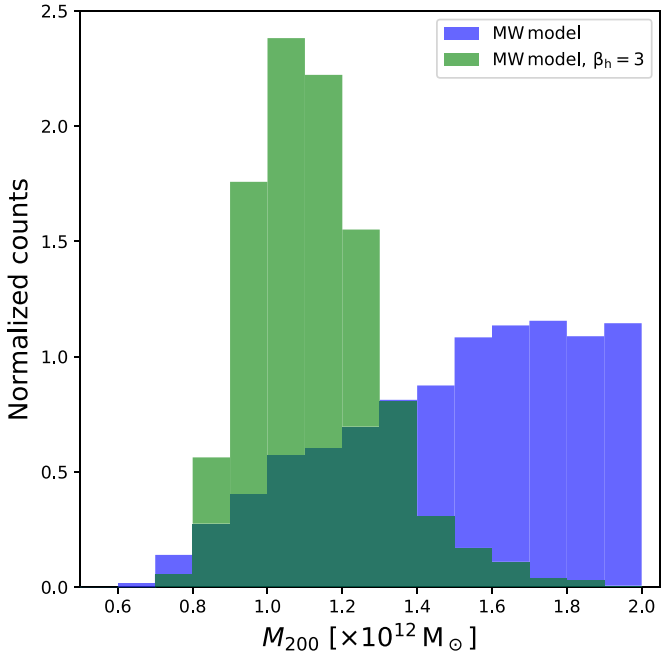

Figure 15. The total M_{200} masses of the Milky Way solutions shown in Figures 13 (green) and 14 (blue).

subset, we respectively find the position of the datum that is the 68.27% lowest and the 68.27% highest, and consider these values as the 1σ confidence intervals.

The halo mass flattening turns out to be very well constrained with $q_{m,h} = 0.749^{+0.026}_{-0.030}(0.709^{+0.033}_{-0.026})$, where the value in brackets corresponds to the fit in which β_h is allowed to vary. Interestingly the (the negative of) the inner power-law slope of the halo is close to the universal NFW profile found in cosmological dark matter simulations. Nominally, we find a shallower outer power-law profile $\beta_h = 2.53^{+0.42}_{-0.16}$, but one that is consistent with the NFW profile at 1σ. The values of the halo scale radius $r_{0,h} = 14.7^{+4.7}_{-1.0}(14.7^{+4.4}_{-3.3})$ kpc are closely consistent, although we note that the maximum-likelihood solutions are larger: $r_{0,h} = 21.4(19.5)$ kpc. We find that $r_{0,h}$ is strongly correlated with β_h, such that larger-scale radii require steeper outer power-law slopes.

The MCMC chain revealed strong correlations between the disk scale lengths and the central disk surface densities, and we also found that the combined mass of the disks $M_{d+t} = 4.20^{+0.44}_{-0.53}(4.34^{+0.50}_{-0.65}) \times 10^{10}\,M_\odot$ is much better constrained than that of the individual components. Likewise, we found that the local halo density $\rho_{h,\odot}$ is much better constrained than the central halo density $\rho_{0,h}$. These realizations motivated our use of the combination of parameters shown in Figures 13 and 14. (The central surface density of the disk can be recovered simply using the fact that the total mass of an exponential disk is $M = 2\pi\Sigma h_R^2$, while the central density of the halo is related to the local density via Equation (9).) For the thin and thick disk components, respectively, the scale heights are found to be $h_{z,d} = 0.347^{+0.007}_{-0.010}(0.345^{+0.009}_{-0.010})$ kpc and $h_{z,t} = 0.856^{+0.030}_{-0.020}(0.861^{+0.022}_{-0.025})$ kpc with scale lengths of $h_{R,d} = 2.172^{+0.184}_{-0.079}(2.198^{+0.153}_{-0.062})$ kpc and $h_{R,t} = 1.62^{+0.72}_{-0.13}(1.77^{+0.86}_{-0.17})$ kpc. The mass within $R = 50$ kpc of these two models is $M_{R<50} = 0.458^{+0.030}_{-0.026}(0.490^{+0.024}_{-0.033}) \times 10^{12}\,M_\odot$. Determining M_{200}, however, requires a substantial extrapolation out of the region where we have data. The distribution of M_{200} masses of these Milky Way models as derived from the MCMC chains is shown in Figure 15. The model with unconstrained β_h is clearly affected by the imposed limit of $M_{200} < 2 \times 10^{12}\,M_\odot$. For this reason, we prefer the $\beta_h = 3$ model, although most of the other properties of the two models are consistent.

Table 2
Statistics of the Parameters of the MCMC Chains Shown in Figures 13 and 14 Derived from Fitting a Flexible Galactic Model with the Sample of 29 Streams

Quantity	$\beta_h = 3$	$\mathcal{L}_{\max}^{\beta_h=3}$	β_h = free	$\mathcal{L}_{\max}^{\beta_h=\text{free}}$
$\rho_{h,\odot}\left[\frac{M_\odot\,\mathrm{pc}^{-3}}{1000}\right]$	11.4 ± 0.7	11.4	$11.6^{+0.7}_{-0.8}$	11.2
$q_{m,h}$	$0.749^{+0.026}_{-0.030}$	0.735	$0.709^{+0.033}_{-0.026}$	0.727
γ_h	$0.97^{+0.17}_{-0.21}$	1.03	$0.99^{+0.26}_{-0.30}$	1.14
β_h	3	3	$2.53^{+0.42}_{-0.16}$	2.54
$r_{0,h}$[kpc]	$14.7^{+4.7}_{-1.0}$	21.4	$14.7^{+4.4}_{-3.3}$	19.5
$M_{d+t}[10^{10}\,M_\odot]$	$4.20^{+0.44}_{-0.53}$	4.17	$4.34^{+0.50}_{-0.65}$	4.27
M_t/M_{d+t}	$0.095^{+0.143}_{-0.014}$	0.201	$0.09^{+0.10}_{-0.01}$	0.14
$h_{R,d}$[kpc]	$2.172^{+0.184}_{-0.079}$	2.241	$2.198^{+0.153}_{-0.062}$	2.251
$h_{z,d}$[kpc]	$0.347^{+0.007}_{-0.010}$	0.348	$0.345^{+0.009}_{-0.010}$	0.349
$h_{R,t}$[kpc]	$1.62^{+0.72}_{-0.13}$	1.74	$1.77^{+0.86}_{-0.17}$	2.07
$h_{z,t}$[kpc]	$0.856^{+0.030}_{-0.020}$	0.858	$0.861^{+0.022}_{-0.025}$	0.860
$M_{R<50}[10^{12}\,M_\odot]$	$0.458^{+0.030}_{-0.026}$	0.477	$0.490^{+0.024}_{-0.033}$	0.518
$M_{200}[10^{12}\,M_\odot]$	$1.09^{+0.19}_{-0.14}$	1.24	$1.70^{+0.20}_{-0.49}$	2.00
$M_d[10^{10}\,M_\odot]$	$3.44^{+0.44}_{-0.54}$	3.34	$3.52^{+0.54}_{-0.51}$	3.65
$M_t[10^{10}\,M_\odot]$	$0.40^{+0.61}_{-0.09}$	0.84	$0.39^{+0.43}_{-0.07}$	0.62

Note. The first two sets of values use a fixed value $\beta_h = 3$ for the halo outer power-law parameter, while the final two sets of columns are for the experiment where β_h is allowed to be free. The derived model masses are listed on the final four rows of the table. The $\mathcal{L}_{\max}$ columns show the parameter values of the highest likelihood datum in the MCMC chains.

The fitted orbits of the progenitors of the 29 streams integrated in the best-fit potential from Figure 14 are shown in Figure 16. These orbits can be seen to approximate quite closely the observational data, demonstrating that the Δ_Θ correction functions are not required to be large for these systems. Similarly, in Figure 17, we compare these orbits to the simulated streams resulting from the test-particle integrations in the same potential, which again shows a close correspondence. Our fitting procedure has clearly managed to encapsulate the large-scale properties of the kinematic, and hence, of the dynamical behavior of this sample of streams.

9. Gaia DR3 Detections

Many of the structures displayed in Figures 1–9 were presented previously in Papers I and II, but 28 are new detections (the objects labeled "New" in Table 3 and stream #11 emanating from the Hydrus dwarf galaxy, Koposov et al. 2018). We have verified that they do not correspond to previously reported detections in the compendium of Mateu (2023) [21] or in the phase-space analysis of Dodd et al. (2023).

As may be expected, the stream-like structures discovered in each new Gaia data release generally have a smaller number of member stars than those found in earlier releases, simply because more populated streams were easier to find first. And despite our efforts in trying to obtain follow-up spectroscopy, in 16 of the new streams we have secured fewer than five radial velocity measurements. However, some of the new features

[21] We note that stream #2 corresponds to the "SGP-S" structure discovered by Yang et al. (2022) that is not present in the Mateu (2023) catalog.

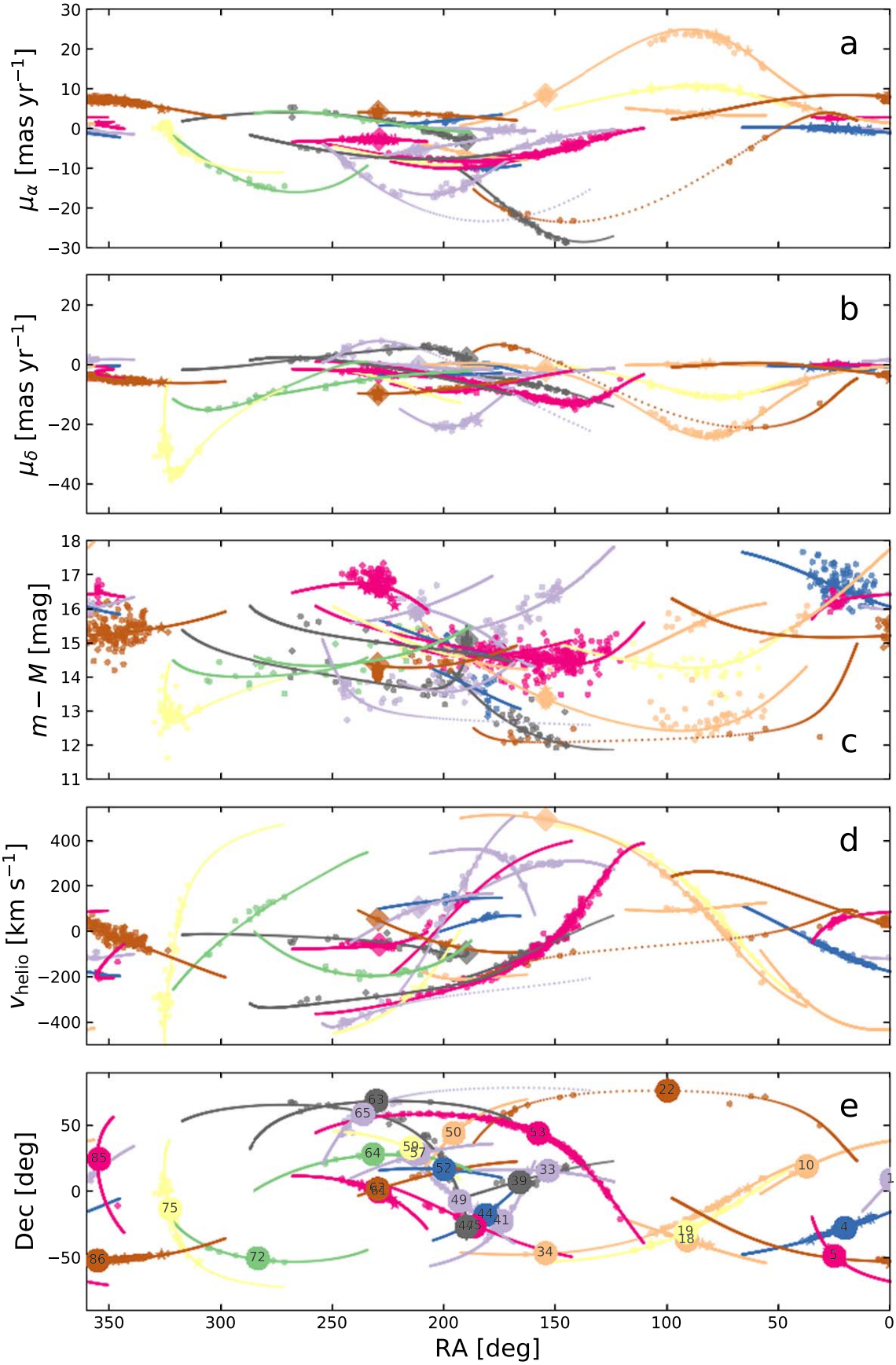

Figure 16. Orbital fits to the sample of 29 long streams integrated in the best potential model with β_h allowed to vary. The large and small four-cornered markers show, respectively, the positions of the center of globular clusters and RR Lyrae. The filled circles are stars in the streams with measured line-of-sight velocities. For each parameter on the ordinate axes, we show the corresponding behavior of the best-fit orbits. The color scheme of Figure 6 is used here.

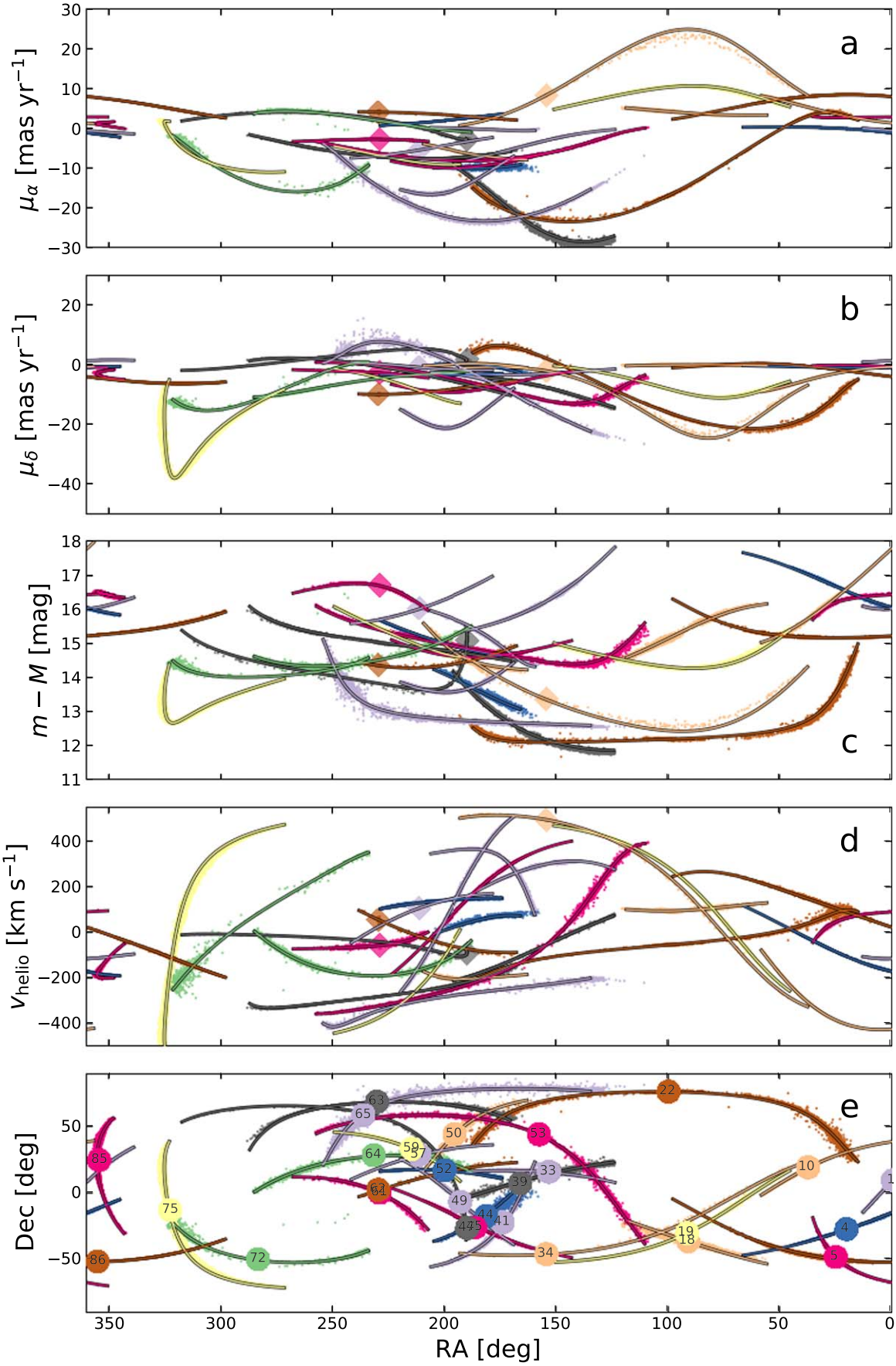

Figure 17. As in Figure 16, but comparing the progenitor orbits to the test-particle stream simulations.

Table 3
Streams Detected in Gaia DR3

s_{ID}	Name	Sample	α_0	α_{pole}	δ_{pole}	n	n_v	$M_\star$ ($M_\odot$)	$\langle$[Fe/H]$\rangle$	References	Remarks
(1)	(2)	(3)	(4)	(5)	(6)	(7)	(8)	(9)	(10)	(11)	(12)
1	C-20	1	0.561	275.038	−30.9	29	8	1200	−2.93	(1)	…
2	SGP-S	0	6.705	273.23	−5.703	36	1	530	−2.22	(2)	…
3	NGC 288	0	13.188	101.35	1.686	173	7	2200	−1.32	(3)	…
4	ATLAS	1	20.185	75.623	47.653	208	80	19,000	−2.2	(4)	…
5	Phoenix	1	24.341	309.372	12.542	58	26	3000	−2.7	(5)	…
6	Kwando	0	24.930	112.058	9.835	138	62	40,000	−2.29	(6)	Very wide, rough [Fe/H] estimate
7	New-1	0	27.124	296.02	−1.042	11	3	420	−1.85	(2)	…
8	New-2	0	34.127	53.727	−85.092	90	18	73	−2.07	(7)	…
9	C-13	0	35.678	311.207	−6.984	100	5	750	−0.25	(8)	Velocities unclear, strange CMD
10	Gaia-12	1	37.357	147.363	43.851	46	5	1200	−3.28	(2)	…
11	Hydrus	0	37.389	63.965	9.619	39	14	7700	−3.48	(2)	New stream of known structure
12	NGC 1261	0	48.068	18.701	31.13	173	23	8100	−1.27	(3)	Velocities messy, orbit apocenter
13	NGC 1261a	0	48.068	153.876	−10.473	136	4	9700	−1.27	(3)	Related to N1261?
14	NGC 1261b	0	48.068	84.128	32.219	70	12	5100	−1.27	(3)	Related to N1261?
15	Indus	0	56.206	38.115	19.901	1021	96	24,000	−2.09	(9)	…
16	NGC 1851	0	78.528	151.161	19.287	105	11	3400	−1.18	(3)	…
17	New-3	0	82.663	254.437	−72.963	120	10	120	−2.71	(10)	Two clumps?
18	New-4	1	90.988	51.229	45.719	29	8	730	−1.76	(2)	…
19	Leiptr	1	91.505	152.738	39.307	412	37	3000	−2.17	(2)	…
20	C-12	0	94.401	289.858	−59.422	929	13	14,000	−1.34	(10)	Two overlapping structures?
21	New-5	0	98.455	249.927	−87.804	13	9	16	−1.02	(2)	Two structures?
22	New-6	1	99.776	106.87	−14.425	146	12	340	−2.18	(7)	…
23	NGC 2298	0	102.248	137.971	48.3	125	1	2000	−1.92	(3)	…
24	C-25	0	112.659	324.848	44.684	121	25	1300	−2.3	(1)	Related to C-11?
25	C-11	0	117.062	349.03	24.975	112	9	1100	−2.91	(1)	Velocities unclear
26	NGC 2808	0	138.013	171.607	21.534	292	10	7300	−1.14	(3)	…
27	New-7	0	139.625	318.111	66.353	37	11	110	−2.23	(7)	Velocities unclear
28	New-8	0	142.991	237.5	6.097	7	1	3	−1.99	(7)	…
29	New-9	0	144.479	318.071	58.997	10	7	38	−1.95	(7)	…
30	C-10	0	145.970	55.813	5.518	158	5	1800	−0.91	(8)	Thick RGB
31	New-10	0	147.682	61.538	17.134	47	7	100	−0.99	(10)	…
32	New-11	0	153.299	234.748	−11.648	18	6	110	−2.03	(7)	Velocities unclear
33	Gaia-10	1	153.312	156.208	−74.386	141	26	7600	−1.4	(1)	…
34	Gjoll	1	154.403	158.539	43.545	607	40	2100	−1.63	(3)	…
35	C-9	0	155.889	115.351	−66.055	183	35	630	−0.72	(1)	Several clumps?
36	C-24	0	158.186	228.19	−12.131	244	27	2700	−0.93	(1)	Velocities unclear
37	New-12	0	161.861	84.236	14.306	89	3	580	−1.85	(2)	…
38	New-13	0	162.209	264.091	−13.901	47	1	250	−1.19	(2)	High velocity
39	Slidr	1	166.076	92.169	−64.021	330	34	840	−1.7	(1)	…
40	New-14	0	170.248	69.207	−26.38	18	4	28	−0.95	(2)	Compact
41	Ylgr	1	174.004	256.584	17.379	919	20	11,000	−2.09	(7)	…
42	Sylgr	0	176.261	273.255	−60.454	256	33	700	−2.92	(11)	High-velocity scatter
43	New-15	0	178.134	66.201	58.999	152	23	960	−2.01	(7)	…
44	Gaia-7	1	181.295	78.993	−35.727	282	15	1300	−0.88	(10)	…
45	Gaia-8	1	186.342	305.604	−48.129	453	18	3600	−1.77	(10)	…
46	New-16	0	188.285	102.418	5.746	44	3	170	−1.62	(2)	…
47	Fjorm	1	189.867	103.086	19.455	297	29	1700	−2.23	(3)	…
48	Orphan	0	191.105	68.052	−15.708	867	247	130,000	−1.9	(12)	Massive system
49	Gaia-1	1	192.56	287.833	−35.545	200	28	1100	−1.8	(7)	…
50	C-23	1	195.564	122.347	−16.78	29	6	310	−2.36	(1)	…
51	LMS-1	0	198.23	43.633	62.255	358	29	15,000	−2.09	(13)	Massive and wide system
52	C-22	1	199.904	56.016	68.974	39	11	470	−2.05	(8)	…
53	GD-1	1	200	214.928	−29.881	1468	323	14,000	−2.49	(1)	…
54	Fimbulthul	0	201.697	304.173	−22.859	3724	29	16,000	−1.53	(3)	Massive system
55	Fimbulthul-S	0	201.697	16.148	1.199	1734	25	4400	−1.53	(10)	Massive system
56	New-17	0	210.104	147.375	−50.685	13	0	29	−2.35	(2)	…
57	NGC5466	1	211.364	161.594	−50.069	43	6	1900	−1.98	(3)	…
58	New-18	0	214.041	302.311	−1.888	107	1	280	−0.94	(2)	…
59	Gaia-6	1	214.600	268.951	−41.694	145	14	1800	−1.53	(1)	…
60	New-19	0	221.839	294.781	−22.535	40	4	100	−0.79	(2)	Compact, velocities unclear
61	Pal-5	1	229.022	320.298	−54.042	129	69	17,000	−1.41	(3)	…
62	M5	1	229.638	325.223	63.075	91	11	710	−1.29	(3)	…

Table 3
(Continued)

s_{ID}	Name	Sample	α_0	α_{pole}	δ_{pole}	n	n_v	$M_\star$ ($M_\odot$)	$\langle$[Fe/H]$\rangle$	References	Remarks
(1)	(2)	(3)	(4)	(5)	(6)	(7)	(8)	(9)	(10)	(11)	(12)
63	Kshir	1	230.196	229.22	−21.937	141	7	2200	−1.83	(7)	…
64	Svol	1	231.711	28.918	60.957	234	16	2000	−1.98	(1)	…
65	Gaia-9	1	236.238	169.091	−13.272	233	25	950	−2.21	(1)	…
66	Ophiuchus	0	242.576	18.564	−79.685	391	72	4800	−1.98	(3, 14)	…
67	NGC6101	0	246.451	227.979	16.954	94	3	4800	−1.98	(3)	…
68	M92	0	259.281	232.737	−43.4	202	23	2100	−2.31	(3)	…
69	NGC6397	0	265.175	268.821	35.811	1207	17	2500	−2.02	(3)	…
70	Gaia-11	0	267.612	195.778	−15.134	84	3	1100	−1.19	(2)	Strange CMD, velocities unclear
71	Hrid	0	280.228	187.604	2.034	666	29	2000	−1.13	(7)	…
72	C-7	1	283.419	76.064	−35.517	239	16	1500	−1.52	(10)	Two superposed streams
73	New-20	0	314.963	50.439	18.37	12	4	8	−1.76	(15)	…
74	New-21	0	316.569	243.966	−56.299	762	3	7000	−0.87	(2)	High velocity
75	Phlegethon	1	322.720	55.023	−8.319	632	41	1700	−2.19	(8)	…
76	NGC7089	0	323.363	235.973	72.865	15	2	300	−1.65	(3)	…
77	NGC7099	0	325.092	79.501	−44.028	54	3	680	−2.27	(3)	…
78	New-22	0	325.847	211.35	−34.781	55	10	580	−0.98	(2)	Velocities unclear
79	New-23	0	329.825	188.254	66.646	44	6	120	−2.25	(8)	…
80	New-24	0	334.183	59.385	20.639	56	7	170	−0.64	(16)	Compact, velocities unclear
81	New-25	0	335.959	50.194	23.447	121	12	18,000	−1.68	(2)	Velocities unclear, superposed streams?
82	New-26	0	341.875	23.599	−51.695	43	4	300	−0.17	(2)	Velocities unclear
83	New-27	0	342.224	80.278	−5.92	37	8	410	−2.08	(2)	Velocities unclear
84	NGC7492	0	347.111	89.005	−34.892	26	1	3300	−1.78	(3)	…
85	C-19	1	354.356	81.45	−6.346	46	12	3200	−3.58	(1)	…
86	Jhelum	1	355.231	5.299	37.216	986	160	17,000	−2.12	(9)	…
87	Tuc-3	0	359.150	176.704	−30.396	102	34	12,000	−2.49	(17)	…

Note. Columns (1) and (2) list the identification number s_{ID} and name of the stream; a value of "1" in column (3) marks whether the stream is part of the chosen sample of 29 streams that were used to constrain the Galactic potential. Columns (4)–(6) list, respectively, the zero-point in R.A. and position of the pole of the coordinate system used to derive the ϕ_1 and ϕ_2 stream coordinates. Columns (7) and (8) report the number of stars found in the structure, and the number with measured radial velocity, respectively. Column (9) reports the stellar mass estimate, computed assuming that each stream sample is complete to $G_0 = 20$ mag, and that its stellar population follows a PARSEC model isochrone of age 12.5 Gyr with the metallicity value given in column (10). Column (11) lists the source of the metallicity information. Some brief comments on the nature of the structure are given in column (12). We note that stream #6 ("Kwando," Grillmair 2017) appears to be the same structure as the "Cetus/Palca" stream (Yuan et al. 2022a). Note also that one star (Gaia ID 3267948604442696448) in stream #8 ("New-2") is a member of group #4 of Dodd et al. (2023), but closer inspection shows that these two structures are different, with stream #8 showing narrow spatial and kinematic coherence.

References. (1) Martin et al. (2022); (2) Martin et al. (2023); (3) Harris (2010); (4) Li et al. (2021); (5) Wan et al. (2020); (6) Grillmair (2017); (7) SDSS; (8) LAMOST; (9) Ji et al. (2020); (10) This work; (11) Roederer & Gnedin (2019); (12) Koposov et al. (2023); (13) Yuan et al. (2020); (14) Caldwell et al. (2020); (15) Gaia BP/RP; (16) Andrae et al. (2023); (17) Li et al. (2019).

were harder to discover simply because they are more diffuse than those found earlier. For instance, streams 8, 17, and 22 are examples of very metal-poor structures ([Fe/H] = –2.07, −2.71, and −2.18, respectively) that subtend a long angle over the sky (62°, 69°, and 80°, respectively) are nearby (≈1.2, ≈1.5, and ≈1.25 kpc distant, respectively) and display a well-defined velocity gradient.

We will discuss the new findings in detail in a future contribution, but here, we nevertheless briefly mention some interesting highlights, either because the new stream is particularly interesting, or because the new data or analysis conveys some new insight into the previously known structure. We will discuss these highlighted streams in order of their s_{ID} index.

9.1. Stream #17 (New-3)

This newly discovered structure has 120 candidate members, including 10 radial velocity measurements and 22 with excellent parallaxes ($\varpi/\delta\varpi > 10$), which are all within 2 kpc of the Sun. A chemical abundance analysis with the `MyGIsFOS` code (Sbordone et al. 2014) of the stars observed at high resolution with the UVES instrument will be presented elsewhere. However, we note here that the two well-measured stars (with Gaia IDs: 3089847099636770560, 3074553030332697344) have [Fe/H] metallicities of −2.75 and −2.67, respectively, which places this system close to the most metal-poor known.

Another surprising property of this stream is its orbit. We use the machinery described in Section 5 to fit the phase-space data, using again only the velocity-confirmed members. The resulting progenitor path is displayed in Figure 18 in relation to the Sun (yellow circle), the Galactic Center, and the positions of the RR Lyrae members of the Sagittarius dwarf galaxy in Gaia DR3, which we have selected using the parameter filter described in Ibata et al. (2020a). It therefore seems highly probable that stream #17 formed in the early universe as a globular cluster satellite of the Sagittarius dwarf, and was brought into the Galaxy with it.

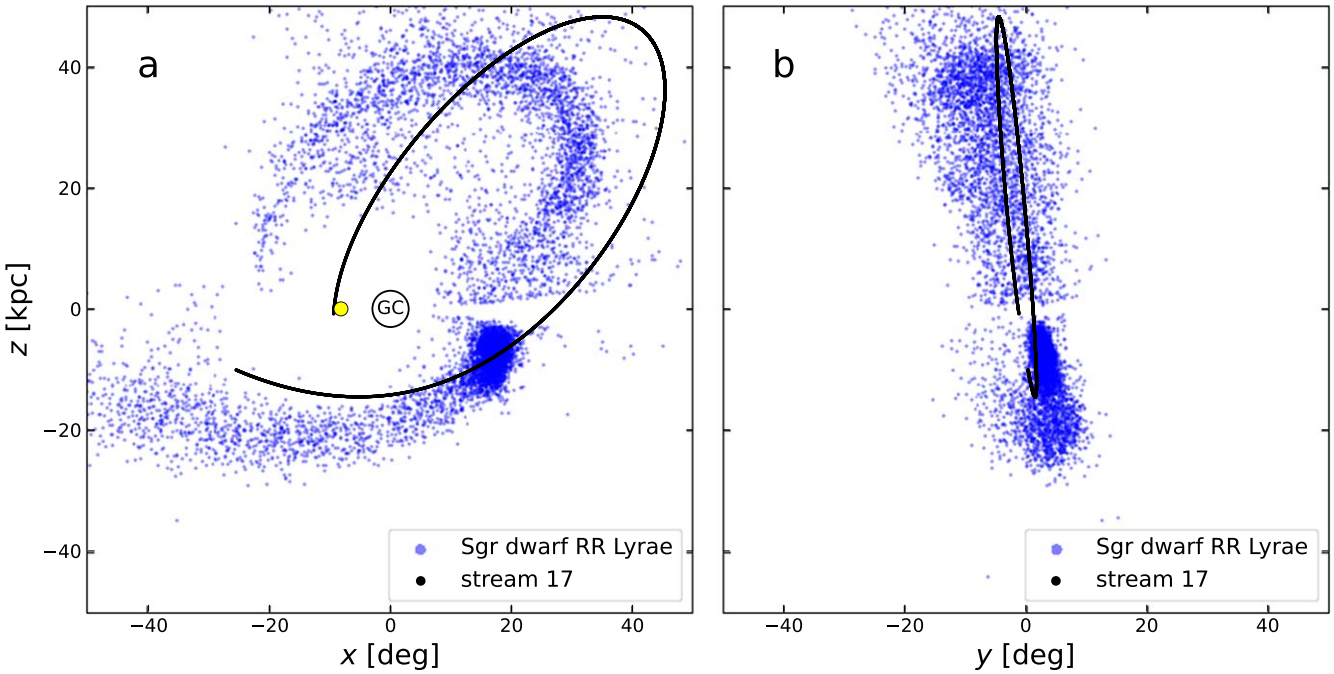

Figure 18. Orbit of stream #17 compared to the present-day structure of the Sagittarius dwarf galaxy, as seen from Gaia DR3 RR Lyrae extracted using the astrometric filter of Ibata et al. (2020a). The orbit is shown integrated backward in time for 1 Gyr, and can be seen to correspond very closely in position to this sample of RR Lyrae stars. The position of the Sun is marked with a yellow dot.

9.2. Fitting Stream #48 (Orphan) with the LMC

The notable missing structure in the sample of 29 long thin streams, which we set aside from our MCMC exploration above, is stream #48 (Orphan-Chenab, Belokurov et al. 2007), which is known to be strongly affected by the LMC (Erkal et al. 2019). We will now attempt to fit this structure using our test-particle algorithm, which was built to handle precisely this sort of situation with the host galaxy and one or several massive perturbers moving under each other's gravitational influence.

Our new contribution to the problem is that we can now impose what we expect is currently the most accurate Milky Way mass model, at least for the spatial region contained by the 29 fitted streams in Figures 16 and 17. Onto our now moving Milky Way model, we add a moving NFW potential to model the LMC.[22] We take the value of the center and the proper motions of the LMC from Gaia Collaboration et al. (2018), we adopt the distance from Pietrzyński et al. (2019), and the radial velocity from van der Marel et al. (2002). We further estimate from Ludlow et al. (2014) that a plausible concentration for the NFW model of the LMC to be $c_{\rm LMC} = 12.5$. Following Koposov et al. (2023), we model the progenitor with a mass of $2.67 \times 10^7\,M_\odot$ and a Plummer scale radius of 1 kpc.

In Figure 19, we show the result of our stream modeling using just the preferred Milky Way model with $\beta_h = 3$ found in Section 8 (green dots), while the maximum-likelihood fit upon adding the LMC has a model mass (defined as M_{200}) of $M_{\rm LMC} = 1.5 \times 10^{11}\,M_\odot$ (black dots). However, these models clearly fail to reproduce the large-scale behavior of the stream faithfully, and are much less convincing than the fits of Koposov et al. (2023). Imposing a mass of $M_{\rm LMC} = 2.85 \times 10^{11}\,M_\odot$ as inferred by Koposov et al. (2023), results in a lower likelihood fit in our Galactic potential model that shows poor agreement with the proper motion measurements. Further work is needed to ascertain whether axisymmetric double-power-law halo models are capable of encapsulating the properties of the Milky Way sufficiently well all the way from the inner to the outer regions of the Galaxy.

[22] To isolate the effect of the Milky Way and the LMC, all other Local Group galaxies are set to zero mass.

9.3. Stream #49 (Gaia-1)

Many of the streams possess stars with high velocity along the line of sight (see Figures 7–9) and many possess high proper motion. It is interesting to consider those stars for which the Gaia parallaxes ϖ are sufficiently good to also identify stars with high total velocity. To this end, we show in Figure 20 the actions (J_r, J_ϕ, Jz) and orbital energy $E_{\rm tot}$ of the objects in our STREAMFINDER sample that have $\varpi/\delta\varpi > 7$ and measured radial velocity. (In this work, we have chosen negative J_ϕ to correspond to prograde rotation.) The outlier in this plane is stream #49 (Gaia-1, Paper I), which thanks to one well-measured Gaia star (ID 3578950965917470208, with $\varpi/\delta\varpi = 9.5$) can be seen to have very high radial action J_r and to have energy that puts it close to being unbound in the (relatively heavy) McMillan (2017) potential. Indeed, this star is actually unbound in the lighter MW2014 potential model (Bovy 2015). At its present radial location of $r = 8.95 \pm 0.36$ kpc, the 1% lower limit to the mass of the Keplerian potential that would bind this star is $0.41 \times 10^{12}\,M_\odot$. We note that the magnitude of the velocity of this star is $816 \pm 82\,{\rm km\,s^{-1}}$, where the uncertainty is almost completely due to parallax uncertainty. The direction of motion of this stream is such that it is just now arriving into the inner Galaxy from the outer halo. So unless this system is an intergalactic traveler, the requirement that it is bound to the Milky Way places a strong lower limit on the total mass of our Galaxy. Furthermore, its metallicity is [Fe/H] = –1.8, which is not extremely metal-poor for a stream, so the possibility that this is

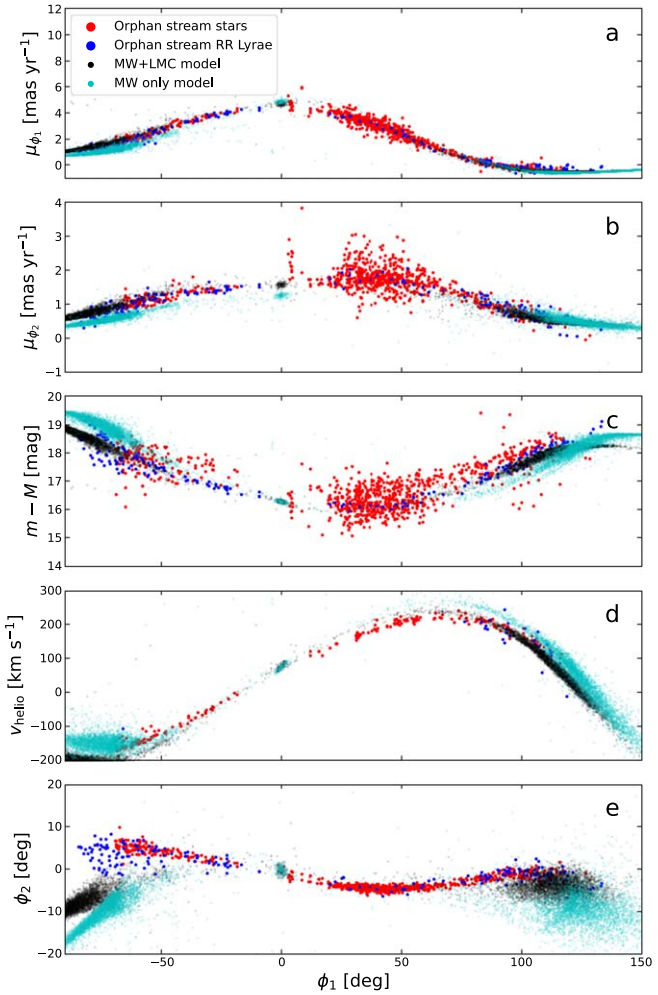

Figure 19. Fit to stream #48 (Orphan-Chenab). Here, the potential includes a moving model for the Milky Way as well as a massive moving LMC, while the stream progenitor loses mass over a period of 5 Gyr. Black dots show the best-fit stream model with both the Milky Way and the LMC, where the latter has a mass of $M_{\rm LMC} = 1.5 \times 10^{11}\,M_\odot$. In contrast, the green dots show the result of setting $M_{\rm LMC} = 0$. The Milky Way host is represented by the model derived previously from orbit fitting (corresponding to the mass model with $\beta_h = 3$ fit in Figure 13).

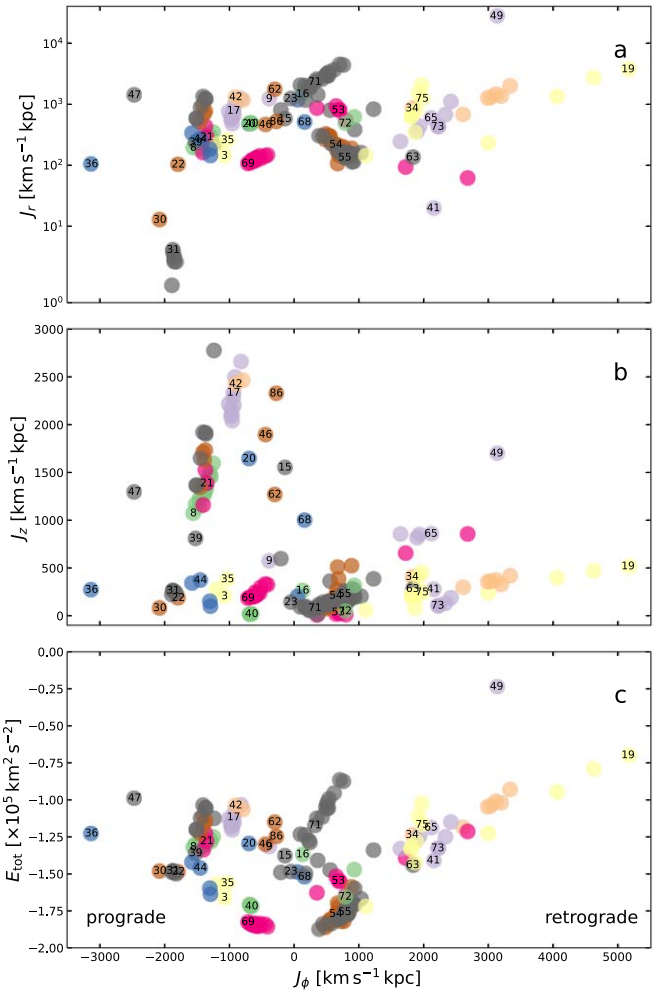

Figure 20. Actions and energy of the 190 stars with measured radial velocities and excellent ($>7\sigma$) astrometric parallaxes, calculated in the McMillan (2017) potential model (for easier comparison to earlier work). Color encodes the stream $s_{\rm ID}$ identification as in Figure 6.

a pristine system being accreted for the first time seems very implausible.

As stream #49 is in the selected sample of *long thin* streams, this object is already taken into account in our MCMC search. However, the constraint that the stars should be bound to the Milky Way was not used. This would be an easy upgrade to add to the algorithm in future work.

In any case, it is interesting that a single star, whose astrometry will be even more accurately measured in future Gaia data releases, can be used to set a lower bound on the Galaxy's mass. The fact that this star is a member of a stream allows us to obtain a clearer view of its origin and possible history of previous interactions.

9.4. Stream #53 (GD-1)

We will briefly revisit the kinematics of stream #53 (GD-1, Grillmair & Dionatos 2006) given the improved data on the system. Our very limited aim here is to motivate the likelihood model that was used as a template in the fitting software detailed above in Sections 5–6.

The mean line-of-sight velocity profile of GD-1 as a function of ϕ_1 was fit previously by Ibata et al. (2020b). The distribution of residuals from that function is shown both as a function of angle ϕ_1 along the stream in Figure 21(a) and as a histogram in Figure 21(b) (where we sum over the full angular range $\phi_1 = [-12.^\circ 8, 102.^\circ 5]$ of the velocity members), and appears to show significant wings. To quantify this possibility, we again used an MCMC procedure to fit the data set with a single Gaussian model, and reran the fit with a two-component Gaussian model, including, of course, the individual velocity measurement uncertainties when computing the likelihoods. The p-value for the measured difference in log-likelihood between the maximum-likelihood fits of the two models is $\approx 1.2 \times 10^{-7}$, indicating that the more complex model with two Gaussians provides a significantly better fit to the data compared to the simpler single Gaussian model.

The two-component fit has means $\mu_1 = 3.2 \pm 0.7$ km s^{-1}, $\mu_2 = 0.8 \pm 3.9$ km s^{-1}, dispersions $\sigma_1 = 7.4 \pm 1.1$ km s^{-1}, $\sigma_2 = 29.1 \pm 6.1$ km s^{-1} and a fraction 0.73 ± 0.09 in component 1. Thus, there is strong evidence that GD-1 has a cocoon-like envelope around it, as suggested by the simulations of

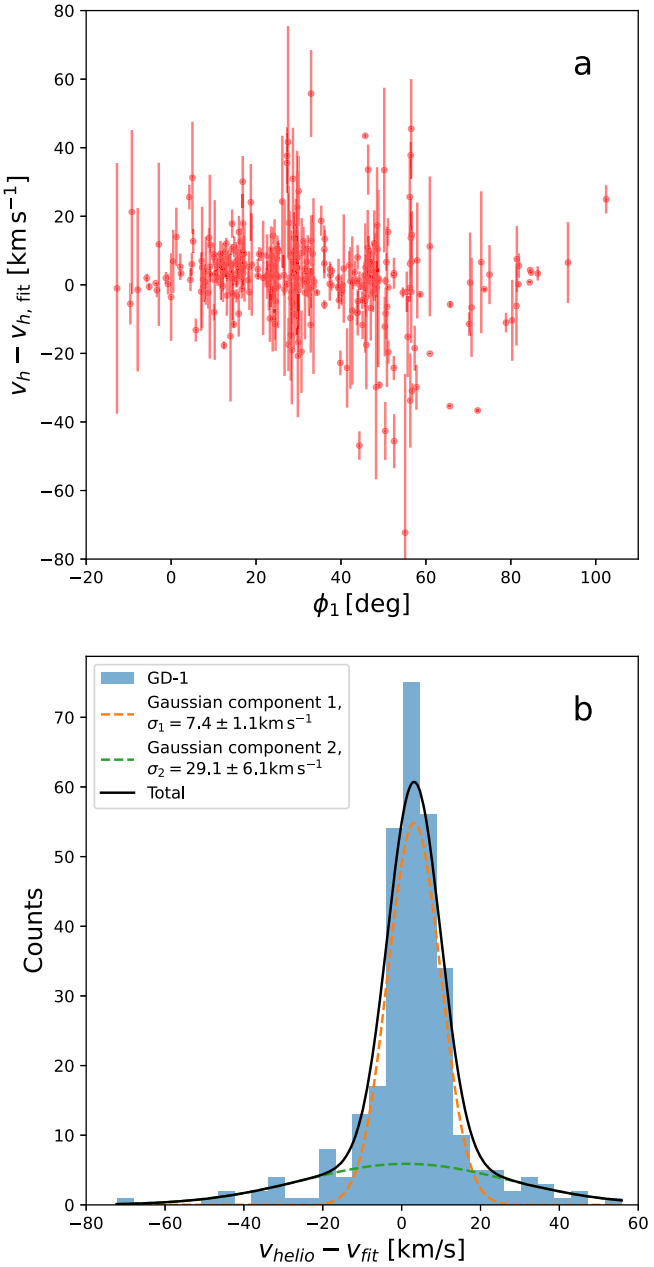

Figure 21. Line-of-sight velocity structure in the GD-1 stream. The velocity residuals from the profile previously fit by Ibata et al. (2020b) are shown (a) as a function of ϕ_1 position angle along the stream, and can be seen to have a wide dispersion. Fitting Gaussians to this distribution (b) strongly suggests the presence of at least two Gaussian components.

Carlberg (2020) and Carlberg & Agler (2023), which posit that stream progenitors were accreted inside dark matter subhalos.

Finally, given the new DR3 data set, and given the center for GD-1 calculated from the midpoint of the mass-weighted stellar population along the stream presented in Section 8, we believe it is useful to consider the counts along the stream as a function of physical path length, as shown in Figure 22. To achieve this coordinate conversion, we use the distance profile derived in Ibata et al. (2020b). The epicyclic spikes with periodicity 2.64 kpc identified in that contribution are very clear in this new representation. While dark matter subhaloes are expected to cause gaps in streams (Carlberg 2012), they are highly unlikely to produce such regular behavior.

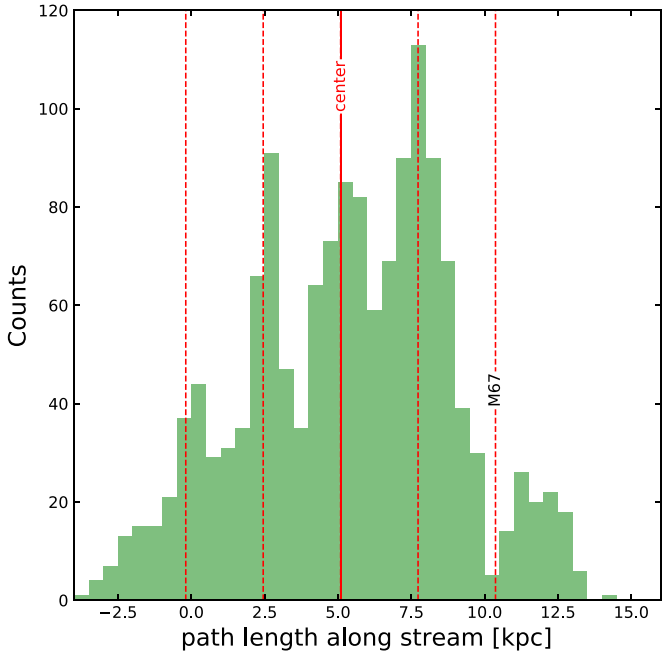

Figure 22. Density as a function of physical path length along the GD-1 stream. The path length zero-point is set to $\phi_1 = 0$. The probable current location of the progenitor is marked, and vertical dashed lines show the periodicity derived by Ibata et al. (2020b). Our data masking at the position of the old open cluster M67 is responsible for the reduced counts at the marked location, which unfortunately coincides with a predicted peak.

9.5. Streams #54 (ω Cen/Fimbulthul) and #55

One of the early successes of our STREAMFINDER program was the discovery of a tidal tail of ωCen (Ibata et al. 2019a), the most massive globular cluster in the Milky Way, and long thought to be the central remnant of an accreted dwarf galaxy (Majewski et al. 2000; Bekki & Freeman 2003). A total of 22 stars of this stream (#54) currently have good parallaxes ($\varpi/\delta\varpi > 7$) and velocities, and consequently appeared in the action and energy diagram displayed in Figure 20 (which we discussed previously in relation to stream #49). Interestingly, a further 18 stars (with the same quality cut) belong to another structure identified by STREAMFINDER (stream #55) that is almost coincident in the action-energy diagram. The mean values and rms scatter of these integrals of motion are (J_r, J_ϕ, J_z) = (207 ± 60, 663 ± 110, 198 ± 120) km s^{-1} kpc and $E_{\rm tot} = -1.78 \pm 0.06 \times 10^5$ km^2 s^{-2} for stream #54 and (J_r, J_ϕ, J_z) = (217 ± 160, 797 ± 190, 200 ± 60) =km s^{-1} kpc and $E_{\rm tot} = -1.73 \pm 0.11 \times 10^5$ km^2 s^{-2} for stream #55. This coincidence strongly suggests a common origin between the two groups.

The association between the two streams is explored further in Figure 23. Panel (a) shows the end result of the *N*-body simulation of ωCen presented by Ibata et al. (2019a). A peculiarity of that model is that it incorporated an initial rotation of the cluster model in order to reproduce the observed present-day rotation of ωCen (Bianchini et al. 2013), which was also found to be necessary to reproduce the peculiar knee-shaped structure of the stream as seen in projection on the sky. In panel (a), particles at a heliocentric distance of $d < 6$ kpc that were still bound to the cluster 1 Gyr ago are displayed in color, with the particles that were no longer bound to the progenitor 0.5 Gyr ago shown in green. The corresponding distribution on the sky is displayed in Galactic coordinates in (b), along with

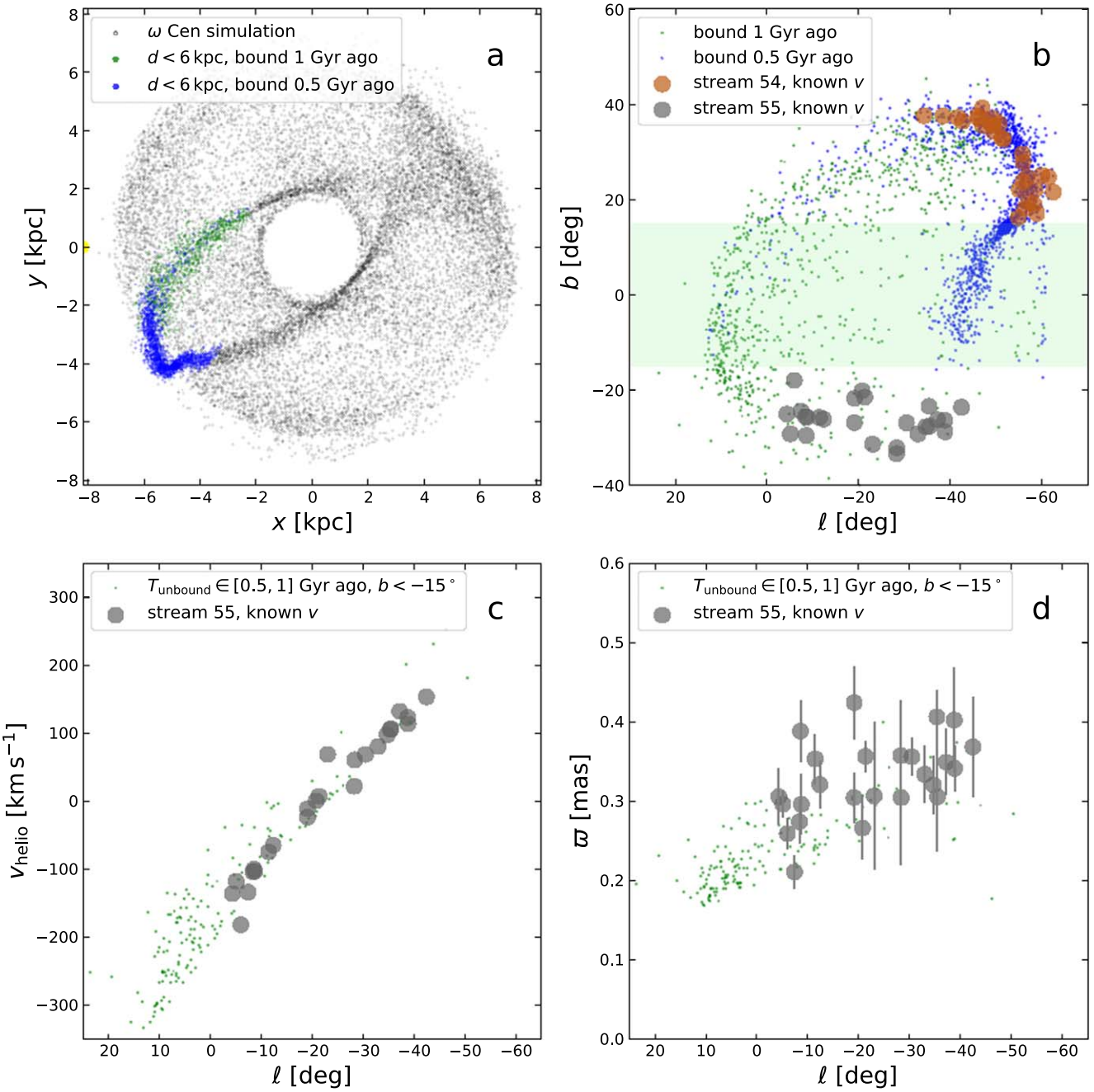

Figure 23. Observations and model of streams #54 and #55. The present-day snapshot of the Ibata et al. (2019a) ω Cen model is shown in the x–y plane (a), oriented such that the location of the Sun lies at $(-R_\odot, 0)$. Particles that were still bound in the simulation 0.5 Gyr ago and currently lie at a heliocentric distance $d < 6$ kpc are colored blue, while those also at $d < 6$ kpc that were bound 1 Gyr ago are colored green. The same colored particles are shown again in panel (b), along with the velocity-confirmed members of stream #54 (brown) and #55 (gray, using the color scheme of Figure 20). The filled green area within 15° of the Galactic plane highlights the region where high source density and extinction render it very challenging to detect streams. The model particles of the older (green) part of the stream that lies below $b = -15°$ are reproduced in panels (c) and (d), which show, respectively, the line-of-sight velocity and parallax behavior of both the data and simulations.

the locations of streams #54 and #55. Although the modeled stream produces a young spatially thin (blue) component, the progenitor is sufficiently massive (with a present-day model mass of $4.2 \times 10^6\, M_\odot$) to scatter particles into an older, broader (green) feature as well. The older part of the stream is also visible in panel (b) in the form of a population of particles below $b = -15°$, approximately coincident on the sky with the location of stream #55. Panels (c) and (d) reproduce again the older (green) model stream selection from panel (b), but further trimmed to show only those particles with $b < -15°$. The line-of-sight velocity (c) and parallax (d) trends of this subsample of the model approximate the corresponding observed properties of stream #55. A similar phase-space structure is present in the simulations of Ferrone et al. (2023).

Hence, this structure, like stream #54 (Fimbulthul), is also trailing tidal arm debris from the disruption of ω Cen. The bulk of the sample is located ≈3 kpc away from the Sun and covers much of the southern bulge region.

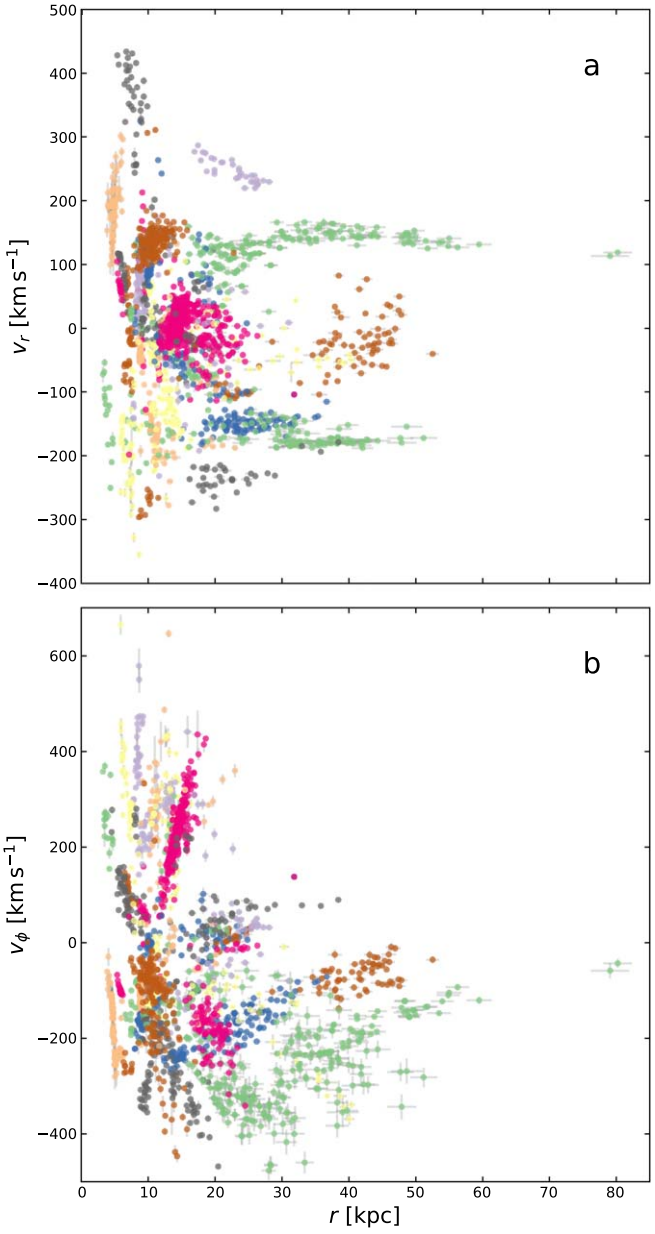

Figure 24. Radial distribution of the stream stars with measured line-of-sight velocity. The radial component (a) and azimuthal component (b) of the velocity vector in a Galactocentric frame are displayed on the ordinate axes. The velocity components are chosen such that positive v_r indicates motion away from the globular cluster, while $v_\phi > 0$ corresponds to retrograde motion with respect to the Galactic disk. Color again encodes the stream $s_{\rm ID}$ identification number, as in Figure 6. The (1σ) error bars are estimated by generating 1000 random realizations of each observed star consistent with the observational uncertainties and projecting into these Galactocentric coordinates.

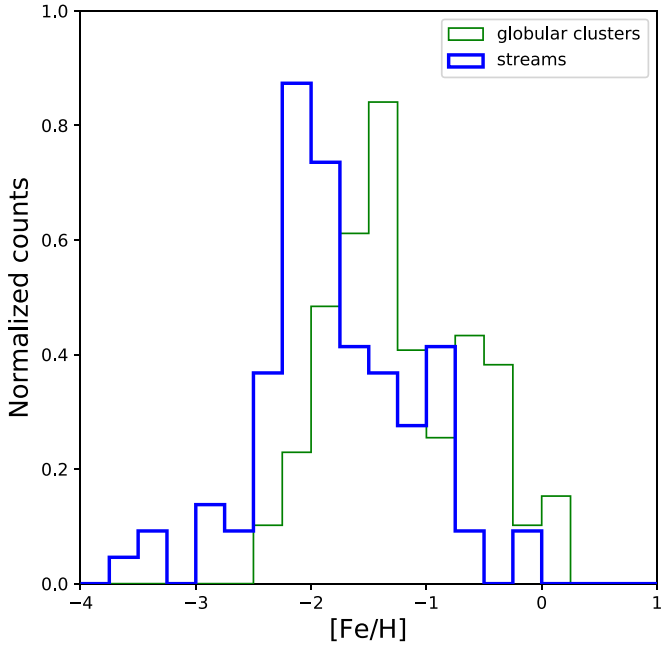

Figure 25. Comparison of the metallicity distribution of the stellar streams detected in Gaia DR3 with STREAMFINDER with the full sample of Galactic globular clusters (Harris 2010).

10. Discussion and Conclusions

10.1. Overview

In this contribution we have presented a large catalog of stellar streams, extracted in a homogeneous manner from the Gaia DR3 data set. We hunted for these structures using an improved version of the STREAMFINDER algorithm (Malhan & Ibata 2018), employing a stream template with a spatial dispersion of 50 pc so as to find structures resulting from the expected dissolution of globular clusters or very small dwarf satellite galaxies. This work is a continuation of our search efforts with the Gaia DR2 (Paper I; Ibata et al. 2019b) and EDR3 (Ibata et al. 2021b; Malhan et al. 2022) catalogs. Despite the radial velocity information being very sparse, the new velocity constraints, along with other enhancements in the algorithm detailed in Section 2, have allowed us to improve stream statistics and detect more subtle, diffuse structures.

We also embarked on a large follow-up campaign of the stream sources with the VLT/UVES high-resolution spectrograph (together with earlier observations in 2018–2020 with CFHT/ESPaDOnS in the Northern Hemisphere). Some low-resolution spectroscopic observations with INT/IDS were also obtained. Combining these data with public spectroscopic surveys has resulted in a catalog containing ≈24,500 thin stream stars, including 2178 line-of-sight velocities (extracted from a total sample of 0.79×10^9 Gaia stars passing the magnitude, extinction, and spatial cuts, of which 24×10^6 also have radial velocity measurements). This represents a significant expansion and refinement over previous catalogs. We expect the data set to be of considerable astrophysical interest for charting the Galactic mass distribution, probing dark substructures, and investigating alternative ideas for the workings of gravity.

The detected streams sample a large volume of the Galaxy, as can be seen in Figure 24, where we display the Galactocentric radius of the stars with measured line-of-sight velocity along with their velocity projections along the radial (v_r) and azimuthal (v_ϕ) directions in a nonrotating Galactocentric frame. A slight majority (48) of the streams in Figure 24(b) have prograde orbits, while 37 display retrograde motion. However, the ratio of the two directions should not be overinterpreted, as significant additional analysis needs to be undertaken to quantify the detection biases introduced by the STREAMFINDER approach. In particular, we expect retrograde streams to be much easier to detect as they will display far greater contrast than prograde streams in proper motion space.

10.2. Metallicity Distribution of Stellar Streams

We collated the metallicities of the detected streams from the literature, from individual metallicity measurements of member stars extracted from public spectroscopic and photometric surveys, and from our own follow-up spectroscopic observations. The resulting values are listed in Table 3, along with the source of the measurements. The Gaia-12 and Hydrus streams appear to be particularly interesting due to their low metallicity in the Martin et al. (2023) metallicity catalog based on Gaia DR3 BP/RP spectro-photometry. Spectroscopic follow-up observations will be useful to confirm the pristine nature of these structures.

Updating the sample previously analyzed in Martin et al. (2022), in Figure 25, we compare the metallicity distribution function (MDF; using the values listed in Table 3) with that of the globular clusters listed in the compilation by Harris (2010). Because of the adopted stream template of Gaussian dispersion 50 pc, we expect the streams presented in this contribution to be mainly the remnants of globular clusters, although we note that the class of small and extremely low-luminosity systems that have recently been discovered (Mau et al. 2020; Cerny et al. 2023; Smith et al. 2024), and which may be very low-mass dwarf galaxies, are also possible progenitor candidates. The peak of the MDF of the streams can be seen to be ≈0.75 dex more metal-poor than that of the surviving clusters.

Cosmological simulations show that, on average, accreted (metal-poor) globular clusters experienced weaker tidal fields compared to in situ (metal-rich) clusters over cosmic time (Renaud et al. 2017). However, that study did not explicitly investigate differences in tidal fields as a function of metallicity for the accreted cluster population itself. If this dependence of tidal history on metallicity in the accreted population is small, the observed difference in the MDF between streams and surviving globular clusters would suggest that metal-poor globular clusters are more susceptible to disruption compared to their metal-rich counterparts. This could be the consequence of metal-poor globular clusters originally being formed with lower masses or densities. Among the surviving globular clusters in the Galactic halo, there appears to be a correlation such that the most metal-rich are also the least massive (Parmentier & Gilmore 2001), which argues against mass being the primary driver, and suggests that density may be more important. Supporting this perspective, Bianchini et al. (2017) propose that metal-rich globular clusters may have formed in a denser initial state, characterized by shorter relaxation times. Their analysis seeks to explain the observed trend in dynamical mass-to-light (M/L) ratios with metallicity: metal-rich globular clusters, at least in M31, exhibit lower M/L ratios compared to their metal-poor counterparts (Strader et al. 2011, although we note that the formation history of M31 is likely to be strikingly different from our own). A denser formation with rapid relaxation times could accelerate the evolution of metal-rich globular clusters toward lower M/L ratios, due to the preferential ejection of low-mass stars and stellar remnants.

Alternatively, the MDF difference may be a manifestation of the fact that the most metal-rich globular clusters in the Galaxy tend to have a higher fraction of disk orbits or orbits confined to the innermost regions of the Galaxy, and are more likely to have been formed in situ. Both types of orbits produce streams that would be harder to detect with `STREAMFINDER`, as the algorithm performs less well for very diffuse streams, streams in very high-density regions, as in the bulge, or streams confined to the disk. Ferrone et al. (2023) have shown that orbits with low apocenters produce streams on the sky that are very different from *classical* streams such as Palomar 5, and thus, they would be harder to detect by hunting along orbits. The differences between the stream and the globular clusters MDF may thus be a selection effect. Quantifying this requires computationally expensive completeness tests, and will be explored in a future contribution.

Clearly, there are multiple factors that could contribute to the observed difference in the metallicity distribution between streams and surviving clusters, including the initial conditions at formation, the strength of the tidal field experienced over time, and the bias of the methodology used to detect the streams. A comprehensive analysis will be needed to disentangle these various factors.

10.3. MCMC Exploration of Streams and Milky Way

Given this unprecedented data set, we decided to also invest substantial effort to build analysis tools that would allow us to build an updated global model of the Milky Way. The computational task is daunting; however, as reasonably realistic axisymmetric Galactic mass models have in excess of 10 parameters, while six parameters are needed to define the orbit of each stream progenitor, and at least a mass and a scale radius is required to define the simplest (Plummer) mass model for each of the latter. The approach we took was to devise two algorithms. The first algorithm is a simpler orbit-fitting analysis, which uses, we believe for the first time, a correction function for each of the observable parameters so as to better approximate stream tracks. The Galactic mass model parameters and the stream kinematics are optimized through an MCMC search. The second algorithm integrates test particles around dissolving progenitors within a dynamic Local Group environment, where the massive host and perturbing galaxies are allowed to move each under the influence of the gravity of the other massive bodies, but with the massless test particles having no effect on other bodies. While the second algorithm is capable of a full MCMC exploration, in the current contribution, we used it primarily to derive the orbit-to-stream corrections needed for the first approach. In future work, we intend to use this algorithm to explore stream and satellite dynamics throughout the Local Group.

10.4. Halo Constraints

The analysis presented in Section 8 started from a simple fit to extant circular velocity and terminal velocity data (together with some additional kinematic constraints) and progressively added in the information from GD-1, which is the best-measured stream, then from streams with known globular clusters, and finally from the selected full sample of 29 long and thin streams. Our hope had been that a model of the complexity of that presented here could be fully constrained by the present data set, with no strong priors needed. However, it transpires that in allowing the halo outer power-law parameter β_h to vary, we obtain solutions to the virial mass that reach up to our imposed limit of $M_{200} < 2 \times 10^{12}\, M_\odot$ (which corresponds to half of the 95% upper limit to the mass of the Local Group, as determined by Peñarrubia et al. 2014). With this constraint, the most likely value of the outer slope parameter is $\beta_h \approx 2.5$. Cosmological simulations of galaxy formation predict that dark matter halos have profiles that have on average an

asymptotic r^{-3} slope in their outer regions (Navarro et al. 1997). Yet there is also an environmental dependence (Avila-Reese et al. 1999), with steeper slopes in galaxy clusters, and shallower slopes ($\beta \approx 2.3$–2.7) in groups and galaxy systems. Thus, the PDF of β_h found in Figure 14 is therefore not unexpected for the case of the Milky Way. Nevertheless, because the MCMC exploration does reach the M_{200} limit when β_h is free, we select the fits with the outer halo power-law parameter fixed to $\beta_h = 3$ as our preferred model.[23]

The fitted value of the halo inner power-law parameter $\gamma_h = 0.97^{+0.17}_{-0.21}$ is fully consistent with the NFW profile, and the scale radius $r_{0,h} = 14.7^{+4.7}_{-1.0}$ kpc is also consistent at $\approx 1\sigma$ with expectations for the Milky Way from ΛCDM based models (Klypin et al. 2002), as is the inferred virial mass of $M_{200} = 1.09^{+0.19}_{-0.14} \times 10^{12}\, M_\odot$. Wilkinson & Evans (1999) introduced the mass interior to 50 kpc as a useful measure of the Galaxy, finding $M_{R<50} = 0.54^{+0.02}_{-0.36} \times 10^{12}\, M_\odot$. Our fitted value of $M_{R<50} = 0.46 \pm 0.03 \times 10^{12}\, M_\odot$ is fully consistent with this, and with the posterior distribution shown by McMillan (2017; their Figure 6). This mass is essentially identical to the value of $M_{R<50} = 0.468^{+0.032}_{-0.034} \times 10^{12}\, M_\odot$ derived by Shen et al. (2022) from an analysis of the kinematics of 168 halo stars in the H3 survey. However, our fits appear to be in tension with the recent detection of a Keplerian decline in the Galactic rotation curve (Jiao et al. 2023), which implies a total Milky Way mass of $0.206^{+0.024}_{-0.013} \times 10^{12}\, M_\odot$; in future work, it will be interesting to explore how the two analyses can be tallied.

We note, however, that our results should not be taken as inconsistent with those of Portail et al. (2017) and Cole & Binney (2017), who found a cored halo with an inner slope shallower than 0.6 in the central 2 kpc, since the present study is not well suited to constrain the mass profile in that region, given the 29 streams considered here. A detailed study of the dark matter distribution in this central region would need a realistic model of the bar (e.g., Portail et al. 2017; Monari et al. 2019).

The local dark matter density, assuming that it is given solely by the density of the halo component, is tightly constrained at $\rho_{h,\odot} = 0.0114 \pm 0.0007\, M_\odot\, \mathrm{pc}^{-3}$. This is consistent at the 2σ level with the best-fit value of $\rho_{h,\odot} = 0.0101\, M_\odot\, \mathrm{pc}^{-3}$ found by McMillan (2017).

The mass flattening of the double-power-law model of the dark matter halo is found to be tightly constrained to $q_{m,h} = 0.749^{+0.026}_{-0.030}$. While this constraint pertains to the global structure of the halo model, the bulk of the stars in the sample that possess line-of-sight velocity measurements resides in the vicinity of the Sun, with half of the sample lying within 13.5 kpc of the Galactic Center, and 90% within 21.6 kpc. Thus, most of the information that constrains our measurement of the density flattening comes from approximately the scale radius of the halo. At similar distances, Koposov et al. (2010) find a *potential* flattening of $q_\Phi = 0.87^{+0.07}_{-0.03}$ from an analysis of the GD-1 stream, while Küpper et al. (2015) derived $q_\Phi = 0.95^{+0.16}_{-0.12}$ from the Palomar 5 stream, which together gives a weighted mean of $q_\Phi = 0.88 \pm 0.05$. For axisymmetric potentials that are close to spherical, the relation between potential and density flattening is $1 - q_\Phi \approx \frac{1}{3}(1 - q_m)$ (Binney & Tremaine 2008), implying $q_m \approx 0.64 \pm 0.15$, which is consistent with our finding at the 1σ level (of course both GD-1 and Palomar 5 are in our sample, and as such our measurement is not fully independent of theirs). At nearer distances close to the Sun, Dodd et al. (2022) have recently suggested that the dark halo has a density flattening of $q_{m,h} = 1.2$, which they deduce from the azimuthal to vertical resonance of stars in the nearby Helmi streams. At larger distances of up to 100 kpc, the stream of the Sagittarius dwarf galaxy provides one of the few constraints on the dark matter halo shape. There was considerable debate whether the data on this stream implied the presence of a spherical (Ibata et al. 2001), an oblate (Johnston et al. 2005), a prolate (Helmi 2004), or a triaxial (Law & Majewski 2010) dark halo. More recently, Vasiliev et al. (2021) studied the evolution of the Sagittarius stream, taking the LMC and the reflex motion of the Milky Way into account, and they suggest a complicated configuration in which the Galactic dark matter is triaxial and changes shape and orientation as a function of radius. This may explain why the earlier studies, which examined different tracers at different distances, drew different conclusions. In future work, it will be interesting to explore whether their halo model improves the fits to the sample of stellar streams considered here.

10.5. Disk Constraints

Our fits put strong constraints on the large-scale mass and structure of the disk components of the Milky Way. The thin disk is found to have a scale length of $h_{R,d} = 2.17^{+0.18}_{-0.08}$ kpc and scale height of $h_{z,d} = 0.347^{+0.007}_{-0.010}$ kpc, while the same properties of the thick disk are, respectively, $h_{R,t} = 1.62^{+0.72}_{-0.13}$ kpc and $h_{z,t} = 0.86^{+0.03}_{-0.02}$ kpc. The combined mass of the two stellar disks is $M_{d+t} = 4.20^{+0.44}_{-0.53} \times 10^{10}\, M_\odot$, of which $9.5^{+14.3}_{-1.4}$% resides in the thick disk. In terms of the surface density at the Solar radius, we find that the local thick disk constitutes $12.4\% \pm 0.7\%$ of the combined disk surface density, while the local thick disk density fraction is $5.4\% \pm 0.4\%$. The disk structural parameters we measure are contained within the range reported in the literature review and meta-analysis by Bland-Hawthorn & Gerhard (2016). To help visualize the behavior of our best-fit model, we show its rotation curve in Figure 26.

As a sanity check of (primarily) the stellar disk components of our model, we compare in Figure 27 the profile of the $K_{z,1.1}$ vertical acceleration at a position of $z = 1.1$ kpc above the Galactic plane to the values of this parameter derived from the analysis of Bovy & Rix (2013). We did not use their data set in our model fitting because the uncertainties on their data points are correlated, yet one can see that the model follows the $K_{z,1.1}$ trend reasonably well. Like the McMillan (2017) model, ours slightly underpredicts the Bovy & Rix (2013) $K_{z,1.1}$ data at small radii, but our model follows the profile closely at $R \gtrsim 6.5$ kpc.

Our model is fitted primarily to dynamical constraints, and so the properties of the disk models we find should reflect a decomposition of their mass distribution given the imposed double-exponential analytic form. In contrast, when the thick disk is defined using chemical abundances, the resulting thin and thick disk masses have been found to be very similar (Snaith et al. 2014). This difference may be the result of using mass models that are too simple for these components in the

[23] Obviously, we could have incorporated the results of the Peñarrubia et al. (2014) analysis into our MCMC search as a Bayesian prior, but we deem that the present approach presents a clearer view of the constraints provided by the STREAMFINDER data set.

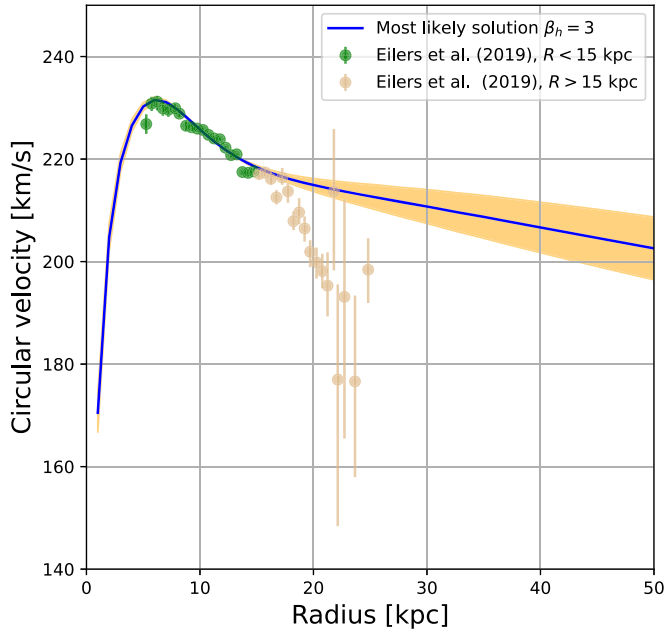

Figure 26. Circular velocity of the most likely Galaxy model with $\beta_h = 3$ (purple line). The shaded (yellow) region shows the 1σ spread derived from the models explored in the MCMC chain. We show for comparison the Eilers et al. (2019) data set; the selected subset at $R < 15$ kpc where the effects of the Galactic warp and flaring are less likely to be problematic is highlighted in green.

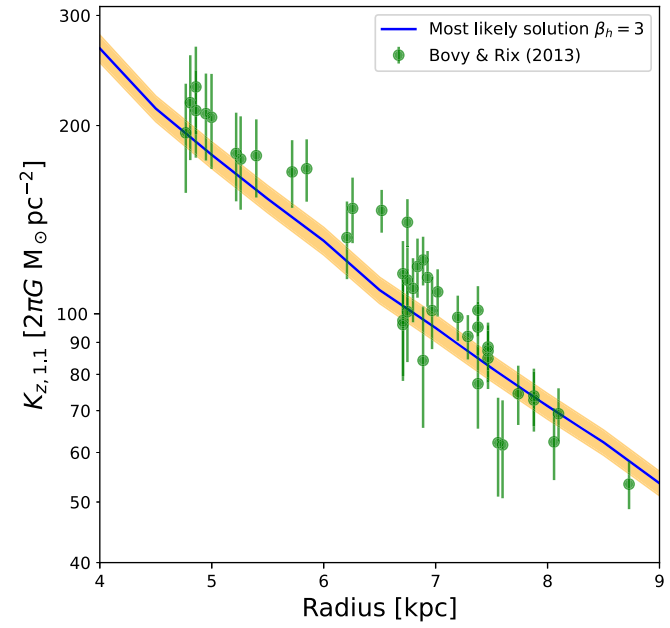

Figure 27. Profile of the $K_{z,1.1}$ vertical acceleration $z = 1.1$ kpc above the Galactic plane. The best Milky Way model (purple) together with its (1σ) uncertainties derived from the MCMC chain are compared to the analysis of Bovy & Rix (2013). Note that these data were not used to derive the mass model.

dynamical analysis; broken exponentials may be more appropriate (Lian et al. 2022).

10.6. M/L Ratio

It is interesting to consider the M/L ratio of the luminous components of the Galaxy, given that our model is fit to dynamical constraints and *relative* star counts. The extinction-corrected K-band absolute magnitude was measured from COBE data (Drimmel & Spergel 2001) to be $M_K = -24.02$, and Hammer et al. (2007) estimate a 0.1 mag uncertainty on this value from a comparison to earlier measurements. Adopting $M_{K\odot} = 3.3$ (Bell et al. 2003), we find a K-band M/L ratio of the stellar components of the Milky Way of $M_{\star,\mathrm{MW}}/L = 0.61 \pm 0.08\, M_\odot/L_\odot$, which is substantially lower than the K-band $M/L = 0.95 \pm 0.03\, M_\odot/L_\odot$ derived by Bell et al. (2003) from a stellar populations analysis of Two Micron All Sky Survey (2MASS) and SDSS galaxies. However, those authors use a universal initial mass function (IMF) tailored to produce maximum-disk solutions, and they comment that values ≈30% lower are obtained with a Kroupa et al. (1993) IMF. Hence, with plausible assumptions about the IMF, our Milky Way stellar mass estimate based on stream dynamics is fully consistent with the stellar mass based on stellar evolution models and the integrated luminosity of the Milky Way.

10.7. Toward a Nonparametric Model of the Galaxy

The very tight constraints we have derived on the local dark matter and on the structure of the Galactic components are clearly, in part, an artifact of the rigidity of the analytic functions (Equations (8) and (9)) used to describe them. In future work, we hope to overcome this limitation; indeed, our motivation in developing the orbit-to-stream correction functions $\Delta_\Theta(\phi_1)$ was to be able to reuse them to derive a nonparametric Galactic model using the machinery developed in Ibata et al. (2021a). That method uses an unsupervised machine learning procedure to derive the transformation from positions and velocities along orbits to canonical actions and angles, and thereby effectively builds a data-driven Hamiltonian of the Galaxy.

10.8. Highlighted Streams

While a detailed exposition of the properties of the new streams is beyond the scope of the present paper, and will be presented in a future contribution, in Section 9, we nevertheless briefly discussed some highlights and insights from the new catalog.

1. Stream #17 is a very metal-poor stream, with a metallicity of [Fe/H] = –2.7 that is below the expected floor for cluster formation (Beasley et al. 2019). It is currently passing through the solar neighborhood, yet it appears to have been a satellite of the Sagittarius dwarf galaxy. It will be fascinating to model the dynamics of this system further to ascertain when and under what conditions its backward path can be made to coincide precisely with that of the Sagittarius dwarf. We suspect that this will require the perturbing effect of the LMC to also be taken into account, for which the stream-fitting machinery presented in Section 6, with its capability of implementing the forces due to several perturbers at once, should be ideal. The extreme proximity of this extragalactic system may also be useful for stellar population and chemical analyses.
2. For stream #48 (Orphan-Chenab), we briefly investigate with our dynamical stream-fitting software whether our newly fitted Milky Way mass model affects the conclusion that a massive LMC is needed to reproduce the observed phase-space structure of this stream. While

the best-fit solution has $M_{\rm LMC} = 1.5 \times 10^{11}\,M_{\odot}$ (consistent with Erkal et al. 2019), we find that our models do not yet give a satisfactory representation of the stream's large-scale morphology, which we suspect is due to an insufficient flexibility of the adopted Milky Way halo density model.

3. Stream #49 is remarkable due to its very large radial action: it is presently arriving from the outer halo and so its high-velocity members place useful constraints on the total mass of the Galaxy. Indeed, the astrometry of one of its bright member stars was very well measured by Gaia (ID 3578950965917470208), and the derived total energy of this star is in tension with the popular MW2014 Galactic potential model (Bovy 2015), unless the system is not bound to the Milky Way, which seems highly unlikely.
4. We revisit stream #53 (GD-1), and show that the line-of-sight velocity distribution is best modeled as a combination of two components, a kinematically cold part with dispersion $7.4 \pm 1.1\,{\rm km\,s^{-1}}$ and a hot component with dispersion $29.1 \pm 6.1\,{\rm km\,s^{-1}}$. Such kinematic structure is consistent with simulations where globular clusters form at random locations within dark matter subhalos and are subsequently accreted onto large galaxies (Carlberg 2020; Carlberg & Agler 2023). We also used the updated catalog to clearly demonstrate the periodicity of the spikes in the number counts along this stream when viewed as a function of physical distance along the structure: such periodicity is highly unlikely to be due to random encounters with dark matter subhalos.
5. Finally, we argue that stream #55 is a tidal feature of ω Cen, the most massive of the Milky Way's globular clusters, and is a broader and significantly closer counterpart to the previously discovered stream #54 (Fimbulthul). This trailing arm structure skirts the southern bulge at a heliocentric distance of $\approx$3 kpc. It appears to be constituted of stars that were lost to ω Cen between 0.5 and 1 Gyr ago, whereas the stream #54 stars were lost more recently than 0.5 Gyr ago. We suspect that the observed relative densities of streams #54 and #55 could be used in future work to refine the disruption model and so better understand the dynamical history of this unique and important cluster.

10.9. Limitations

While we have tried to render the analysis as realistic as possible, there are several limitations to our approach. First of all, our Milky Way model is axisymmetric, which is clearly unrealistic, especially in the inner Galaxy where dynamics are dominated by the bar. Indeed, some of the streams we removed from the sample were rejected precisely because we feared that their small pericenters made them highly susceptible to the bar, and hence, that they would be poorly reproduced with our axisymmetric model. The recent work of Thomas et al. (2023) shows that it is now possible to overcome such limitations, and following their lead, we hope to be able to include non-axisymmetric components in our MCMC exploration in the near future. Similarly, it may be useful to include spiral arms in the modeling, though we suspect their influence will be relatively minor for the halo streams we have considered.

Using a double-power-law mass model with a single shape parameter may also be too limiting, as hinted by the analysis in Section 9.2. It may be necessary to consider a basis function approach (e.g., Petersen et al. 2022) to model the mass distribution in a more realistic manner.

In our future work, we intend to use the algorithms developed here to explore the combined effect of the LMC, the Sagittarius dwarf, and other potential perturbers on the full population of stellar streams.

10.10. Concluding Remarks

The upcoming huge WEAVE and 4MOST spectroscopic campaigns that will soon be launched promise an exciting future for this field of study. The present work was based on a relatively small number of velocity-confirmed stream members, and our statistics could easily be improved by an order of magnitude with observations from those spectroscopic surveys. Furthermore, the next Gaia DR4 release will substantially improve the proper motion and parallax accuracy, most probably allowing yet more systems to be detected with our algorithm and tightening the constraints on the known structures.

However, the most exciting use of this data now is to use it to try to shed light on the dark matter, and ascertain whether the observed stream morphology, structure, substructure, and dynamics allow us to prefer one dark matter model over others.

Acknowledgments

R.I., N.M., D.A., B.F., G.M., R.E., and A.S. acknowledge funding from the Agence Nationale de la Recherche (ANR project ANR-18-CE31-0006, ANR-18-CE31-0017, and ANR-19-CE31-0017), from CNRS/INSU through the Program National Galaxies et Cosmologie, and from the European Research Council (ERC) under the European Unions Horizon 2020 research and innovation program (grant agreement No. 834148). F.R. acknowledges support provided by the University of Strasbourg Institute for Advanced Study (USIAS), within the French national program Investment for the Future (Excellence Initiative) IdEx-Unistra. M.B. acknowledges the financial support to this research by INAF, through the Mini Grant assigned to the project "Chemo-dynamics of the Accreted Halo of the Milky Way (CHAM)" (PI: M. Bellazzini), and by the Italian Ministero dell'Universitä e della Ricerca through the PRIN 2022 Grant 2022LLP8TK_001 "LEGO—Reconstructing the building blocks of the Galaxy by chemical tagging" (PI: A. Mucciarelli). G.T. acknowledges support from Agencia Estatal de Investigación del Ministerio de Ciencia en Innovación (AEI-MICIN) under grant No. PID2020-118778GB-I00/10.13039/501100011033, the MICIN under grant No. FJC2018-037323-I, and the AEI under grant No. CEX2019-000920-S. A.A.A. acknowledges support from the Herchel Smith Fellowship at the University of Cambridge and a Fitzwilliam College research fellowship supported by the Isaac Newton Trust. E.S. acknowledges funding through the VIDI grant "Pushing Galactic Archeology to its limits" (with project number VI.Vidi.193.093), which is funded by the Dutch Research Council (NWO). This research has been partially funded by a Spinoza award by NWO (SPI 78–411). This research was supported by the International Space Science Institute (ISSI) in Bern, through ISSI International Team project 540 (The Early Milky Way).

We gratefully acknowledge the High Performance Computing Center of the Université de Strasbourg for the very generous time allocation and for its support of the development of this project.

We wish to thank Pablo Galán, Rosa Hoogenboom, Sara Vitali, Clár-Bríd Tohill, Sara Vitali, and Paige Yarker for their invaluable help in supporting the INT observations reported here.

This work has made use of data from the European Space Agency (ESA) mission Gaia,[24] processed by the Gaia Data Processing and Analysis Consortium (DPAC).[25] Funding for the DPAC has been provided by national institutions, in particular, the institutions participating in the Gaia Multilateral Agreement.

This work is based on observations collected at the European Southern Observatory under ESO programs 105.20AL.001, 110.246A.001, and 111.2517.001.

Funding for SDSS-III[26] has been provided by the Alfred P. Sloan Foundation, the Participating Institutions, the National Science Foundation, and the US Department of Energy Office of Science.

SDSS-III is managed by the Astrophysical Research Consortium for the Participating Institutions of the SDSS-III Collaboration including the University of Arizona, the Brazilian Participation Group, Brookhaven National Laboratory, Carnegie Mellon University, University of Florida, the French Participation Group, the German Participation Group, Harvard University, the Instituto de Astrofisica de Canarias, the Michigan State/Notre Dame/JINA Participation Group, Johns Hopkins University, Lawrence Berkeley National Laboratory, Max Planck Institute for Astrophysics, Max Planck Institute for Extraterrestrial Physics, New Mexico State University, New York University, Ohio State University, Pennsylvania State University, University of Portsmouth, Princeton University, the Spanish Participation Group, University of Tokyo, University of Utah, Vanderbilt University, University of Virginia, University of Washington, and Yale University.

Guoshoujing Telescope (the Large Sky Area Multi-Object Fiber Spectroscopic Telescope (LAMOST)) is a major national scientific project built by the Chinese Academy of Sciences. Funding for the project has been provided by the National Development and Reform Commission. LAMOST is operated and managed by the National Astronomical Observatories, Chinese Academy of Sciences.

Software: Python `corner` (Foreman-Mackey 2016), `STREAMFINDER` (Malhan & Ibata 2018), `Armadillo` (Sanderson & Curtin 2016), `IRAF` (Tody 1986, 1993), `GalPot` (Dehnen & Binney 1998).

Data Availability

The sample of stream stars will be available online at the VizieR service.[27]

ORCID iDs

Rodrigo Ibata https://orcid.org/0000-0002-3292-9709
Khyati Malhan https://orcid.org/0000-0002-8318-433X
Wassim Tenachi https://orcid.org/0000-0001-8392-3836
Anke Ardern-Arentsen https://orcid.org/0000-0002-0544-2217
Michele Bellazzini https://orcid.org/0000-0001-8200-810X
Paolo Bianchini https://orcid.org/0000-0002-0358-4502
Piercarlo Bonifacio https://orcid.org/0000-0002-1014-0635
Elisabetta Caffau https://orcid.org/0000-0001-6011-6134
Benoit Famaey https://orcid.org/0000-0003-3180-9825
Salvatore Ferrone https://orcid.org/0000-0003-1623-6643
Nicolas F. Martin https://orcid.org/0000-0002-1349-202X
Florent Renaud https://orcid.org/0000-0001-5073-2267
Guillaume Thomas https://orcid.org/0000-0002-2468-5521
Zhen Yuan https://orcid.org/0000-0002-8129-5415

[24] https://www.cosmos.esa.int/gaia
[25] https://www.cosmos.esa.int/web/gaia/dpac/consortium
[26] http://www.sdss3.org/
[27] https://vizier.unistra.fr

References

Andrae, R., Rix, H.-W., & Chandra, V. 2023, ApJS, 267, 8
Avila-Reese, V., Firmani, C., Klypin, A., & Kravtsov, A. V. 1999, MNRAS, 310, 527
Baumgardt, H., & Hilker, M. 2018, MNRAS, 478, 1520
Baumgardt, H., & Vasiliev, E. 2021, MNRAS, 505, 5957
Beasley, M. A., Leaman, R., Gallart, C., et al. 2019, MNRAS, 487, 1986
Bekki, K., & Freeman, K. C. 2003, MNRAS, 346, L11
Bell, E. F., McIntosh, D. H., Katz, N., & Weinberg, M. D. 2003, ApJS, 149, 289
Belokurov, V., Evans, N. W., Irwin, M. J., et al. 2007, ApJ, 658, 337
Bianchini, P., Sills, A., van de Ven, G., & Sippel, A. C. 2017, MNRAS, 469, 4359
Bianchini, P., Varri, A. L., Bertin, G., & Zocchi, A. 2013, ApJ, 772, 67
Binney, J., & Tremaine, S. 2008, Galactic Dynamics (2nd ed.; Princeton, NJ: Princeton Univ. Press)
Bland-Hawthorn, J., & Gerhard, O. 2016, ARA&A, 54, 529
Bovy, J. 2015, ApJS, 216, 29
Bovy, J., & Rix, H.-W. 2013, ApJ, 779, 115
Bressan, A., Marigo, P., Girardi, L., et al. 2012, MNRAS, 427, 127
Buder, S., Asplund, M., Duong, L., et al. 2018, MNRAS, 478, 4513
Caldwell, N., Bonaca, A., Price-Whelan, A. M., Sesar, B., & Walker, M. G. 2020, AJ, 159, 287
Carlberg, R. G. 2012, ApJ, 748, 20
Carlberg, R. G. 2020, ApJ, 889, 107
Carlberg, R. G., & Agler, H. 2023, ApJ, 953, 99
Cerny, W., Martínez-Vázquez, C. E., Drlica-Wagner, A., et al. 2023, ApJ, 953, 1
Clementini, G., Ripepi, V., Garofalo, A., et al. 2023, A&A, 674, A18
Cole, D. R., & Binney, J. 2017, MNRAS, 465, 798
Combes, F., Leon, S., & Meylan, G. 1999, A&A, 352, 149
Correa Magnus, L., & Vasiliev, E. 2022, MNRAS, 511, 2610
Cui, X.-Q., Zhao, Y.-H., Chu, Y.-Q., et al. 2012, RAA, 12, 1197
Dehnen, W. 2002, JCoPh, 179, 27
Dehnen, W., & Binney, J. 1998, MNRAS, 294, 429
Dodd, E., Callingham, T. M., Helmi, A., et al. 2023, A&A, 670, L2
Dodd, E., Helmi, A., & Koppelman, H. H. 2022, A&A, 659, A61
D'Odorico, S., Cristiani, S., Dekker, H., et al. 2000, Proc. SPIE, 4005, 121
Drimmel, R., & Spergel, D. N. 2001, ApJ, 556, 181
Eilers, A.-C., Hogg, D. W., Rix, H.-W., & Ness, M. K. 2019, ApJ, 871, 120
Erkal, D., Belokurov, V., Laporte, C. F. P., et al. 2019, MNRAS, 487, 2685
Errani, R., & Navarro, J. F. 2021, MNRAS, 505, 18
Errani, R., Navarro, J. F., Smith, S. E. T., & McConnachie, A. W. 2024, ApJ, 965, 20
Ferrone, S., Di Matteo, P., Mastrobuono-Battisti, A., et al. 2023, A&A, 673, A44
Foreman-Mackey, D. 2016, JOSS, 1, 24
Fukushige, T., & Heggie, D. C. 2000, MNRAS, 318, 753
Gaia Collaboration, Helmi, A., van Leeuwen, F., et al. 2018, A&A, 616, A12
Gaia Collaboration, Prusti, T., de Bruijne, J. H. J., et al. 2016, A&A, 595, A1
Gaia Collaboration, Vallenari, A., Brown, A. G. A., et al. 2023, A&A, 674, A1
Goodman, J., & Weare, J. 2010, CAMCS, 5, 65
GRAVITY Collaboration, Abuter, R., Amorim, A., et al. 2019, A&A, 625, L10
Grillmair, C. J. 2017, ApJ, 847, 119
Grillmair, C. J., & Dionatos, O. 2006, ApJL, 643, L17
Hammer, F., Puech, M., Chemin, L., Flores, H., & Lehnert, M. D. 2007, ApJ, 662, 322
Harris, W. E. 2010, arXiv:1012.3224
Helmi, A. 2004, ApJL, 610, L97

Ibata, R., Bellazzini, M., Thomas, G., et al. 2020a, ApJL, 891, L19
Ibata, R., Diakogiannis, F. I., Famaey, B., & Monari, G. 2021a, ApJ, 915, 5
Ibata, R., Lewis, G. F., Irwin, M., Totten, E., & Quinn, T. 2001, ApJ, 551, 294
Ibata, R., Malhan, K., Martin, N., et al. 2021b, ApJ, 914, 123
Ibata, R., Sollima, A., Nipoti, C., et al. 2011, ApJ, 738, 186
Ibata, R., Thomas, G., Famaey, B., et al. 2020b, ApJ, 891, 161
Ibata, R. A., Bellazzini, M., Malhan, K., Martin, N., & Bianchini, P. 2019a, NatAs, 3, 667
Ibata, R. A., Lewis, G. F., Thomas, G., Martin, N. F., & Chapman, S. 2017a, ApJ, 842, 120
Ibata, R. A., Malhan, K., Martin, N. F., & Starkenburg, E. 2018, ApJ, 865, 85
Ibata, R. A., Malhan, K., & Martin, N. F. 2019b, ApJ, 872, 152
Ibata, R. A., McConnachie, A., Cuillandre, J.-C., et al. 2017b, ApJ, 848, 129
Ji, A. P., Li, T. S., Hansen, T. T., et al. 2020, AJ, 160, 181
Jiao, Y., Hammer, F., Wang, H., et al. 2023, A&A, 678, A208
Johnston, K. V., Law, D. R., & Majewski, S. R. 2005, ApJ, 619, 800
Jurić, M., Ivezić, Ž., Brooks, A., et al. 2008, ApJ, 673, 864
Klypin, A., Zhao, H., & Somerville, R. S. 2002, ApJ, 573, 597
Koposov, S. E., Belokurov, V., Li, T. S., et al. 2019, MNRAS, 485, 4726
Koposov, S. E., Erkal, D., Li, T. S., et al. 2023, MNRAS, 521, 4936
Koposov, S. E., Rix, H.-W., & Hogg, D. W. 2010, ApJ, 712, 260
Koposov, S. E., Walker, M. G., Belokurov, V., et al. 2018, MNRAS, 479, 5343
Kroupa, P., Tout, C. A., & Gilmore, G. 1993, MNRAS, 262, 545
Kuijken, K., & Gilmore, G. 1991, ApJL, 367, L9
Kunder, A., Kordopatis, G., Steinmetz, M., et al. 2017, AJ, 153, 75
Küpper, A. H. W., Balbinot, E., Bonaca, A., et al. 2015, ApJ, 803, 80
Küpper, A. H. W., Macleod, A., & Heggie, D. C. 2008, AN, 329, 1061
Law, D. R., & Majewski, S. R. 2010, ApJ, 714, 229
Li, G.-W., Yanny, B., & Wu, Y. 2018, ApJ, 869, 122
Li, T. S., Koposov, S. E., Erkal, D., et al. 2021, ApJ, 911, 149
Li, T. S., Koposov, S. E., Zucker, D. B., et al. 2019, MNRAS, 490, 3508
Li, T. S., Simon, J. D., Kuehn, K., et al. 2018, ApJ, 866, 22
Lian, J., Zasowski, G., Mackereth, T., et al. 2022, MNRAS, 513, 4130
Ludlow, A. D., Navarro, J. F., Angulo, R. E., et al. 2014, MNRAS, 441, 378
Majewski, S. R., Patterson, R. J., Dinescu, D. I., et al. 2000, in Proc. of the Liege Int. Astrophysics Coll. 35, The Galactic Halo: From Globular Cluster to Field Stars, ed. A. Noels et al. (Belgium: Institut d'Astrophysique et de Geophysique), 619
Majewski, S. R., Schiavon, R. P., Frinchaboy, P. M., et al. 2017, AJ, 154, 94
Malhan, K., & Ibata, R. A. 2018, MNRAS, 477, 4063
Malhan, K., Ibata, R. A., & Martin, N. F. 2018, MNRAS, 481, 3442
Malhan, K., Ibata, R. A., Sharma, S., et al. 2022, ApJ, 926, 107
Martin, N. F., Ibata, R. A., Starkenburg, E., et al. 2022, MNRAS, 516, 5331
Martin, N. F., Starkenburg, E., Yuan, Z., et al. 2023, arXiv:2308.01344
Mastrobuono-Battisti, A., Di Matteo, P., Montuori, M., & Haywood, M. 2012, A&A, 546, L7
Mateu, C. 2023, MNRAS, 520, 5225
Mau, S., Cerny, W., Pace, A. B., et al. 2020, ApJ, 890, 136
McClure-Griffiths, N. M., & Dickey, J. M. 2007, ApJ, 671, 427
McClure-Griffiths, N. M., & Dickey, J. M. 2016, ApJ, 831, 124
McMillan, P. J. 2017, MNRAS, 465, 76
Momany, Y., Zaggia, S., Gilmore, G., et al. 2006, A&A, 451, 515
Monari, G., Famaey, B., Siebert, A., Wegg, C., & Gerhard, O. 2019, A&A, 626, A41
Muraveva, T., Delgado, H. E., Clementini, G., Sarro, L. M., & Garofalo, A. 2018, MNRAS, 481, 1195
Navarro, J. F., Frenk, C. S., & White, S. D. M. 1997, ApJ, 490, 493
Odenkirchen, M., Grebel, E. K., Kayser, A., Rix, H.-W., & Dehnen, W. 2009, AJ, 137, 3378
Parmentier, G., & Gilmore, G. 2001, A&A, 378, 97
Peñarrubia, J., Ma, Y.-Z., Walker, M. G., & McConnachie, A. 2014, MNRAS, 443, 2204
Petersen, M. S., Peñarrubia, J., & Jones, E. 2022, MNRAS, 514, 1266
Pietrzyński, G., Graczyk, D., Gallenne, A., et al. 2019, Natur, 567, 200
Portail, M., Gerhard, O., Wegg, C., & Ness, M. 2017, MNRAS, 465, 1621
Press, W. H., Teukolsky, S. A., Vetterling, W. T., & Flannery, B. P. 1992, Numerical Recipes in FORTRAN. The Art of Scientific Computing (Cambridge: Cambridge Univ. Press)
Randich, S., Gilmore, G., Magrini, L., et al. 2022, A&A, 666, A121
Renaud, F., Agertz, O., & Gieles, M. 2017, MNRAS, 465, 3622
Roederer, I. U., & Gnedin, O. Y. 2019, ApJ, 883, 84
Sanderson, C., & Curtin, R. 2016, JOSS, 1, 26
Sbordone, L., Caffau, E., Bonifacio, P., & Duffau, S. 2014, A&A, 564, A109
Schlafly, E. F., & Finkbeiner, D. P. 2011, ApJ, 737, 103
Schlegel, D. J., Finkbeiner, D. P., & Davis, M. 1998, ApJ, 500, 525
Schönrich, R., Binney, J., & Dehnen, W. 2010, MNRAS, 403, 1829
Shen, J., Eadie, G. M., Murray, N., et al. 2022, ApJ, 925, 1
Simon, J. D., Li, T. S., Erkal, D., et al. 2020, ApJ, 892, 137
Sivia, D., & Skilling, J. 2006, Data Analysis: A Bayesian Tutorial, Oxford Science Publications (Oxford: Oxford Univ. Press),
Smith, S. E. T., Cerny, W., Hayes, C. R., et al. 2024, ApJ, 961, 92
Snaith, O. N., Haywood, M., Di Matteo, P., et al. 2014, ApJL, 781, L31
Starkenburg, E., Martin, N., Youakim, K., et al. 2017, MNRAS, 471, 2587
Strader, J., Caldwell, N., & Seth, A. C. 2011, AJ, 142, 8
Thomas, G. F., Famaey, B., Monari, G., et al. 2023, A&A, 678, A180
Tody, D. 1986, Proc. SPIE, 627, 733
Tody, D. 1993, in ASP Conf. Ser. 52, Astronomical Data Analysis Software and Systems II, ed. R. J. Hanisch, R. J. V. Brissenden, & J. Barnes (San Francisco, CA: ASP), 173
van der Marel, R. P., Alves, D. R., Hardy, E., & Suntzeff, N. B. 2002, AJ, 124, 2639
Vasiliev, E. 2019, MNRAS, 484, 2832
Vasiliev, E., Belokurov, V., & Erkal, D. 2021, MNRAS, 501, 2279
Walker, M. G., Mateo, M., Olszewski, E. W., et al. 2015, ApJ, 808, 108
Wan, Z., Lewis, G. F., Li, T. S., et al. 2020, Natur, 583, 768
Wilkinson, M. I., & Evans, N. W. 1999, MNRAS, 310, 645
Yang, Y., Zhao, J.-K., Xue, X.-X., Ye, X.-H., & Zhao, G. 2022, ApJL, 935, L38
Yanny, B., Rockosi, C., Newberg, H. J., et al. 2009, AJ, 137, 4377
Yuan, Z., Chang, J., Beers, T. C., & Huang, Y. 2020, ApJL, 898, L37
Yuan, Z., Malhan, K., Sestito, F., et al. 2022a, ApJ, 930, 103
Yuan, Z., Martin, N. F., Ibata, R. A., et al. 2022b, MNRAS, 514, 1664